High Efficiency Permanent Magnet Eddy Current Couplings

Saud J Alshammari

The University Of Sheffield.

A thesis submitted for the degree of

Doctor of Philosophy

Department of Electronic and Electrical Engineering

November 2020

Abstract

Permanent magnet eddy current coupling (PMECCs) are electromagnetic devices which can transmit power from a motor to a load with no electrical or mechanical connections. Resulting in vibration isolation, low maintenance, and overload protection. However, PMECCs which have been considered exhibit relatively lower efficiencies due to their torque slip- speed characteristics. Consequently, their industrial applications as power transmission devices has been limited, and have mostly been employed in braking and damping applications. Therefore, in this thesis an investigation into the design and analysis of PMECCs for power transmission applications, where efficiency is a primary requirement, is undertaken. An example application considered in this thesis is limited-slip differentials for electric vehicles.

PMECCs topologies described in the literature have mainly employed plain copper sheets as a conducting material. Although, these were simpler and more cost effective solutions, they suffered from relatively lower efficiencies. Therefore, it is shown, that employing squirrel cage conductors embedded in softmagnetic cores, results in significant improvement in efficiency, even when less conductive materials, such as Aluminium, are employed.

3- dimensional finite element analysis is employed to design and analyse the different topologies of PMECCs, such as radial, axial single- and double sided, topologies. Furthermore, the theoretical findings are validated on a prototype, which consists of a single-sided radial field PMECC, with one rotor equipped with 14 permanent magnet poles, and the other equipped with squirrel cage conductor having 17 bars embedded in slots.

Publications

S. Alshammari and K. Atallah, “Permanent magnet eddy current couplings for power transmission”, to be submitted to IEEE Transactions on Magnetics

Acknowledgment

Before all else, I am very grateful to God for his infinite grace, mercy, and provision. I would like to convey my truthful appreciation to my supervisor Prof. Kais Atallah for his endless support and excellent supervision and guidance during my PhD studies.

I would like to thank everyone in the department of Electrical and Electronic engineering, my friends, and my colleagues of EMD group. A special thanks to the technical staff Mr. Clive Thompson and Mr. Andrew Race for their support and valuable suggestions during the manufacturing stage and laboratory tests.

I am grateful to my brothers and sisters for their constant encouragement during my PhD studies. Last but not least, everlasting gratefulness to my wife Alia Alshammari and my children Abdulaziz, Sadan and Abdullatif who made my life joyful and supported me throughout my PhD studies experience.

List of figures

List of tables

List of abbreviation

BEV	Battery electric vehicle
EV	Electrical Vehicle
EMECC	Electromagnet Eddy Current Coupling
EM	Electromagnet
NEDC	New European driving cycle
ECE- UDC	Urban driving cycle
EUDC	Extra urban driving cycle
HEV	Battery electric vehicle
ICE	Internal Combustion Engine
IM	Induction Motor
LSD	Limited-slip differential
PHEV	Plug-in hybrid electric vehicle
PM	Permanent Magnet
PMECC	Permanent magnet eddy current couplings

List of symbols

A	End ring cross section Area
DS	Double sided

e_{mr}	End ring mean radius
e_h	End ring height = slot depth
e_{th}	End ring thickness
G_f	Goodness factor
Le	End ring inductance
l	End ring length
Nr	Number of bars
Re	End ring resistance
SS	Single Sided
T	PMECCs transmitted torque
T_m	Input torque of the PMECCs
T_c	Output torque of the PMECCs
V_a	Active volume
η	PMECCs efficiency
$\Delta\Omega$	Relative speed of the PMECCs
α	Corresponding relative-speed where maximum torques occurs
ρ	Material resistivity
Ω_m	Input speed of the PMECCs
Ω_c	Out speed of the PMECCs
δ_v	Torque density

Contents

Chapter 1

Permanent Magnet Eddy Current Couplings (PMECCs)

Permanent Magnet Eddy Current Couplings (PMECCs) are electromagnetic devices which transmit torque through the interactions between permanent magnets and eddy currents induced by the difference of speed between the drive and driven rotors.[1] [2]. PMECCs are considered as an enhancement of permanent magnetic coupling, since, for synchronous permanent magnet couplings, both rotors are equipped with permanent magnets, on the other hand in PMECCs only one rotor is fitted with permanent magnets and the other is made of conductive materials [1]. Furthermore, PEMCCs exhibit a significantly gentler torque limiting action, since they don't generate the inherently large torque ripple associated with PM synchronous couplings. PMECCs have become commercially available since 1999 [3] and have been used in many industrial applications for example brake, power transmission, and damping systems [4]. The benefit of such device is to provide coupling between two rotors without any mechanical connection which leads to vibration isolation, low maintenance and overload protection [5][6]. The operation of PMECCs is straightforward, and it is based on the relative-speed (difference speed) between two rotors. When two rotors, one containing a set of permanent magnets interacts with another rotor carrying conductors, the relative motion between the two rotors induces eddy currents in the conductive material which interacts with the main field provided

by PMs in the other rotor to produce torque [7]. Furthermore, the eddy current couplings field source can be provided by an electromagnet (EM) or permanent magnets (PMs). The advantage of Electromagnet Eddy Current Coupling (EMECCs) is that the coupling can be controlled, albeit a lower magnetic flux density may be produced in the air gap, and losses occur in the excitation windings. On the other hand, the permanent magnet configuration does not allow control but provides a high air-gap magnetic field [8][9]. There are several types of structures of PMECCs, this includes, single- or double-sided permanent magnet excited radial-flux topologies, or single or double-sided permanent magnet excited axial-flux topologies. In addition, the permanent magnets can be arranged in different ways such as internal permanent magnets, surface mounted or inset permanent magnets. Table 1.1 shows some types of PM arrangements and some of their characteristics [10][11][12].

Table 1. 1 Types of PM arrangements and some of their characteristics

Surface-Mounted PM	Interior PM	Surface-Inset PM
• Little mechanical robustness • Simple, low-cost manufacturing • Ideal for low-speed application • High air gap flux density	• Mechanically robust • High cost and complex manufacturing • Ideal for high-speed application • PMs are protected inside.	• Mechanically robust • low-cost manufacturing • High air gap flux density

Over the years, several PMECCs topologies have been proposed and their performance analysed. However, a conductor sheet has almost exclusively been used for all the proposed topologies, including radial- and axial-field variants. Using a conductor sheet is certainly more practical and facilitates the manufacture of PMECC, but as will be shown in this thesis, they lead to less efficient PMECCs.

Furthermore, according to [7] the input and output torques PMECCs is equal therefore, the efficiency of PMECCs is only affected by the input speed and the relative speed, of the coupling and either the higher input speed or smaller relative speed the higher the efficiency. Moreover, even those which attempted to use a squirrel cage, seem to have been more focused on the development and validation of the modelling techniques instead of focusing on the design and optimisation of such coupling to achieve higher efficiencies.

1.1 Single sided axial -field PMECCs

The axial field PMECC arrangement shown in Figure 1.1 consists of a 6 pole-pair PM rotor, whilst the other rotor, consists of a copper disk is placed on an back-iron [13]. Figure 1.2 shows the published torque and slip-speed characteristic of the PMECCs, where it can be seen that the slip-speed corresponding to the maximum transmitted torque is around 1000rpm, making the PMECC not suitable for power transmission due to its very low efficiency.

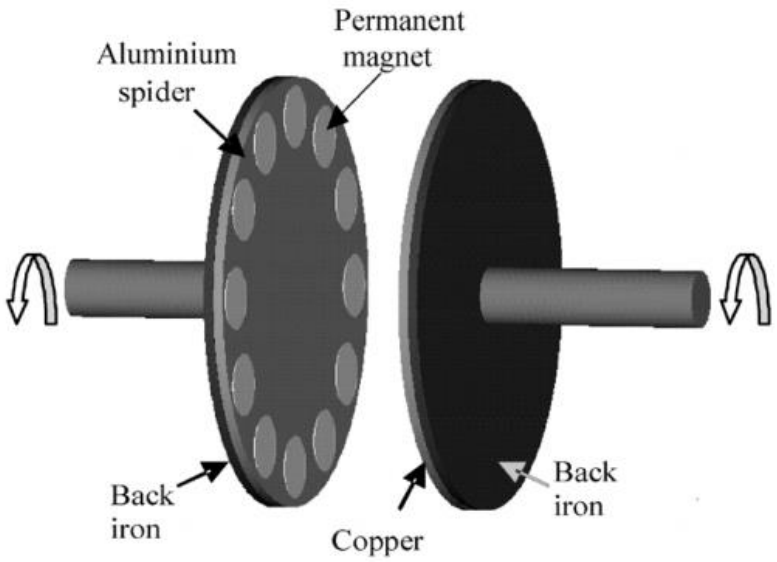

Fig 1. 1 Single sided PM axial rotating flux PMECCs [13]

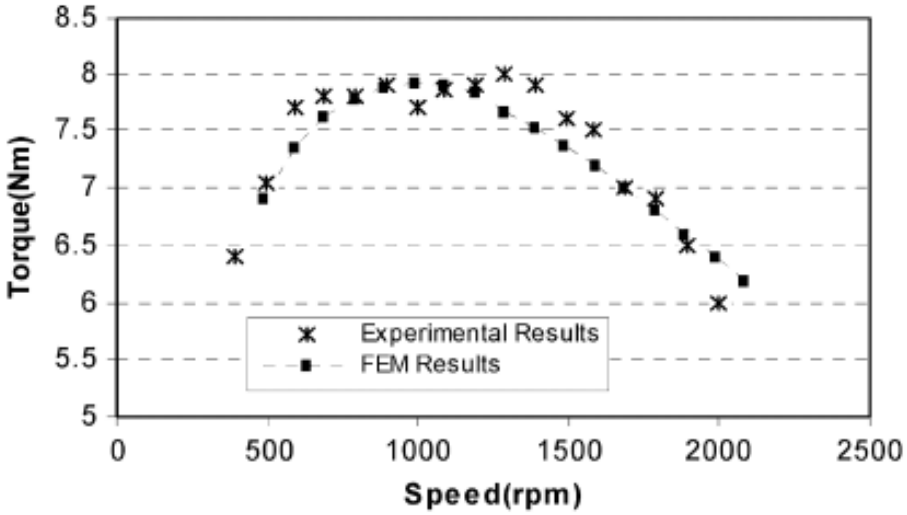

Fig 1. 2 Comparison between numerical and experimental results (2 mm air gap) [13]

Figure 1.3 illustrates an expanded view of a spoke-type PMECCs, which is equipped with copper sheet as on the one rotor [14]. For this coupling, the authors interest was only introducing a new axial PMECCs with an interior permanent magnets rather than optimizing the coupling parameters and improve efficiency. Moreover, Figure 1.4 shows the torque slip-speed characteristic, similarly to the previous PMECC, the slip-speed corresponding to the maximum transmitted torque is not yet reached at 1000rpm.

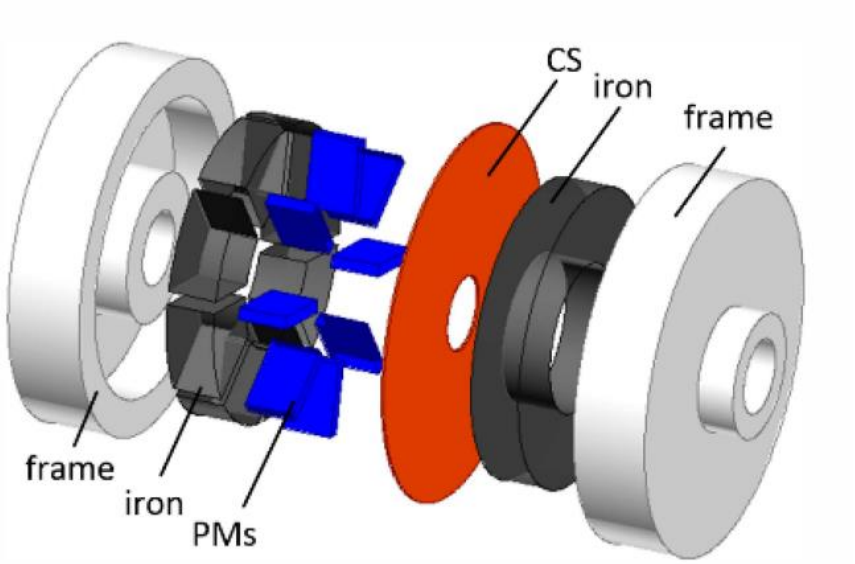

Fig 1. 3 Single Sided PM Axial Rotating Flux PMEC [14]

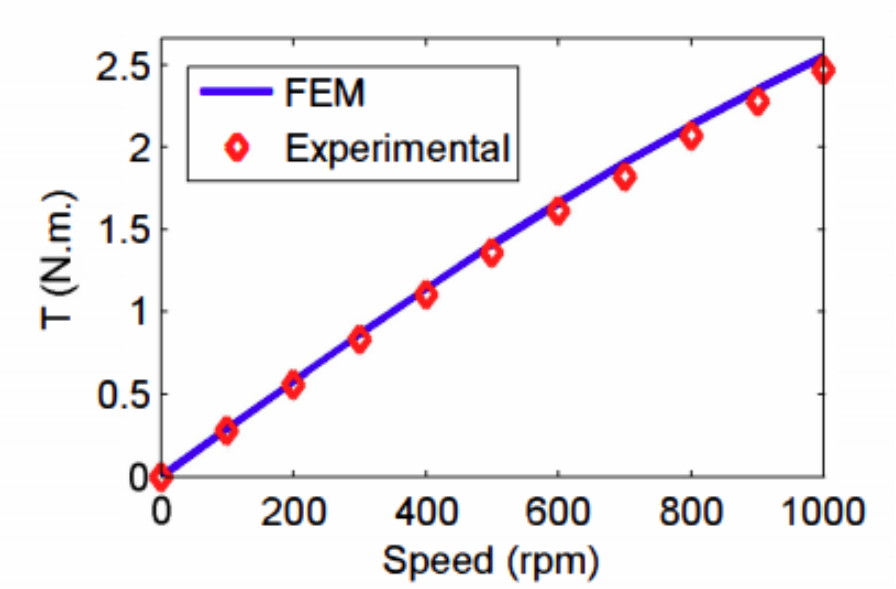

Fig 1. 4 Developed torque versus relative speed [14]

Furthermore, Figure 1.5 shows a single sided axial- flux PMECCs with slotted conductive rotor, which can be considered an axial version of a squirrel cage. In this paper the focus was proposing an analytical method for modelling the magnetic field of PMECCs rather than enhancing the coupling main factors to improve efficiency.

It consists of 6 pole pairs of permanent magnet rotor and conductive rotor with a 24 slots on the other side, and Figure 1.6 shows the torque and speed characteristic of this PMECCs [15]. Again, the slip-speed corresponding the maximum transmitted torque is still too high, ~1200rpm, to make the PMECC suitable for high efficiency power transmission.

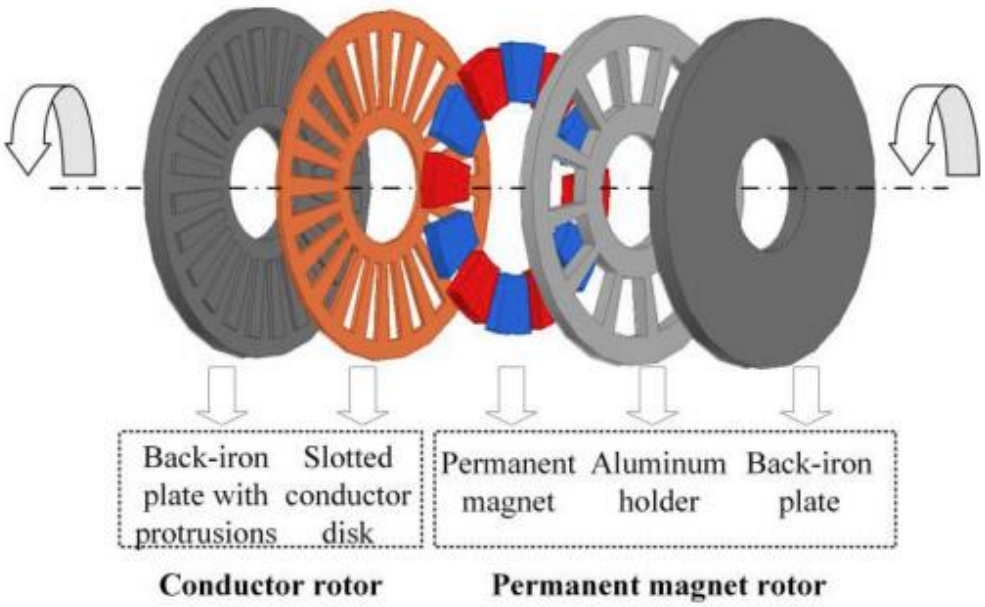

Fig 1. 5 Schematic of slotted eddy current couplings [15]

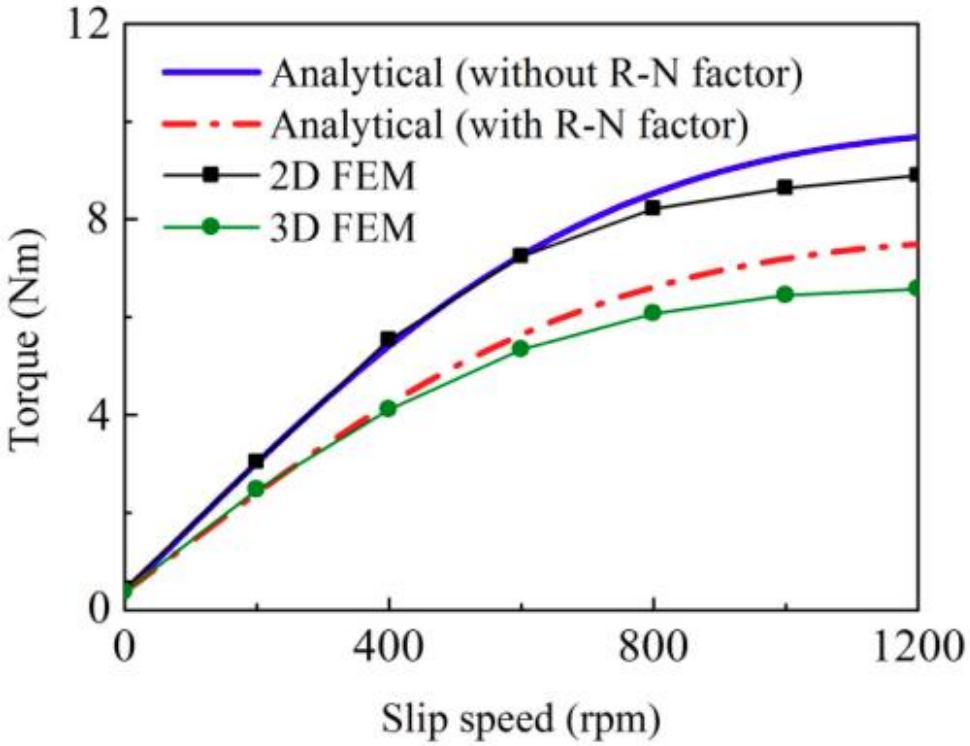

Fig 1. 6 Fig 1.7 Comparison of torque waveforms predicted analytically and by the nonlinear FEM for a slotted eddy current coupling with 24 slots and 12 poles [15]

1.2 Double-sided axial -field PMECCs

An axial double sided PMECC is shown in Figure 1.7. It consists of rotor with a solid conductor sheet, interacting with double-sided 8 pole PM rotor [9]. Furthermore, in this paper the focus was on the implementation of analytical and numerical solution and validating the results. Furthermore, a parametric analysis has been completed and each parameters was studied. However, without concentrating on PMECCs efficiency improvement. Figure 1.8 shows the torque slip-speed characteristic of the PMECC, where it can be seen that, although being better that the previously discussed PMECCs, in terms of efficiency, the slip-speed corresponding to the maximum transmitted torque is still relatively high, being around 500rpm.

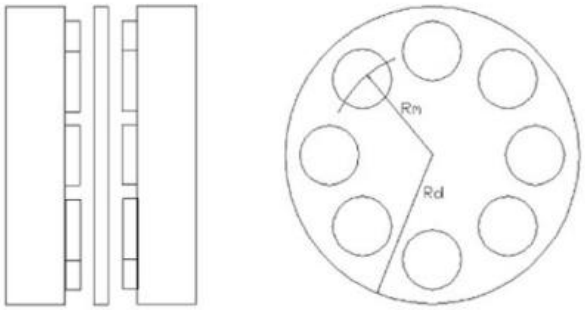

Fig 1. 7 Double sided axial-field PMECC [9]

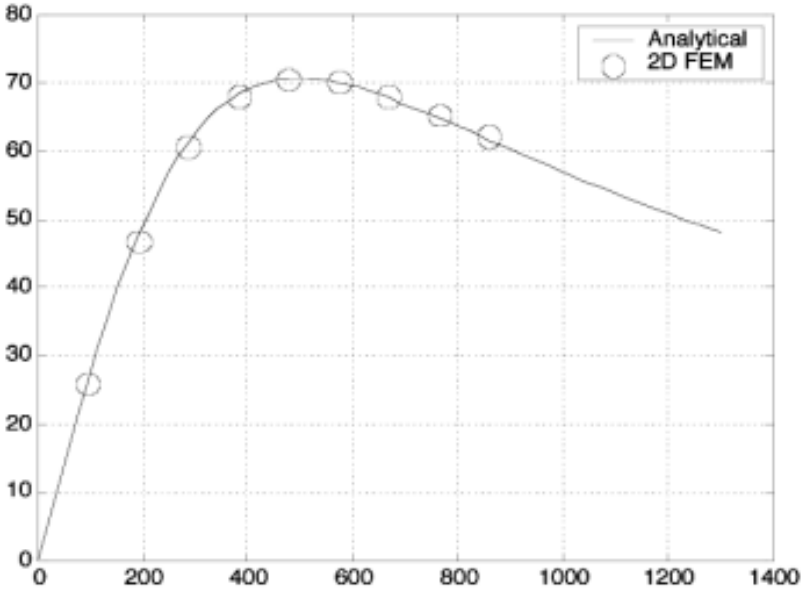

Fig 1. 8 Torque- speed characteristics [9]

1.3 Single sided radial–field PMECCs

Figure 1.9 shows a radial-field PEMCC, equipped with spoke-type PMs on one rotor, while the other rotor is equipped with a conductive sheet with a steel back-iron [11].

Figure 1.10 shows the torque slip-speed characteristic of this PMECCs. For this coupling. The authors aim was mainly to present an analysis and study on a new interior permanent-magnet radial-flux eddy. Although a sensitivity examination has been done, nevertheless, the coupling has not been optimized to improve its efficiency. Furthermore, similarly to the previous couplings, the maximum transmitted torque happens at larger slip-speed which makes it not useful for power transmission.

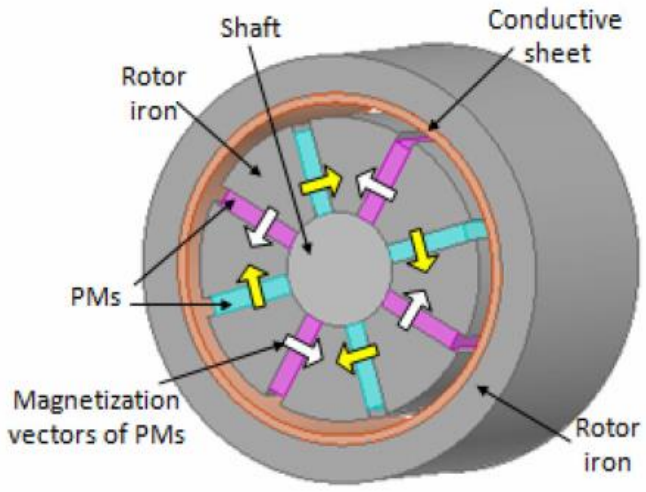

Fig 1. 9 Single sided PM radial-field PMECC with sheet conductive rotor [11]

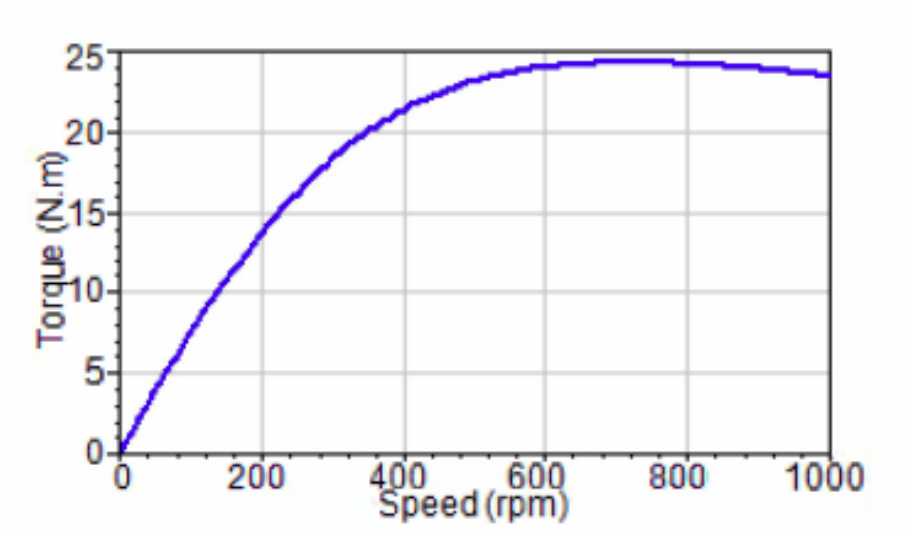

Fig 1. 10 Torque- characteristics of the case study coupler [11]

Furthermore, Figure 1.11 shows a single sided radial- flux PMECC with a squirrel cage rotor. It consists of 4 pole pairs of spoke-type PMs rotor and conductive rotor with an 18 slots squirrel cage. It can be seen that PM rotor is the inner rotor, creating significant mechanical retainment issues for high speed applications, whilst the squirrel cage is located on the outer rotor. Figure 1.12 shows the torque slip-speed characteristic of this PMECCs [16], again the slip-speed corresponding to the maximum transmitted torque is still too high for efficient power transmission.

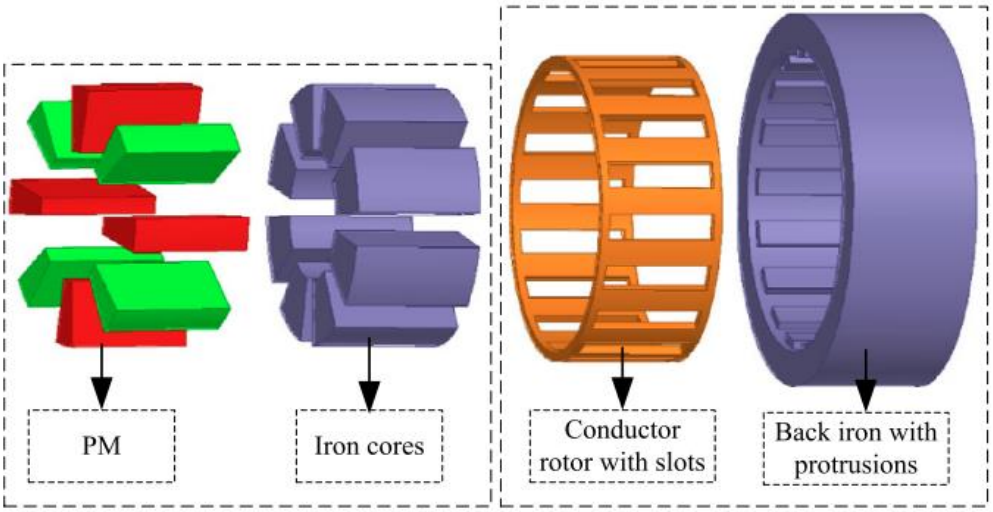

Fig 1. 11 Single sided PM radial rotating flux PMECCs with slotted conductive rotor [16]

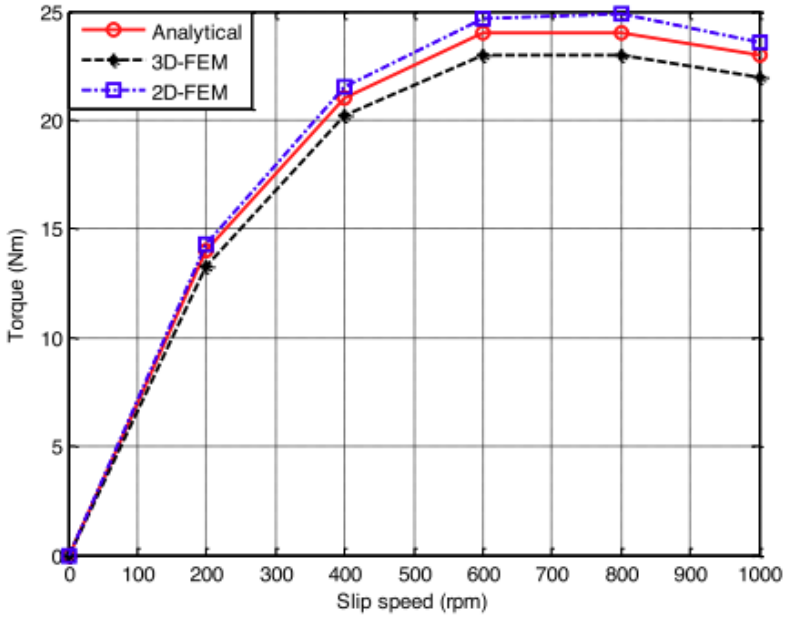

Fig 1. 12 Transmitted torque versus slip speed [16]

1.4 Double sided radial-field PMECCs

Figure 1.13 shows a double sided radial field PMECC with a sheet conductive rotor. It consists of a double sided PM rotor and a conductive sheet rotor in between to create the other side of the PMECC [17]. Similarly, Figure 1.14 shows the torque slip-speed characteristic of the PMECC, where it can be seen that the slip-speed corresponding to the maximum transmitted torque is still larger than 400rpm.

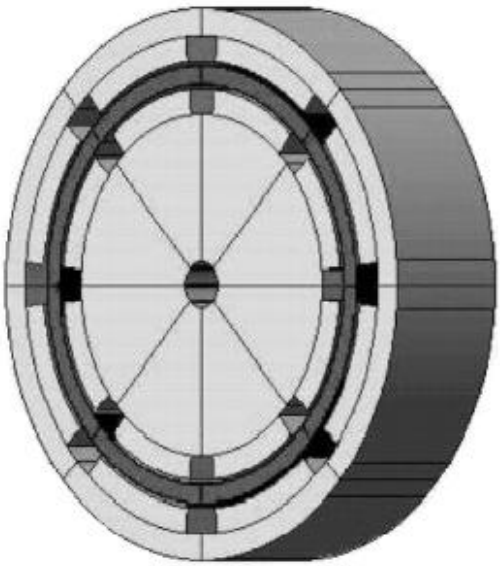

Fig 1. 13 Double- sided permanent- magnet rotational coupler [17]

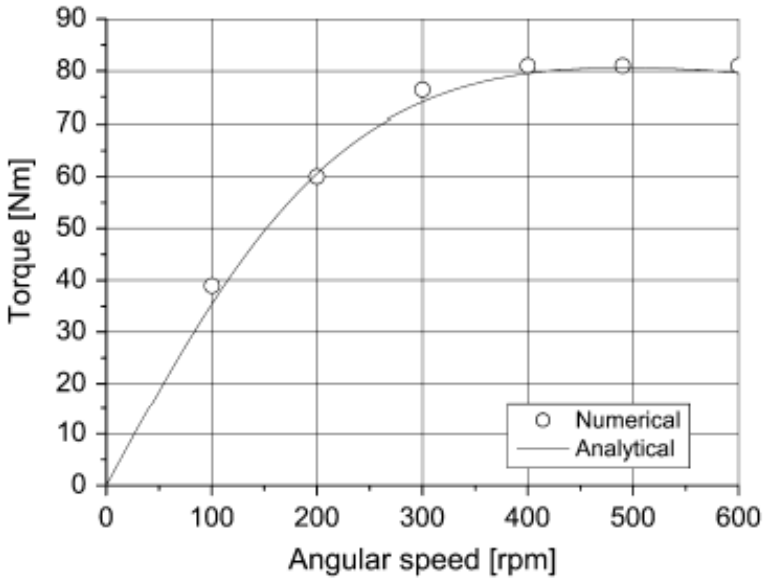

Fig 1. 14 Double sided permanent magnets torque- speed characteristics [17]

1.5 PMECCs with torque transmission characteristic

Figure 1.15 shows a radial-field PMECC with a mechanical flux adjuster (MFA). It consists of a 6 pole-pair spoke type tangentially magnetized permanent magnet rotor, and in the opposite side a copper sheet is placed on steel core to shape a conductive rotor. Furthermore, as can be seen from Figure 1.16 an outer core is mechanically axially moved to adjust the magnetic field of the PM seen by the copper sheet. Hence PM fluxes can be split to two portions, as a main flux and adjustable flux. When the core is fully engaged, this corresponds to the minimum flux seen by the copper sheet, and when is completely withdrawn, this corresponds to the maximum flux seen by the copper sheet. Although, this would work in theory, there was no discussion in the paper about the forces required to move the core in and out of engagement and over the magnetic forces it would be subjected to [18]. Finally, Figure 1.17 shows the torque slip-speed characteristic of this PMECCs with different variable distances

[18]. Again, the slip-speed corresponding to the maximum transmitted torque is still higher than 400rpm.

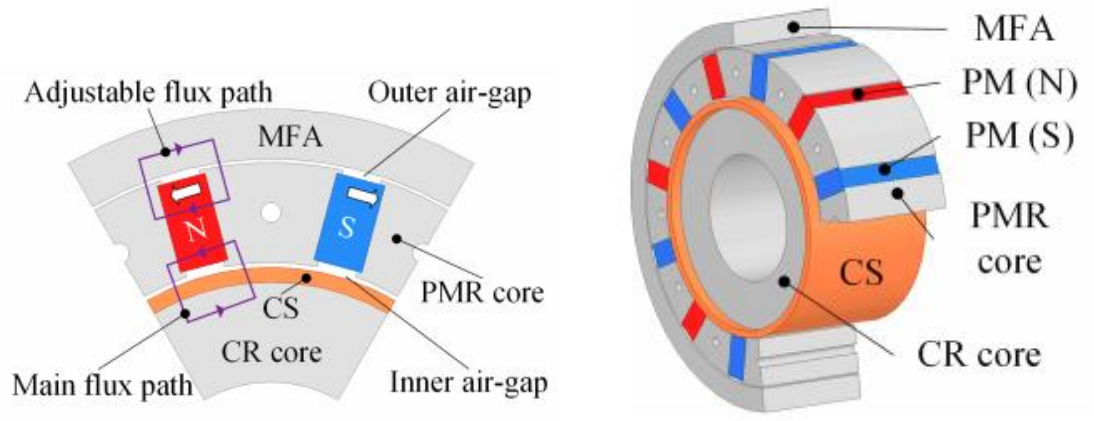

(a) Cross section (b) Part model of 3D view

Fig 1. 15 PMECC with a mechanical flux adjuster [18]

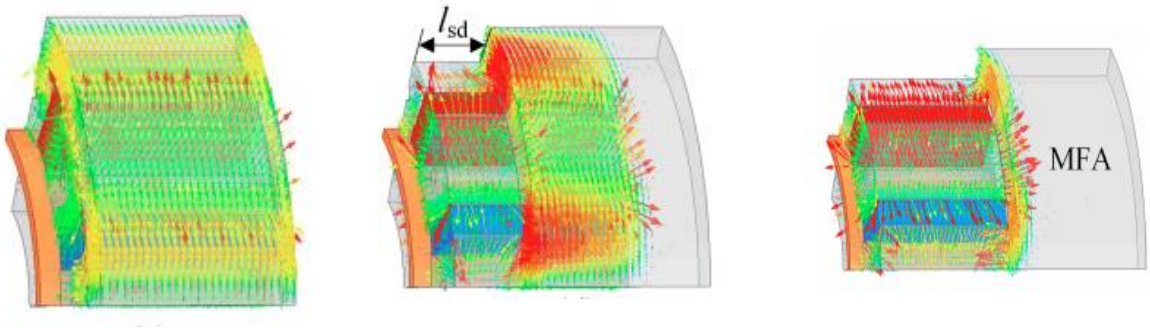

(a) l_{sd} =0 mm (b) l_{sd} = 20 mm (c) l_{sd} = 50 mm

Fig 1. 16 MFA with different moving distances [18]

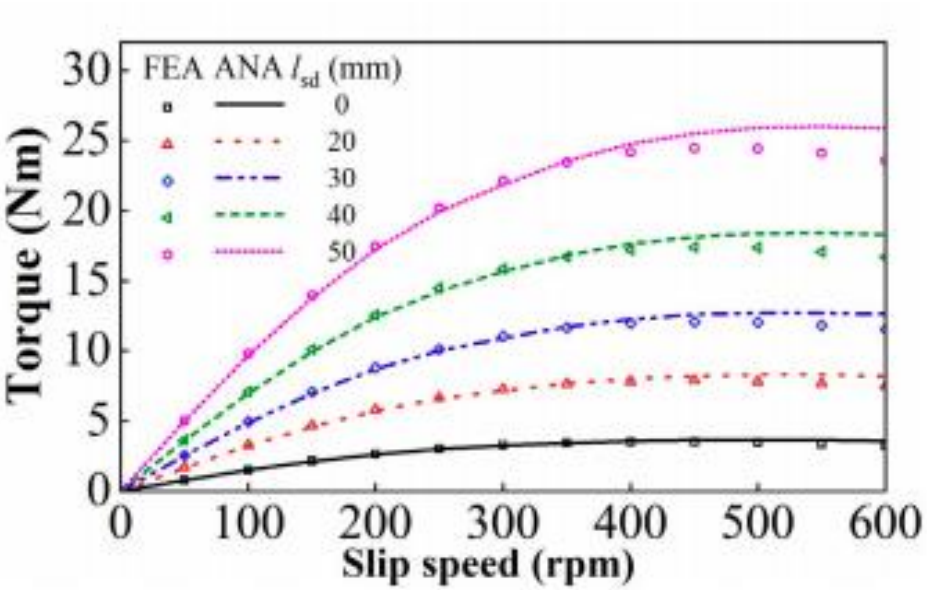

Fig 1. 17 Torque-slip speed characteristics [18]

Similarly, Figure 1.18 shows an axial PMECC with a movable stator ring (MSR), which can be moved in the axial direction. As a result, PM main flux in the PM core can be increased or reduced depending on the moving distance. Hence, the air gap magnetic field and the load speed can be controlled. Figure 1.19 explains the function of movable stator ring with different positions. Again, the ring will be subjected to significant forces, which haven't been discussed by the authors, which in turn limits the practicality of the proposed topology. Furthermore, Figure 1.20 shows the torque slip-speed characteristics of the PMECC [19], where it can be seen that similarly to the previously discussed PEMCCs, the slip-speed corresponding to the maximum transmitted torque is still high, being close to 250rpm.

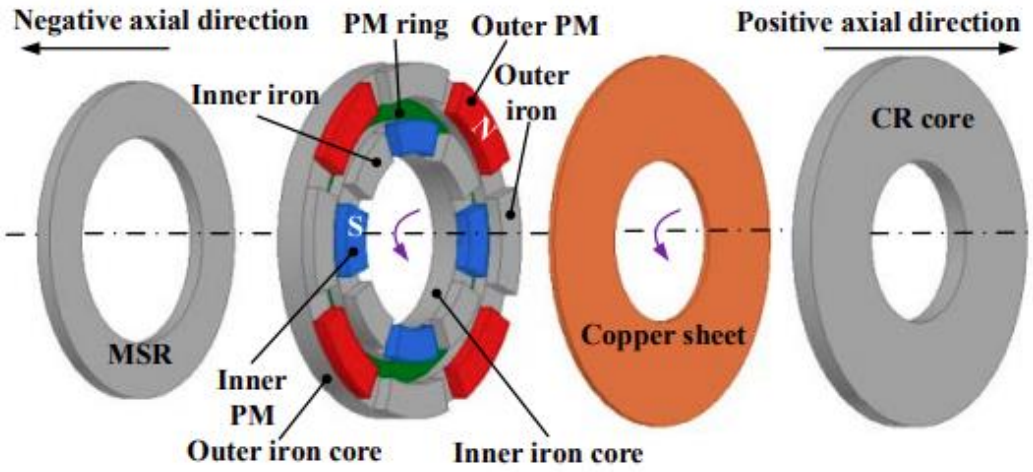

Fig 1. 18 Exploded view of PMECC with movable stator ring [19]

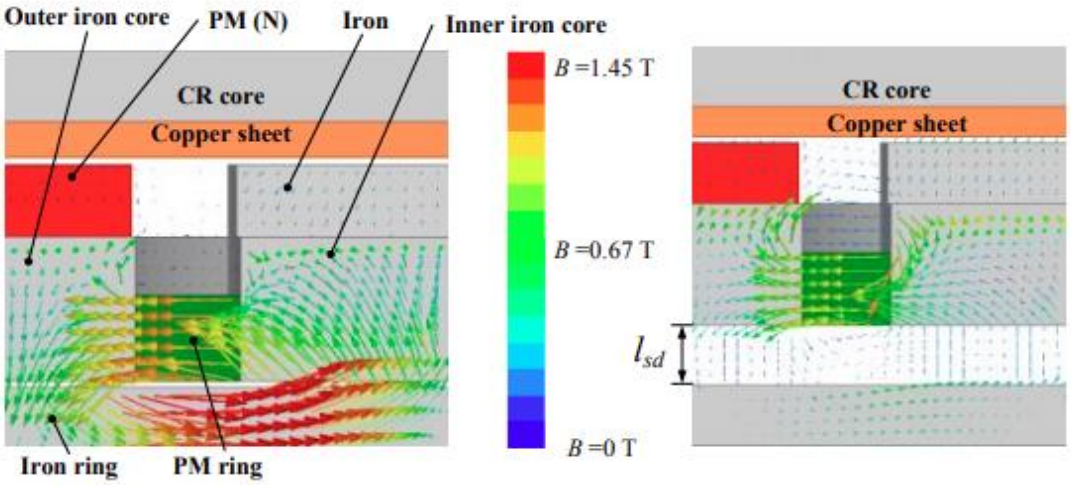

(a) (b)

Fig 1. 19 Fig 1.20 Movable stator ring (a) lsd = 1mm (b) lsd = 11mm [19]

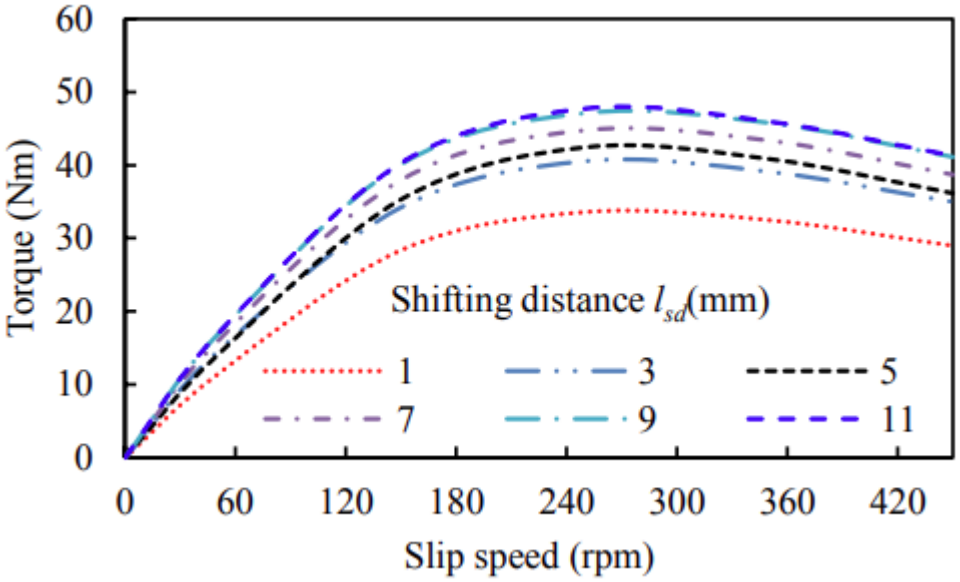

Fig 1. 20 Torque- slip speed characteristics [19]

1.6 Conclusion

In this chapter a review of the main proposed PMECC topologies and their torque slip speed characteristics is undertaken. It can be seen that research into PMECCs has been relatively limited compared to other electromagnetic devices, and there is evidence of a lack of understanding of the effects of the various parameters on the performance of PMECCs. The majority of the reported PMECCs employ conductor sheets, and none of the reported PMECCs employing squirrel cage have been experimentally demonstrated. Furthermore, a number of topologies have been proposed without adequate consideration of practical realisation. For example, for the radial-field topology employing a squirrel cage, shown in figure 1.11, the PM rotor is the inner rotor, creating significant mechanical retainment issues for high speed applications, whilst the squirrel cage is located on the outer rotor. Furthermore, for the proposed topologies with field adjustment, there has been no consideration of the actuation systems and forces required to overcome the magnetic forces.

Therefore, in this thesis an in-depth comparison of the different PMECCs topologies is undertaken, with the view of maximising efficiency and torque transmission density. Furthermore, only the topologies, which can practically be realised and exhibit good mechanical integrity during operation are considered. Consequently, a decision was made to manufacture and test a single-sided radial-field topology employing a squirrel cage rotor, and an external PM rotor is adopted. Thereby, avoiding PM retainment issues, whilst the squirrel cage parameters can easily be varied in order to maximise efficiency without affecting the volumetric torque transmission density.

Chapter 2

Electric vehicle drivetrains and permanent magnet eddy current couplings

2.1 Introduction

In this chapter, the use of PMECCs as limited-slip differentials for electric vehicles is discussed. This enables the realisation of 4-wheel drive drivetrain topologies without the need for distribution propulsion architectures, which may result in improved performance at the expense of increased cost and complexity. Therefore, the effects of PMECC torque slip-speed characteristic on the energy efficiency of the electric vehicle drivetrain are investigated.

2.2 History of Electric Vehicles

The invention and efforts of developing an electric vehicle is not quite a new story. As a matter of fact, it has an interesting long history starting back more than 100 years. Around the 1800s France and England developed first electric car, then Americans have followed and started to show interest in electric vehicles [20]. However, the introduction of the internal combustion engine, has limited the use of electric vehicle to very niche applications, such as milk floats in the UK. However, by the late 1980s/early 1990s, climate change concerns and the predicted depletion of fossil fuels, have renewed interest in electric vehicles. The first functional electric

vehicle was built during the development of electrical systems in Great Britain in the 1870s by Robert Davidson which was powered by non-rechargeable iron/zinc batteries. An advanced electric vehicle was built in 1884 by Thomas Parker which has used rechargeable batteries. Figure 2.1 shows electric vehicle built by Thomas Parker [21].

Fig 2.1 Electric vehicle by Thomas Parker 1884 [21]

In France, Gustave Trouve has built an electrical tricycle powered by a Faure's lead acid battery and Louis Antoine Krieger of Paris manufactured electrically-powered conversion units for horse-drawn carriages and first to introduce a regenerative braking system. Figure 2.2 shows a France made Krieger electric landaulet. [21]

Fig 2.2 France made Krieger electric landaulet, Washington D.C. in 1906 [21]

In the 1891 the first effective electric vehicle in the United States was built by William Morrison of Des Moines, Iowa [22]. Morrison's vehicle was equipped with a 4-horsepower motor and 24-cell battery. Figure 2.3 shows William Morrison's electric vehicle. Furthermore, early in the twentieth century Thomas Edison has developed alkaline nickel-iron battery which was better than lead acid batteries, having higher power and energy densities which improved the range of electric vehicles. Figure 2.4 shows Thomas Edison with an electric vehicle in 1913 [21].

Fig 2.3 William Morrison's electric vehicle in 1891 [22]

Fig 2.4 Thomas Edison with an electric car in 1913 [21]

From the 1960s onwards to the 21st century efforts continued to develop a viable electric vehicle for individual's transportation. In the 1990s, in the USA several manufacturers such as Chrysler, Ford, and General motors were enthusiastically involved in developing electric vehicles, when legislations and regulatory

requirements like Clean Air Act Amendment and Energy Policy were issued by the California Air resources Board to support improvements of electric vehicles and demanding the reduction in the use of internal combustion engines (ICE) [20]. Figure 2.5 shows electric pickup developed by Ford.

Fig 2.5 Ford Ranger electric pickup [20]

Additionally, with the new development of electric and hybrid vehicle technology, in 1997 Toyota reveals the Prius and followed by Honda releasing the Insight hybrid in the 1999. The electric vehicle technology continues to improve and develop and today's electric and hybrid vehicles are very advanced and with much improved range and performance.

2.3 Typical Electric and Hybrid Vehicle Drivetrains

Transportation plays a key role in keeping the world moving. Nowadays, the large proportion of vehicles around the world are still using the Internal Combustion Engine (ICE). ICE vehicles normally have longer range and easy to refuel, however, due to their high emissions, and the prediction depletion of fossil fuels, are driving

the development of alternative propulsion technologies. Resulting, in the development of electric traction systems with better efficiency and lower emissions. Electric traction can be implemented in different ways, Battery Electric Vehicle (BEV), Hybrid Electric Vehicle (HEV). Due to their noise reduction, pollution and less dependence on fossil fuels for transportation they are anticipated to substitute the Internal Combustion Engine (ICE) vehicles in the future [23][24]. Figure 2.6 shows different drivetrain configurations adopted for modern vehicles and the trend towards full electrification [25], and Table 2.1 reviews the key characteristics of EVs and HEVs [23].

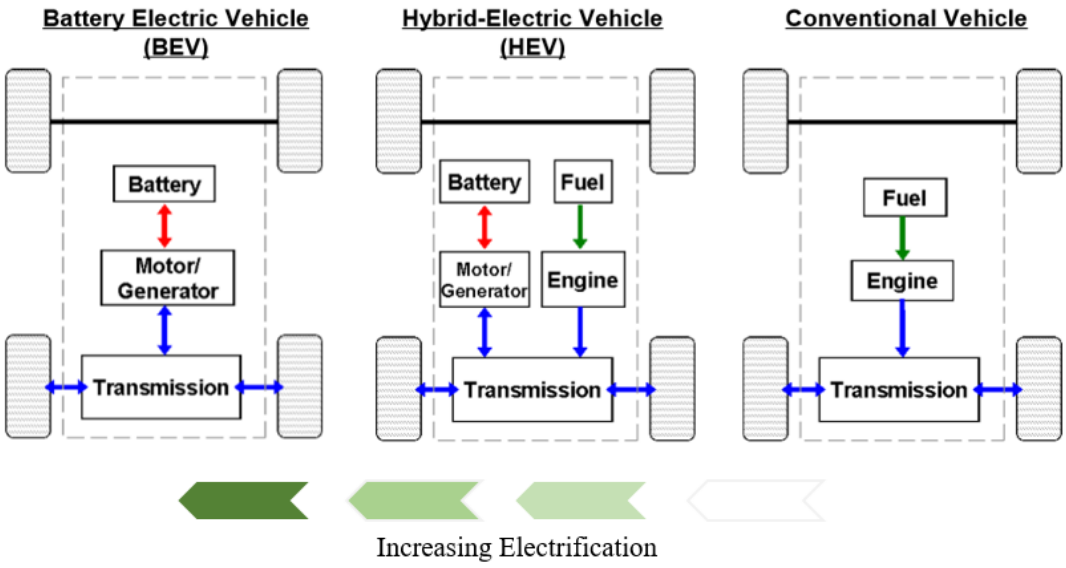

Fig 2.6 An automobile electrification level [25]

Table 2. 1 Characteristics of EVs, HEVs [23]

Vehicle type	Battery Electric Vehicle	Hybrid Electric Vehicle
Propulsion	▪ Electric motor drives	▪ Electric motor drives ▪ ICE
Energy storage subsystem	▪ Battery ▪ Supercapacitor	▪ Battery ▪ Supercapacitor ▪ Fossil or alternative fuels
Energy source infrastructure	▪ Electrical grid charging facilities	▪ Gasoline stations ▪ Electrical grid charging facilities (for PHEV)
Features	▪ Zero emissions ▪ High energy efficiency ▪ Independent of fossil fuel ▪ Relatively short range ▪ High initial cost ▪ Commercially available	▪ Low local emissions ▪ High fuel economy ▪ Long driving range ▪ Dependence on fossil fuels ▪ Higher cost than ICE vehicles ▪ Commercially available
Main issues	▪ Battery sizing and management ▪ Charging facilities ▪ Cost ▪ Battery Lifetime	▪ Battery sizing and management ▪ Control, and management of multiple energy sources

2.4 Differentials

In vehicles, and in 2-wheel drive configurations, a differential is fitted in order to enable power transmission to both wheels, while they can rotate at different speeds, when the vehicle is cornering, for example. In 4-wheel drive configurations, a differential may be added between the axles of the vehicles, again in order to enable power/torque transmission to both axles, while allowing them to rotate at different speeds [26]. In electric vehicles a differential function can be achieved electronically when the vehicle wheels are driven by separate traction machines which can be separately controlled so that the proper torque is provided to each wheel while rotating at different speeds [27][28]. Additionally, employing an induction machine

fitted with two individual squirrel cage rotors supplied from a single stator can also exhibit a differential function [29][30].

2.4.1 Mechanical Differentials

2.4.1.1 Open Differential

Open differential in Figure 2.7 is the most used differential and is found in most cars [31]. It is simple, inexpensive, and efficient. However, it has a problem when one-wheel loses traction, on a slippery surface, for example, it will absorb most of the power coming from the engine via the differential. While other wheel, which may have traction, on the opposite side of axle will remain inactive. Hence, the vehicle will not move, and as a result of this issue, a limited-slip differential (LSD) was introduced [26][7] on some high end vehicles.

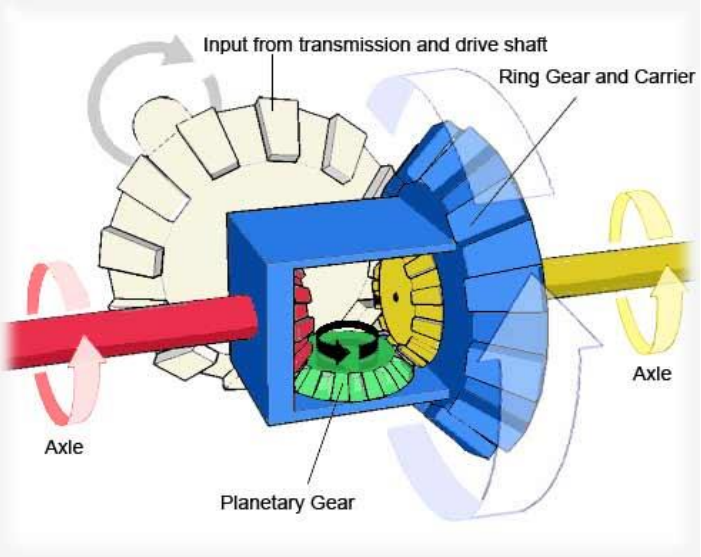

Fig 2.7 Open differential [31]

2.4.1.2 Limited Slip Differentials

Figure 2.8 shows an example of a limited-slip differential [32], which operates differently from an open differential and limits the maximum speed difference between the two wheels of the vehicle. When (LSD) senses a loss of traction on a wheel it automatically sends more power to the wheel with more grip. Nevertheless, it will not transfer all power to the wheel with good traction [26][33]. Limited slip differential is very popular in high-performance and 4-wheel drive vehicles [31].

Fig 2.8 Limited slip differential [32]

Another type of LSD has been used in 4WD vehicles is the viscous coupling, which similar to the PMECC transmits torques through slip speed between the input and output shafts. It consists of a device filled with silicone fluid, and set of plates with holes and grooves, half connected to the output shaft and the other half connected to input shaft. The shear forces applied to the silicone fluid cause by difference in speed between the drive and driven shaft, increases its viscosity and transmits torque from the drive to the driven shaft [34]. Figure 2.9 , shows viscous coupling

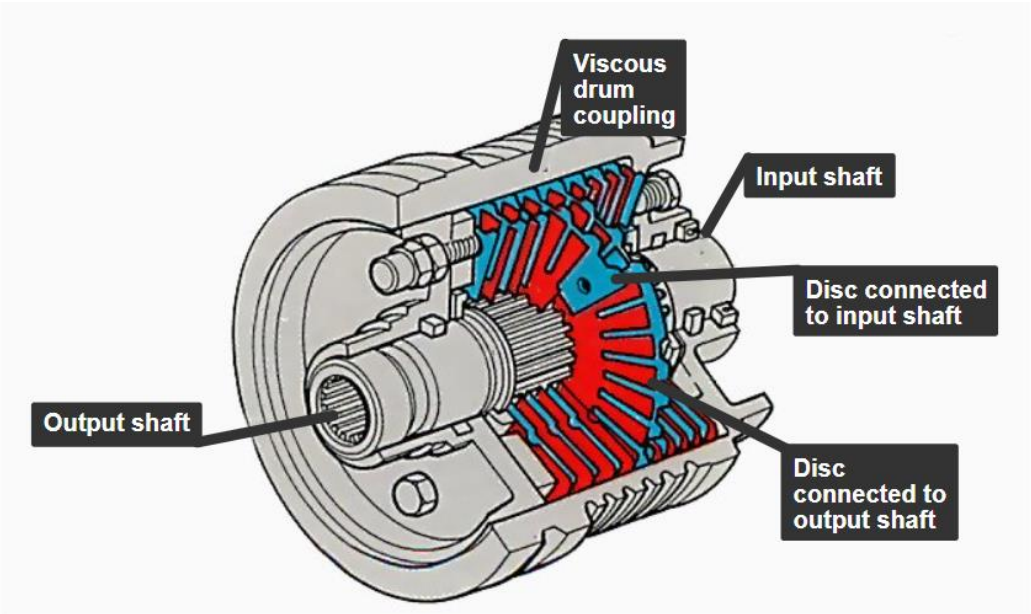

Fig 2. 9 Schematic of a viscous coupling [35].

Many vehicle manufacturers have used the viscous couplings as centre differentials to achieve 4WD capability. However, this is not permanent since in normal driving conditions, the vehicle is essentially a 2WD, and torque is transferred to the other axle when the main axle loses traction for any reason. Especially under aggressive driving, the life of the viscous coupling can be limited due the deterioration of the properties of the silicon fluid.

2.4.2 Electrical Differential

2.4.2.1 Electronic Differential

Electronic differential was introduced in [27], where electric vehicle can be driven by separate electrical machines. Electrical machines can be controlled, so each wheel receives the required speed/ torque hence, achieving the operation of mechanical differential electronically [27][28]. Figure 2.10 shows electric vehicle with

separately controlled motor for each wheel [36]. However, due to costs of the components and the reduced reliability related to multi-drive structures an induction traction machines equipped with two independent squirrel cage rotors supplied from a single stator was proposed [7]. However, the uncertainty of unbalanced transient torques which can be caused by the machine or power electronics faults remains a major disadvantage of multi-drive configurations [7].

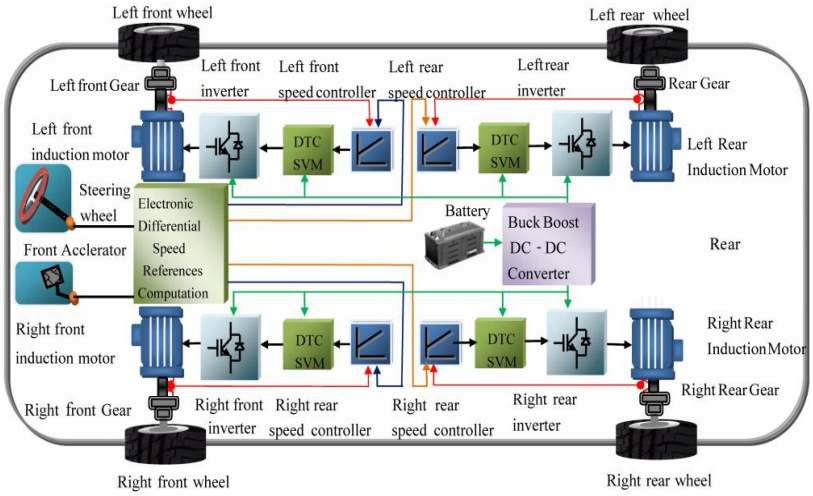

Fig 2.10 Electric vehicle with separately controlled motor for each wheel [36]

2.4.2.2 The Differential Induction Machine

The proposal of induction machine having two separate cage rotors which can be directly connected to the opposite wheels of the vehicle and supplied from a single stator was introduced in [30]. Figure 2.11 shows a differential induction machine, where a difference of speed between the wheels can be tolerated, which can meet electric/ hybrid vehicle differential requirements [29][30]. Furthermore, in [7] the authors have proposed a brushless permanent magnet machine with integrated differential, where the torque is transmitted to the wheels/axles through two

permanent magnet eddy current couplings which exhibit the characteristic of limited slip mechanical differential. This will be discussed in detail in the next sections.

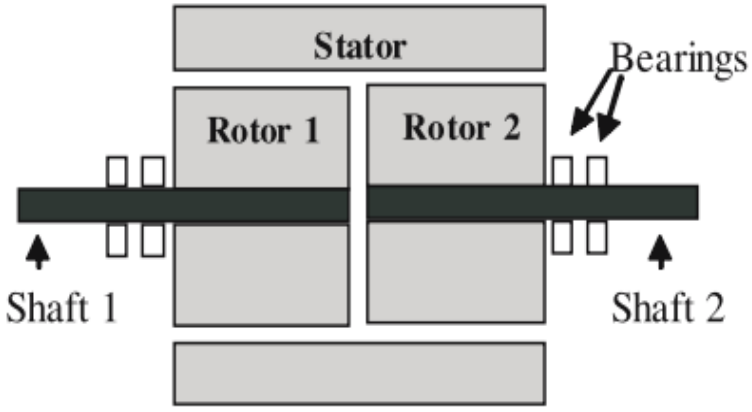

Fig 2. 11 The differential induction machines [30]

2.5 Driving Cycle and PMECCs Efficiency

2.5.1 PMECCs Efficiency

According to [7] integrating an PMECCs with an electrical machine in EV drivetrains will function as a limited slip differentials and can convey the traction machine's torque with efficiencies more than 98%, over a driving cycle. The PMECC efficiency is given by:

$$\eta = \frac{T_c \ \Omega_c}{T_{\mathrm{m}} \ \Omega_{\mathrm{m}}} \tag{2.1}$$

Where T_{m} and T_c are the input and output torques and Ω_{m} and Ω_c are the input and output speeds of the PMECC, respectively. As for an eddy current coupling the input and output torques are identical, therefore, $T_m = T_{\mathrm{c}}$ and $\Omega_c = \Omega_{\mathrm{m}} - \Delta\Omega$ where $\Delta\Omega$ is the relative speed and equation (1) could be written as [7]:

$$\eta = \frac{T_c}{T_m} \frac{\Omega_m - \Delta\Omega}{\Omega_m} \tag{2.2}$$

$$\eta = 1 - \frac{\Delta\Omega}{\Omega_m} \tag{2.3}$$

Which confirms that the efficiency of eddy current coupling is only influenced by the input speed Ω_m and the relative speed, $\Delta\Omega$, and the higher Ω_m and smaller $\Delta\Omega$, the higher the efficiency. Furthermore, the transmitted torque is only a function of relative-speed and could be, by analogy torque-slip equation of 3 phase of induction machine, approximated by [7]:

$$T = 2\, T_m \frac{\Delta\Omega\, \alpha}{(\Delta\Omega^2 + \alpha^2)} \tag{2.4}$$

T_m is the maximum torque which can be transmitted, and α is the corresponding relative-speed. Moreover, to evaluate the torque transmission functionality and efficiency, a simulation study of radial field PMECCs, and used as LSDs is undertaken.

2.5.2 Drivetrain configurations employing PMECC

Figure 2.13 shows examples of the considered drive train configuration employing an electrical machine and PMECCs [7]. In Figure 2.13 (a) in this 4- wheel drive configuration it can be seen that the electric drive is placed in the middle of the transmission system and connect the front and rear axles via PMECCs, and acts as a permanent 4WD drivetrain. During normal driving conditions relative speed between PM rotor and conductive rotor is very small and optimum torque is transmitted to both axles. However, when either axle loses traction which will experience less

resistance the relative speed between the rotors will increase hence, torque will be transmitted to the other axle by the opposite coupling. Figure 2.13 (b) shows a part time 4WD system, similar to those employing the viscous coupling in conventional vehicles. In this case, under normal conditions, the vehicle essentially operates in 2WD mode, through the main axle connected to the traction machine, and torque is transferred to the other axle, only when traction in the main axle is reduced.

To evaluate the efficiency of the eddy current coupling on electric vehicles application, a driving cycle is considered. A driving cycle is a speed-time profile meant to represent a real-world driving pattern to evaluate and compare vehicle efficiency and emissions. There are numerous types of driving cycles [37][38], and examples are 1) EU driving cycle 2) The US driving cycle 3) Japanese driving cycle. The new European driving cycle NEDC is considered and employed. The NEDC consists of two cycles including, ECE which is an urban driving cycle also known as UDC (Urban Driving Cycle) and EUDC extra urban driving cycle. The NEDC comprises of four repeated ECE cycles without disruption and followed by one EUDC. The ECE cycle is created to represent a city driving conditions with maximum speed of 50 km/h. The EUDC cycle is to be implemented right after the fourth ECE cycle to represent more aggressive driving styles like on highways with maximum speed of 120 km/h [39]. Figure 2.12 shows the New European driving cycle and its characteristics are [37]:

Distance travelled: 11017 m

Duration: 1180 s

Average speed: 33.6 km/h

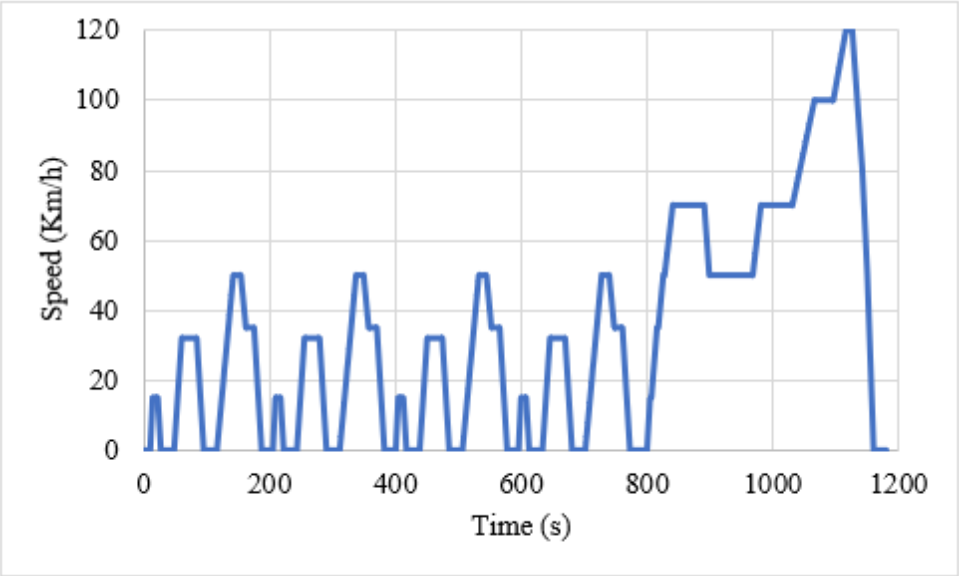

Fig 2.12 New European Driving Cycle

A vehicle model example including axle and tyres, provided by MathWorks [40] is equipped with the drivetrains shown in Fig. 2.13. The vehicle parameters are summarised in Table 2.2. When operating using the drivetrain shown in Figure 2.13 (a), with each PMECC selected with a maximum transmitted torque half of the peak of the traction machines, the energy lost in the PMECCs due to the slip speed, is 2% of the total energy transferred through the drivetrain, when the slip speed of the PMECCs corresponding to the maximum transmitted torque is 100rpm, however, the energy lost drops to 1% when this is reduced to 50 rpm. On the other hand, when employing the drivetrain in Figure 2.13 (b), loss of energy on the PMECC becomes negligible when following the NEDC driving cycle, since under such moderate driving conditions, torque/power are mainly transmitted to the main axle, directly connected to the traction machine.

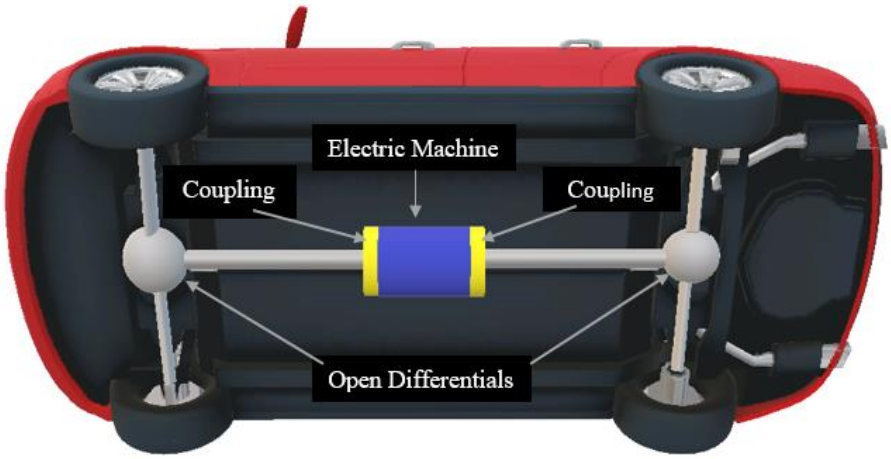

(a) Permanent 4WD configuration

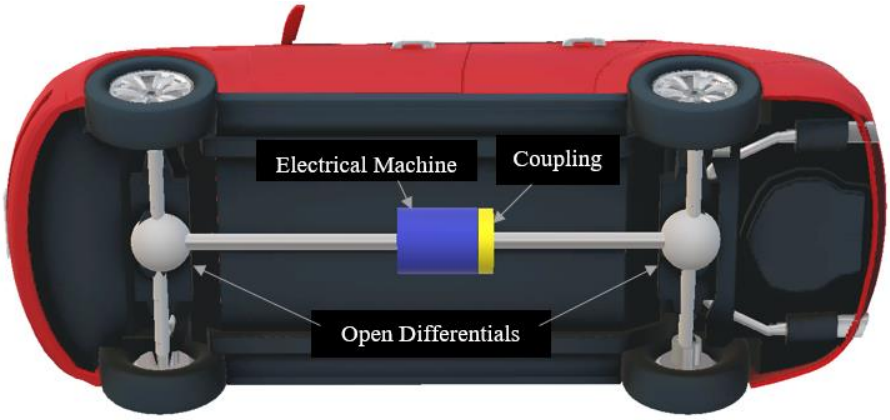

(b) Part-time 4WD configuration

Fig 2.13 Electrical machine with integrated differential. (4 -wheel drive)

An existing Matlab/Simulink model of a full vehicle, including tyre models has been modified by adding an electric drivetrain, using PMECCs as differentials to achieve permanent and part-time 4WD operations. The model has been developed in order to assess the performance of the drivetrain, in terms of efficiency of the PMECCs and the driving capability under dynamic wheel slip conditions.

Permanent 4WD

Figure 2.14 shows the variation of the vehicle speed from 0 to 60 MPH, during normal driving conditions and when the axle loses traction during initial acceleration. It can be seen that the loss of traction and the slip of the front axle didn't have a significant effect on the performance of the vehicle. Figure 2.15, shows the torques on the front and rear axles, it can be seen that with the exception of the early acceleration phase between 0 to 2s, when the front axle loses traction, and the more torque is diverted to the rear axle, under normal conditions the torque split between the axles is essentially the same.

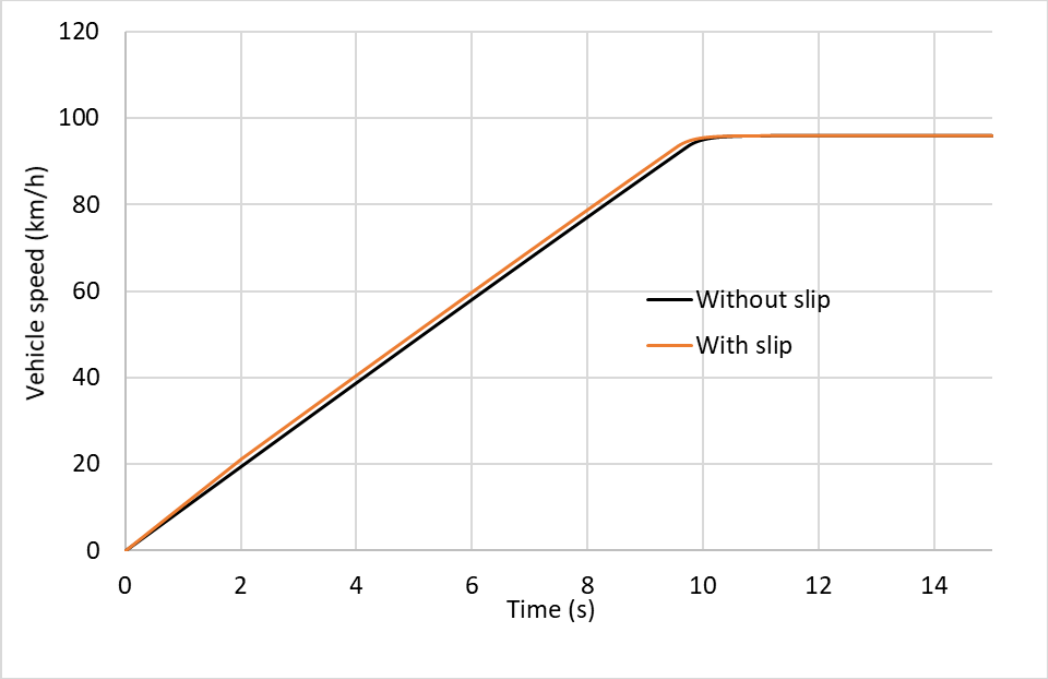

Fig 2. 14 Variation of vehicles speed with time

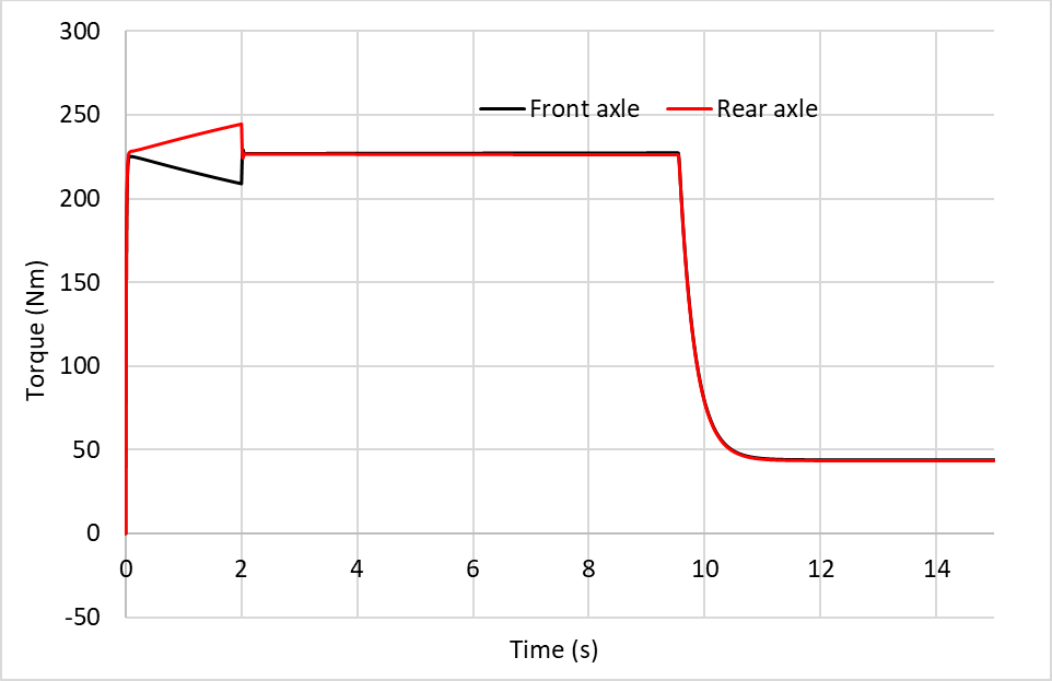

Fig 2. 15 Variation of axle torque with time

Part time 4WD

Similarly, Figure 2.16 shows the variation of the vehicle speed from 0 to 60 MPH, during normal driving conditions and when the axle loses traction during initial acceleration, when equipped with a part time 4WD drivetrain. It can be seen that similarly to the full-time 4WD, the loss of traction and the slip of the front axle didn't have a significant effect on the performance of the vehicle. Figure 2.17, shows the torques on the front and rear axles, it can be seen that with the exception of the early acceleration phase between 0 to 2s, when the front axle loses traction, the rear axle contributes more to the propulsion of the vehicle, when traction of the main front axle is reduced.

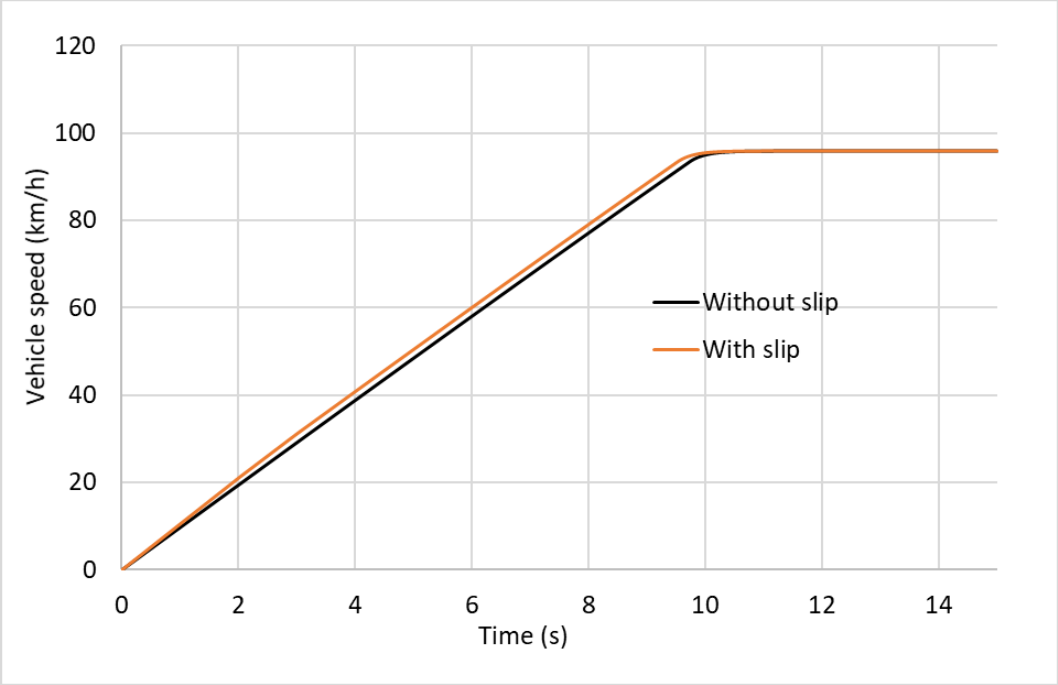

Fig 2. 16 Variation of vehicles speed with time

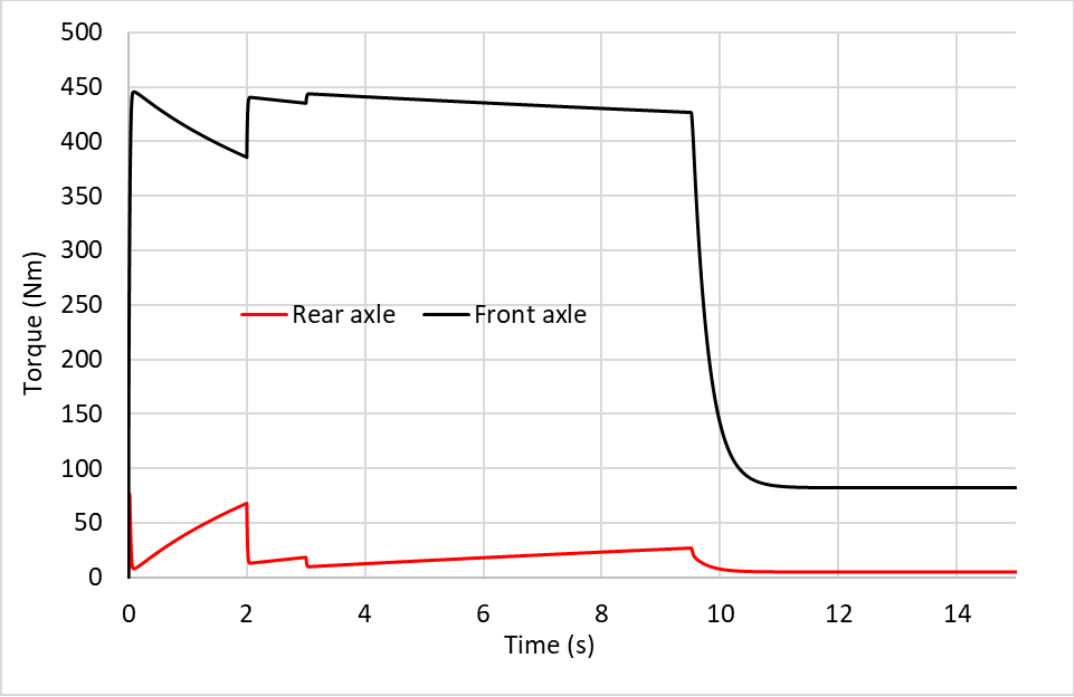

Fig 2. 17 Variation of axle torque with time

Table 2. 2 Parameters of the considered vehicle

Parameter / unit	**Symbol**	**Value**
Radius of wheels / m	r_w	0.4062
Vehicle mass / (kg)	m	1200
Gravitational acceleration (m/s^2)	g	9.807
Rolling resistance coefficient	k_r	0.015
Product of drag coefficient and front area (m^2)	$c_d \cdot A$	1.2
Air density (kg/m^3)	ρ	1.250
Efficiency of differential	η_{dif}	0.980
Differential Gear Ratio	G_r	4:1

2.5.3 Alternative Drive-train Configurations

There are a number of possible drivetrain configurations for Electric vehicle where PMECCs can be employed as limited slip-differential. Figure 2.18 shows two-wheel drive configuration and electrical machine and PMECCs installed on axle and it can be front or rear wheel drive. Furthermore, Figure 2.19 shows a part-time 4WD configuration, however the eddy current coupling main field source is provided by electromagnet rather than permanent magnets.

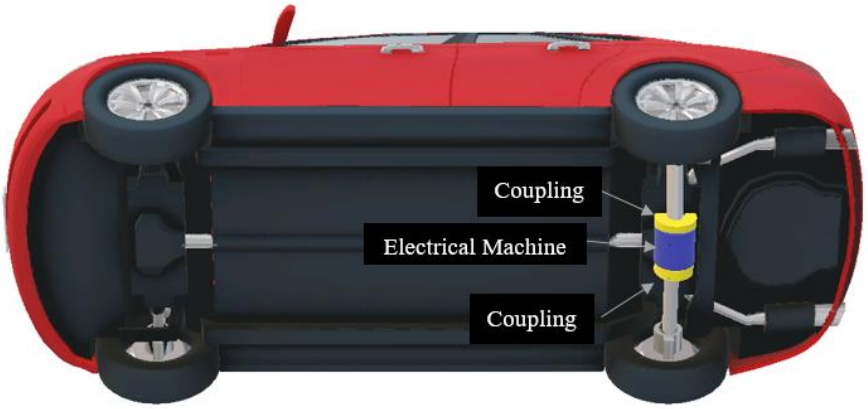

Fig 2. 18 Two-wheel drive integrated electrical machine and limited-slip differential mounted on an axle.

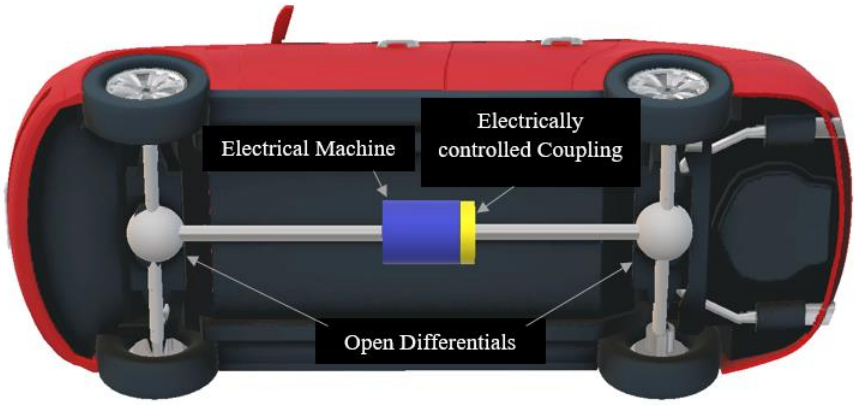

Fig 2.19 Part-time 4WD configuration, with electrically controlled EMECC

2.6 Motivation and research objective

This chapter explored the possibility of using PMECC as LSDs in electric vehicle drivetrains. For the particular vehicle, employed in the example, it was shown that energy efficiencies in excess of 99% can be achieved as long as the slip speed corresponding to the maximum PMECC transmitted torque is kept below 100rpm. LSDs on electric vehicles is only an example application of these high efficiency PMECCs, however, their applications can be extended to typical power transmission applications, especially those characterised by high speed. Indeed, the PMECC efficiency is very high for high speed applications, as it can be seen in Figure 2.20 when the input speed of the coupling is high and the slip speed is low a high efficiency is maintained. For instance, at the input speed of 10 krpm when the slip speed is 180 rpm the efficiency is 98.2%, however, when the slip speed is reduced to 20 rpm the efficiency increases to 99.8% which explains that the permanent magnet eddy current couplings efficiency is affected only by the input speed or the slip speed between the rotors and either the higher input speed or smaller slip speed the higher the efficiency. Furthermore, unlike their synchronous couplings counterparts, torque limiting from PMECCs is significantly gentler, since it doesn't result in the torque ripple associated with slipping synchronous couplings. In addition, the latters are essentially a compliant transmission, which can introduce mechanical resonances which needs to be considered, while the PMECCs would act as dampers. Moreover, in this thesis an investigation into the design and analysis of PMECCs for power transmission applications, where high efficiency is necessary, is undertaken. Different PMECCs topologies will be developed and various parameters will be studied and analysed to examine their effect on the efficiency and performance of the PMECCs.

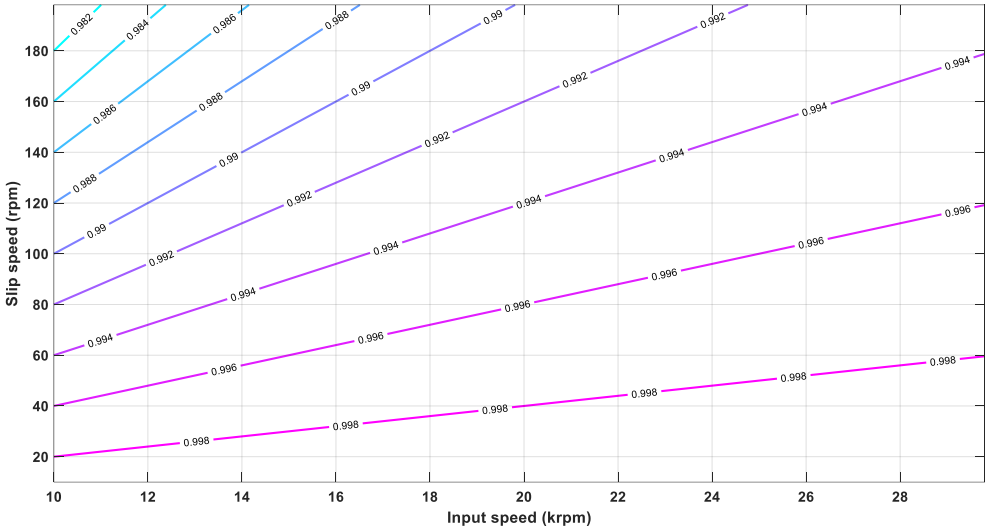

Fig 2. 20 PMECC efficiency map with high speeds

Chapter 3

An Investigation and design of different structures of radial fields permanent magnet eddy current couplings

3.1 Introduction

In this chapter, different sections are introduced to investigate multiple designs of radial permanent magnet eddy current couplings (PMECCs). PMECCs consist of two rotors, single-sided (SS) and double-sided (DS), topologies equipped with surface permanent magnets (SPM) forming a permanent magnet rotor and two different types of conductive rotors, are considered. The first rotor structure has conductors

embedded in slots creating a squirrel cage rotor, and the second rotor structure is simply a conductive sheet rotor. Three-dimensional finite elements software (Maxwell) is used and a transient solution is adopted to simulate, analyse, and compare the results of different pole/slot combinations, slot depth of the squirrel cage rotor, and conductive sheet thickness. Table 3.1 shows the different examined design of PMECCs where the pole/slot combinations has been selected to achieve the lowest cogging torque. Furthermore, a goodness factor G_f to assess and compare the performance of PMECCs for power transmission applications is introduced. The factor is essentially the volumetric damping factor density, which is derived from the approximate equation (2.4) for the torque slip-speed characteristic. Therefore:

$$G_f(\Delta\Omega) = \frac{\frac{dT_t}{d(\Delta\Omega)}}{V_a} \tag{3.1}$$

Where,

$$T_t = 2\,T_m\,\frac{\alpha\,\Delta\Omega}{(\Delta\Omega^2+\alpha^2)} \tag{3.2}$$

Therefore,

$$G_f(\Delta\Omega) = \frac{2\,T_m\,\alpha}{(\Delta\Omega^2+\alpha^2)}\,\frac{\left(1-\frac{2\,\Delta\Omega}{(\Delta\Omega^2+\alpha^2)}\right)}{V_a} \tag{3.3}$$

Which at $\Delta\Omega = 0$, becomes:

$$G_f(\Delta\Omega = 0) = \frac{2\,\delta_v}{\alpha} \tag{3.4}$$

Table 3. 1 Examined designs of PMECCs.

Topology type	3D-Single-sided				3D-Double-sided			
Conductive rotor structure	Squirrel cage		sheet		Squirrel cage		sheet	
Conductive rotor material	Cu	Alu	Cu	Alu	Cu	Alu	Cu	Alu
Pole and Pole/Slot Combination	14/17 - 22/23		14		14/17 - 22/23		14	
Conductive sheet Thickness (mm)			2-12				4-8	

3.2 Single sided permanent magnet eddy current couplings

3.2.1 PMECCs with Squirrel cage rotor type

This section investigates the performance of single-sided PMECCs with a squirrel cage rotor. Fig 3.1 shows a general cross-section of permanent magnet eddy current couplings equipped with a squirrel cage rotor. Fig 3.2 and Table 3.2 show the geometry and the parameters of PMECCs, respectively.

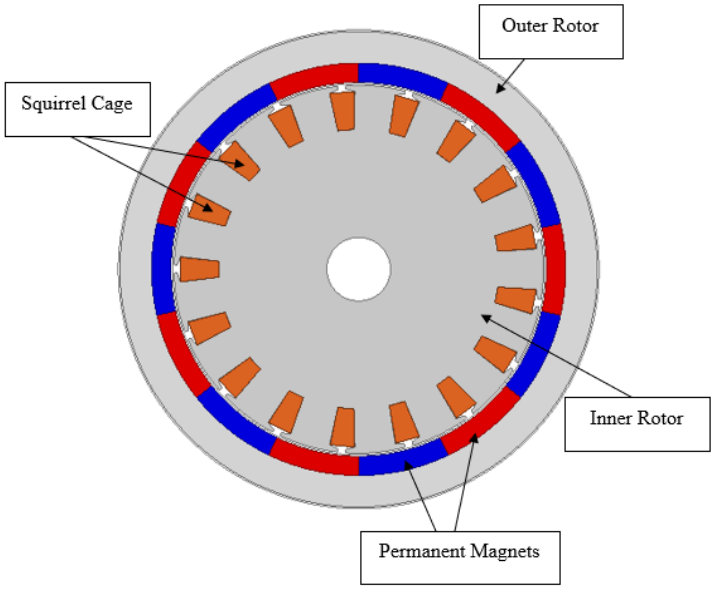

Fig 3. 1 Cross section of permanent magnet eddy current couplings

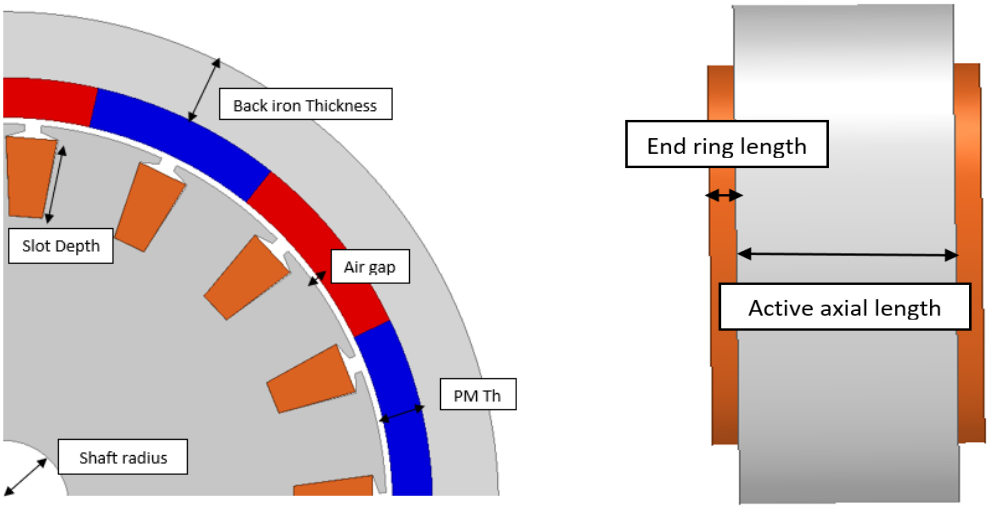

Fig 3. 2 Geometric parameters of the PMECCs

Table 3. 2 Parameters of squirrel cage permanent magnet eddy current couplings

Parameter name	Value/ type
Active diameter	150 mm
Air gap length	1mm
Number of poles	14 / 22
Number of slots	17 / 23
Permanent magnets	NdFeB 30
Squirrel cage material	Copper / Aluminium
Axial Length	50mm

3.2.1.1 Squirrel cage PMECCs with 14/17 pole/slots

This section focuses on squirrel cage PMECCs with 14/17 pole/slot combination. A 3D finite element analysis is completed to study the influence of permanent magnet thickness on the transmitted torque and the impact of slot depth and end ring length on relative speed where the maximum transmitted torque occurs, and finally the material type of the conductive rotor. Fig 3.3 shows a PMECCs with pole/slot combination of 14/17.

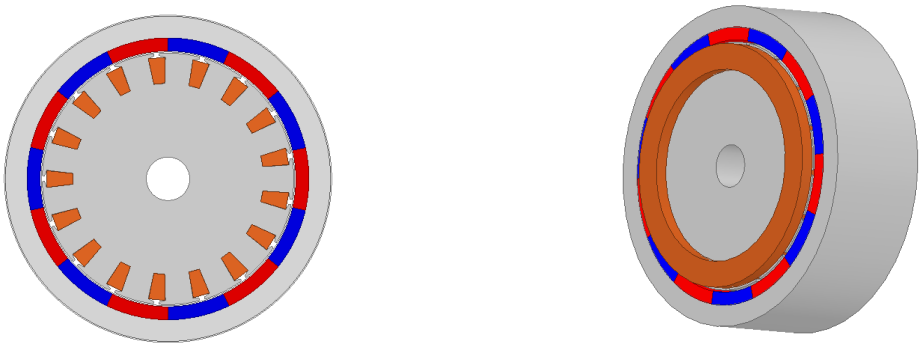

(i) Cross-sectional view (ii) 3D view

Fig 3. 3 PMECCs with 14/ 17 pole / slot combination

3.2.1.1.1 Copper squirrel cage

Fig 3.4 illustrates the effect of increasing the thickness of permanent magnets on the transmitted torque. Clearly, it can be seen that the transmitted torque is improved by increasing the permanent magnet thickness due to increase in magnetomotive force

However, beyond 6 mm of magnet thickness the improvement torque transmission is small and may not justify the increase cost of the magnet.

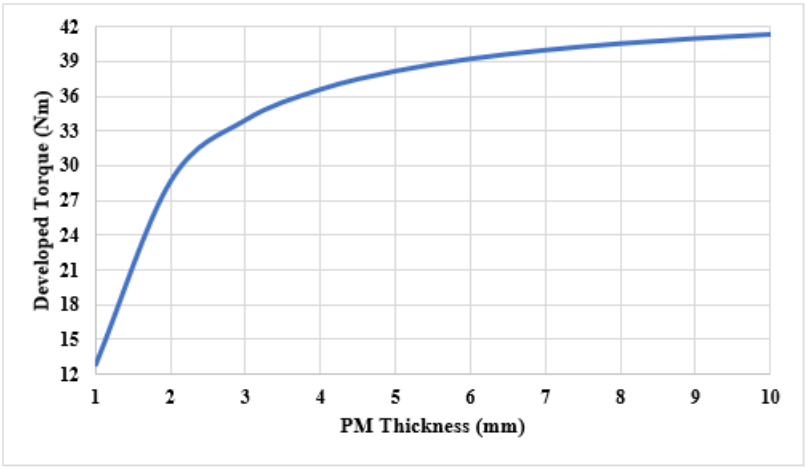

Fig 3. 4 Variation of maximum transmitted torque with thickness of PM. (14/ 17 pole/slot combination)

Furthermore, with a selected permanent magnet thickness of 6 mm and an end ring length of 5 mm, Fig 3.5 shows the variation of the transmitted torque with a relative speed for 11 mm slot depth. It can be seen that for this coupling, the maximum transmitted torque occurs at the relative speed $\alpha \approx 136.4$ rpm. Moreover, Fig 3.6 shows the variation of the transmitted torque with a relative speed of the same PMECCs when the slot depth is increased to 15 mm. The result indicates that, by increasing the amount of copper material, the relative speed α, at which the maximum torque occurs, is reduced to $\alpha \approx 88.5$ rpm.

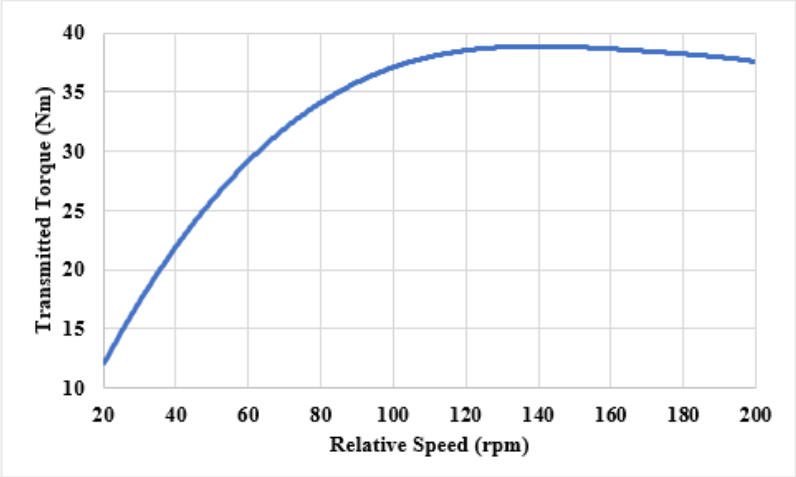

Fig 3. 5 Variation of transmitted torque with relative speed. (11mm slot depth; $G_f = 680\ (\frac{\text{Nm}}{\text{rpm}})/\text{m}^3$) ($\eta$ ~ 98.7% over an NEDC)

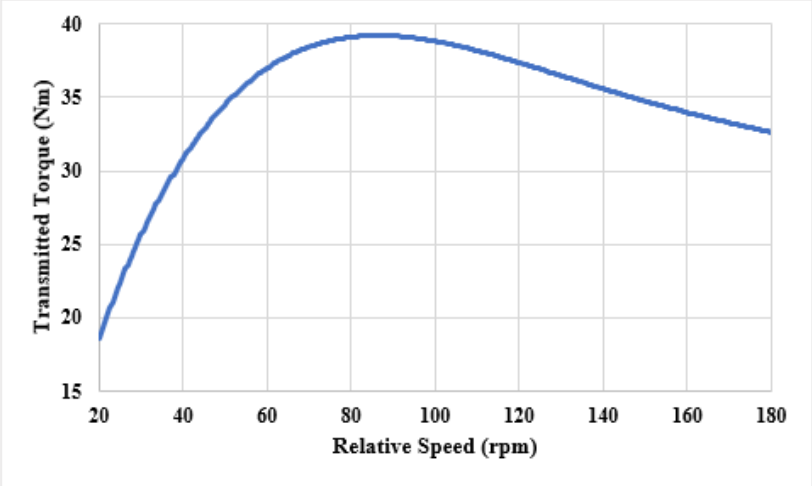

Fig 3. 6 Variation of transmitted torque with relative speed. (15mm slot depth) $G_f = 980\ (\frac{\text{Nm}}{\text{rpm}})/\text{m}^3$ (η ~ 99.1% over an NEDC)

Additionally, Fig 3.7 and Fig 3.8 show the variations of maximum transmitted torque and corresponding relative speed with endring length, respectively. It can be seen that endring length has significant effect on relative speed where the maximum

transmitted torque occurs. Nevertheless, it has a negligible influence on the maximum torque transmitted.

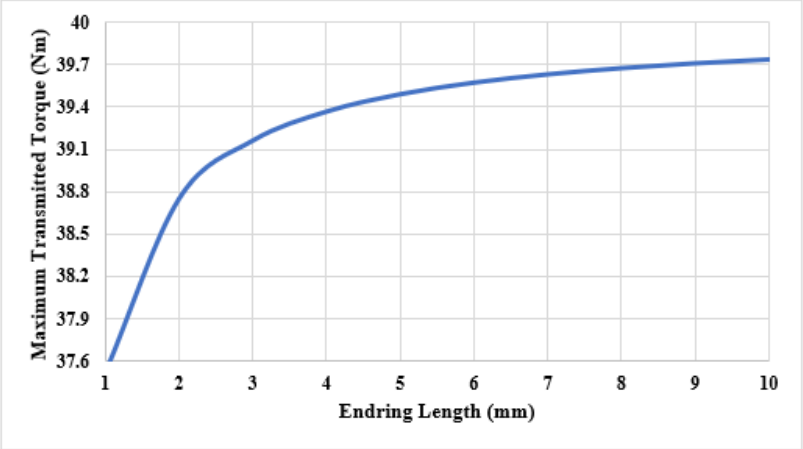

Fig 3. 7 Variation of maximum transmitted torque with endring length. (11 mm slot depth)

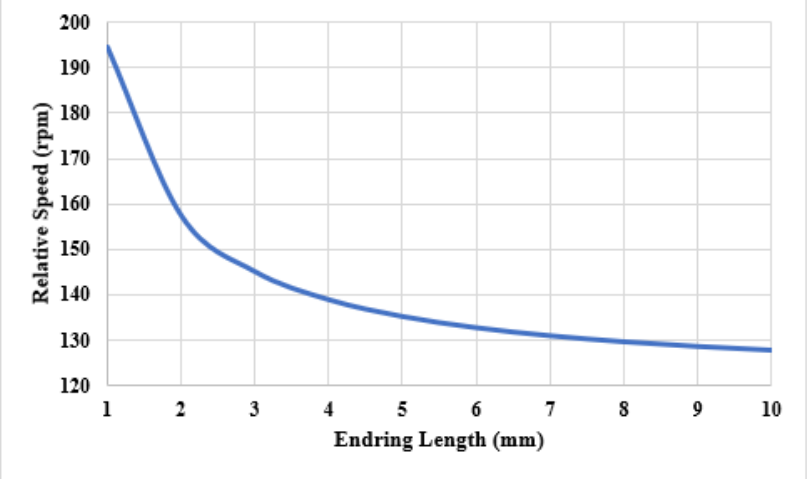

Fig 3. 8 Variation of relative speed corresponding to maximum transmitted torque with endring length. (11 mm slot depth)

Similarly, but a 15mm slot depth, Fig 3.9 and Fig 3.10 show the variation of maximum torque transmitted and corresponding relative speed with endring length, respectively. It can be seen that increasing the endring thickness reduces the relative speed at which the maximum torque occurs.

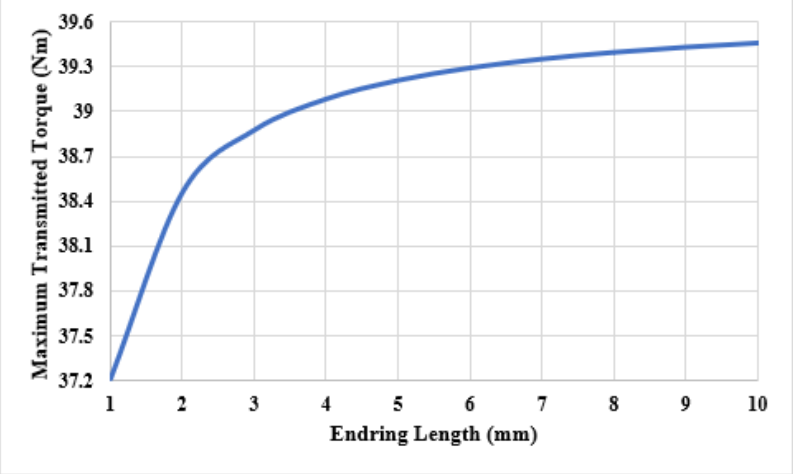

Fig 3. 9 Variation of maximum transmitted torque with endring length. (15 mm slot depth)

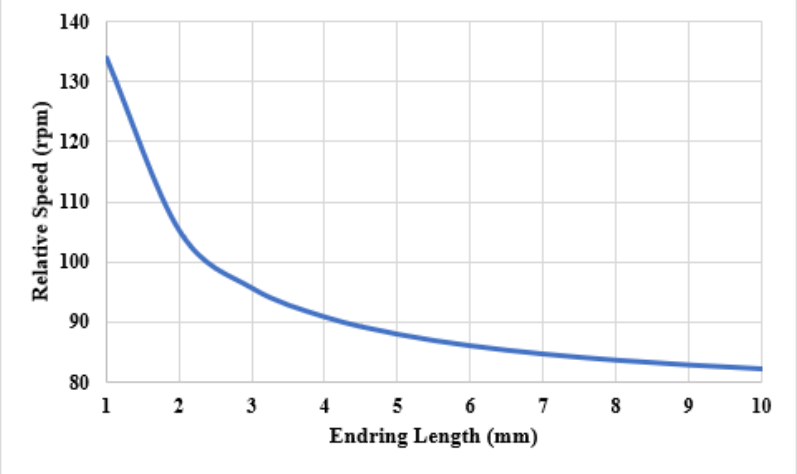

Fig 3. 10 Variation of relative speed corresponding to maximum transmitted torque with endring length. (15 mm slot depth)

3.2.1.1.2 Aluminium squirrel cage

To investigate the influence of the material type on the performance of the PMECCs, a similar study is conducted on the same coupling; however, the squirrel cage rotor material is now assumed to be aluminium. Fig 3.11 shows the variation of transmitted torque with relative speed. It can be seen that when aluminium, which has a lower electrical conductivity than copper, the relative speed at which the maximum torque occurs is now significantly larger, $\alpha \approx 197$ rpm and $\alpha \approx 126.6$ rpm, for 11mm and 15mm slot depths, respectively. However, the maximum transmitted torque remains fairly constant.

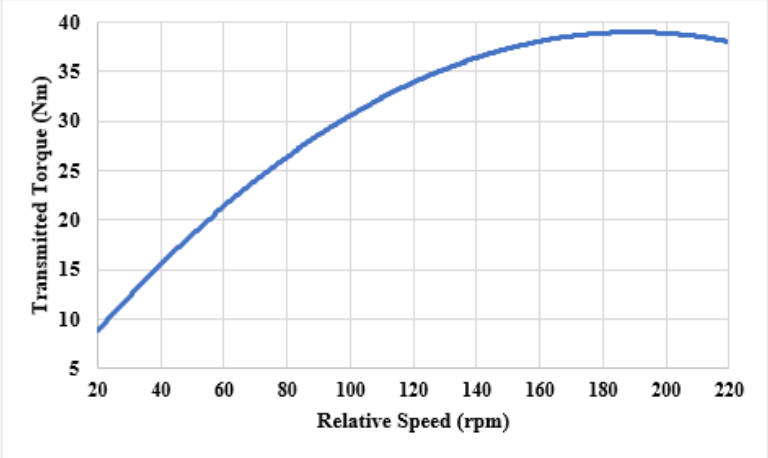

(a) Slot depth 11mm $G_f = 452.7\ (\frac{\text{Nm}}{\text{rpm}})/\text{m}^3$ ($\eta \sim 98$ % over an NEDC)

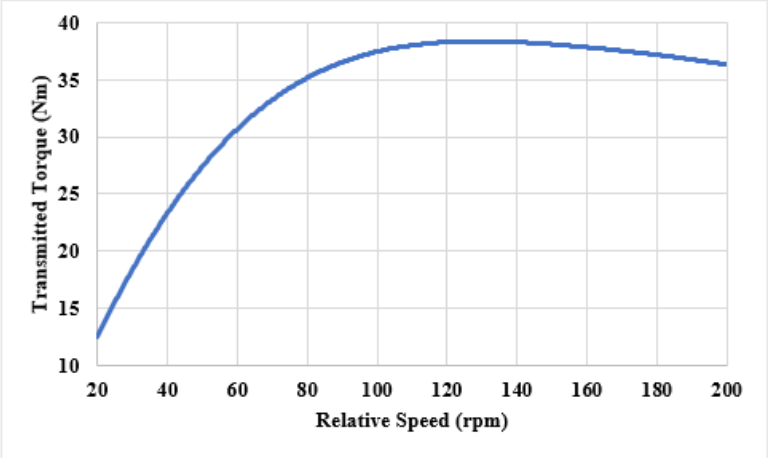

(b) Slot depth 15mm $G_f = 679\ (\frac{\text{Nm}}{\text{rpm}})/\text{m}^3$ ($\eta \sim 98.8\%$ over an NEDC)

Fig 3. 11 Variation of transmitted torque with different slot depth.

Additionally, Fig 3.12 and Fig 3.13 show the variation of maximum torque transmitted and corresponding relative speed with endring length, respectively. It can be seen that endring length has significant effect on relative speed nevertheless, it has a minor influence on the maximum torque transmitted.

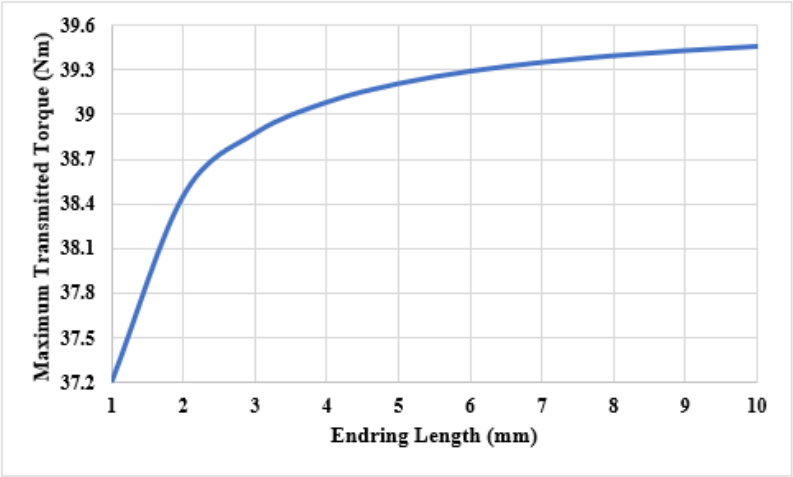

Fig 3. 12 Variation of maximum transmitted torque with endring length. (11 mm slot depth)

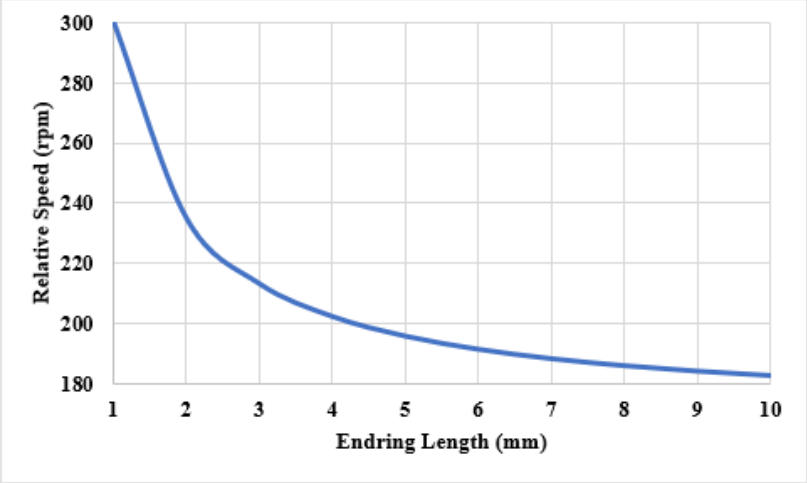

Fig 3. 13 Variation of relative speed corresponding to maximum transmitted torque with endring length. (11 mm slot depth)

Similarly, for 15mm slot depth, Fig 3.14 and Fig 3.15 show the variations of maximum torque transmitted and corresponding relative speed with endring length.

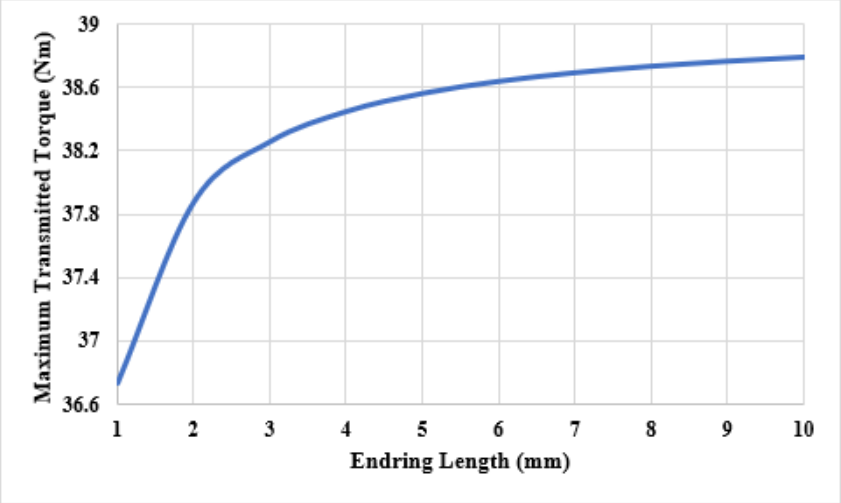

Fig 3. 14 Variation of maximum transmitted torque with endring length. (15 mm slot depth)

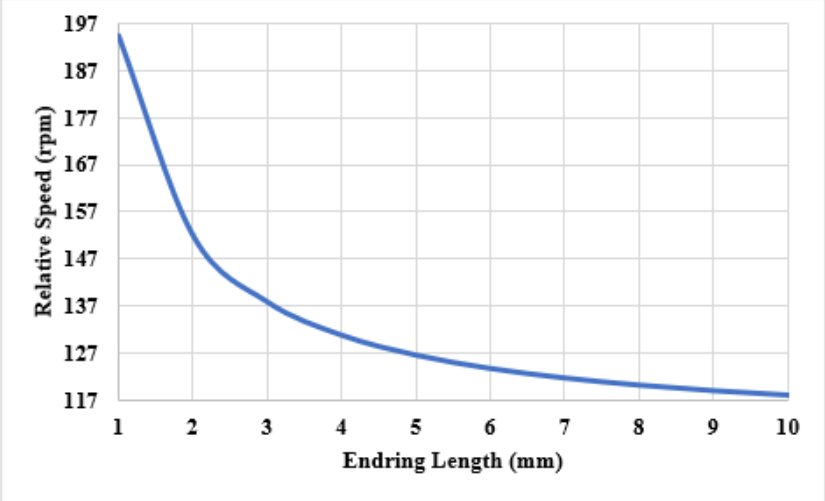

Fig 3. 15 Variation of relative speed corresponding to maximum transmitted torque with endring length. (15 mm slot depth)

3.2.1.2 Squirrel cage PMECCs with 22/23 pole/slot combination

This section concentrates on squirrel cage PMECCs with 22/23 pole/slots combination. Similarly, 3-dimensional finite element analysis is undertaken to

investigate the effect of permanent magnet thickness and slot depth on transmitted torque.

3.2.1.2.1 Copper squirrel cage

Fig 3.16 shows a PMECCs with pole/slot combination of 22/23, and Fig 3.17 illustrates the effect of increasing the thickness of permanent magnets on the coupling developed torque. Again, it can be seen that an optimum magnet thickness exists, for which the transmitted torque is maximum.

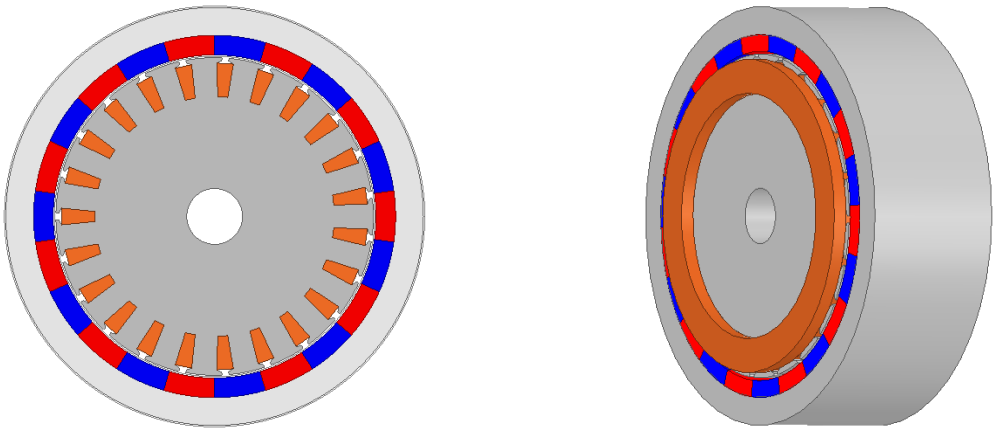

(i) Cross-sectional view (ii) 3D view

Fig 3. 16 PMECCs with pole / slot combination of 22/23

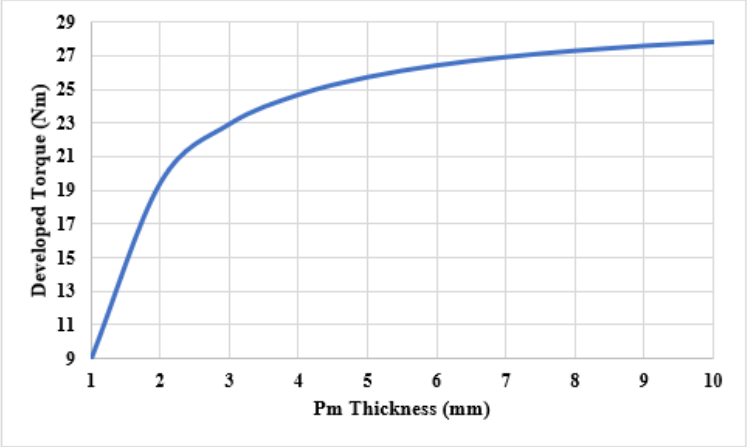

Fig 3. 17 Variation of maximum transmitted torque with PM thickness. (15.5 mm slot depth)

For a PM thickness of 6 mm, and end ring length of 6 mm, Fig 3.18 shows the variation of transmitted torque with relative speed. It can be seen that the relative speed corresponding to the maximum transmitted torque is decreased when the slot depth is increased, resulting in over reduction in the resistance of the bar. However, it can also be seen, that increasing the slot depth results in a slight decrease in the maximum transmitted torque, due to an increase in the leakage reactance of the squirrel cage.

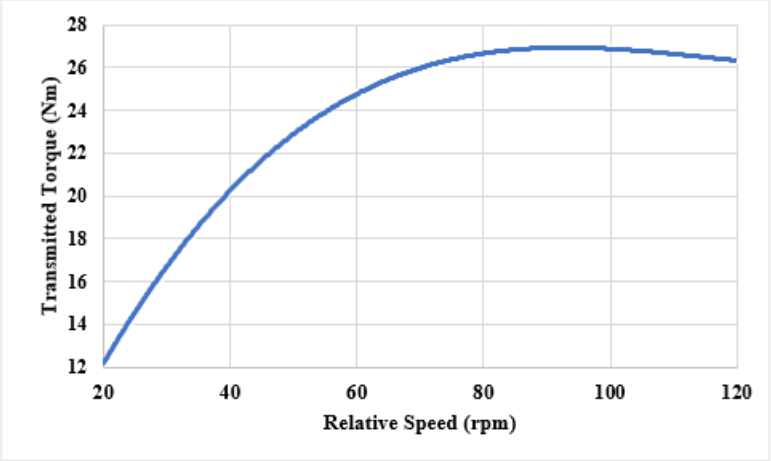

(a) Slot depth 12mm. $G_f = 643\ (\frac{\text{Nm}}{\text{rpm}})/\text{m}^3$ (η ~ 98.7% over an NEDC)

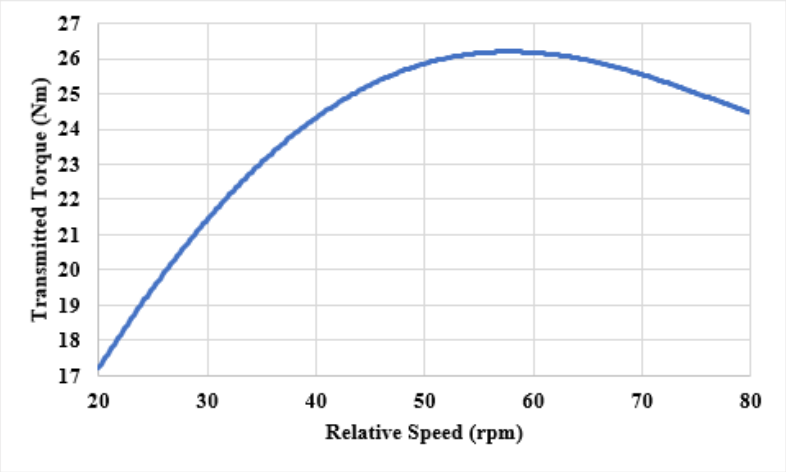

(b) Slot depth 15.5mm. ($G_f = 997\ (\frac{\text{Nm}}{\text{rpm}})/\text{m}^3$ ($\eta \sim 99.1\%$ over an NEDC)

Fig 3. 18 Variation of maximum transmitted torque with relative speed.

Additionally, Fig 3.19 and Fig 3.20 show the variation of maximum transmitted torque and the corresponding relative speed with endring length with copper material. It can be seen that endring length has significant effect on relative speed corresponding to the maximum transmitted torque. However, it can also be seen the effect of endring length on the maximum torque transmitted, is less prominent.

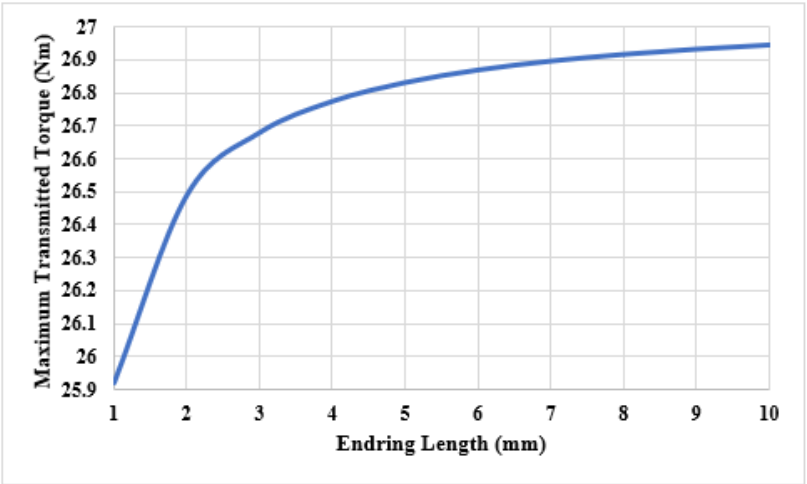

Fig 3. 19 Variation of maximum torque transmitted with endring length. (12mm slot depth)

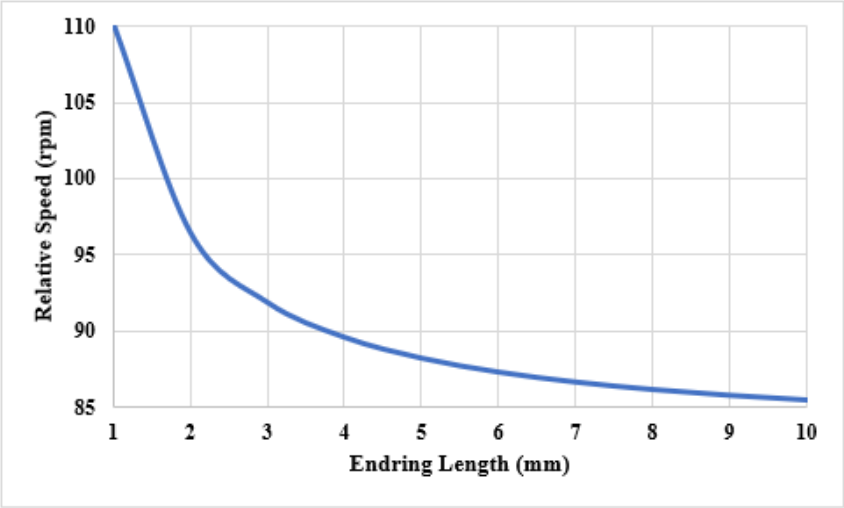

Fig 3. 20 Variation of relative speed corresponding to maximum transmitted torque with endring length. (12mm slot depth)

For a slot depth of 15.5mm, Fig 3.21 and Fig 3.22 show the maximum torque transmitted and the corresponding relative speed with endring length. It can be seen that an endring length exists, beyond which variation in transmitted torque and corresponding relative speed, are negligible.

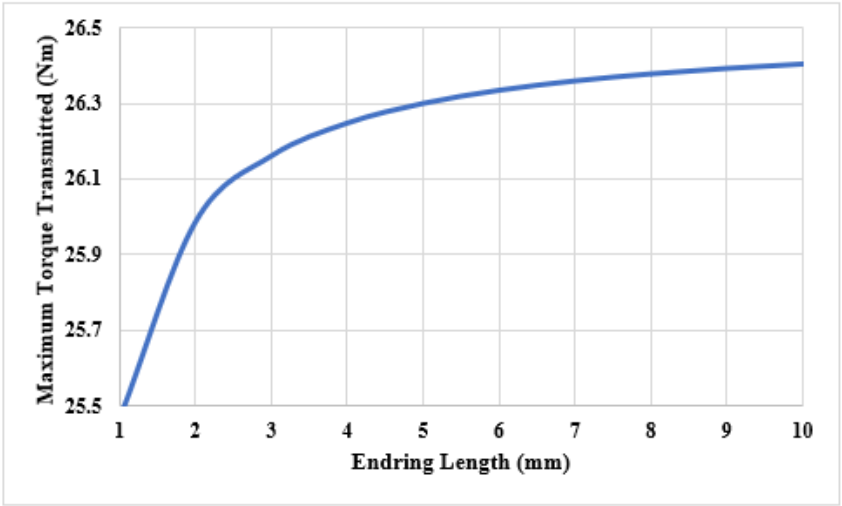

Fig 3. 21 Variation of maximum torque transmitted with endring length. (15.5mm slot depth)

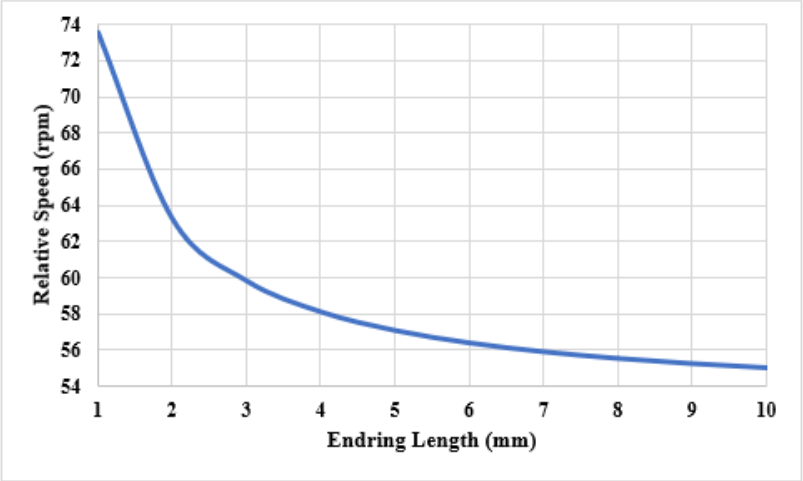

Fig 3. 22 Variation of relative speed corresponding to maximum transmitted torque with endring length. (15.5mm slot depth)

3.2.1.2.2 Aluminium squirrel cage

Furthermore, Fig 3.23 shows the variation of transmitted torque with the relative speed for aluminium squirrel cage. It can be seen that, the higher resistivity of aluminium results in similar maximum transmitted torque, albeit at a much larger corresponding relative speed.

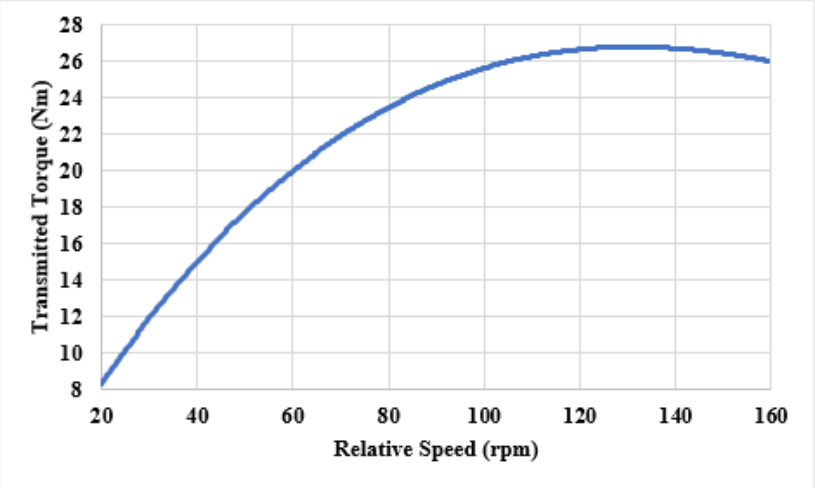

(a) Slot depth 12mm. $G_f = 470\ (\frac{\text{Nm}}{\text{rpm}})/\text{m}^3$ ($\eta \sim 97.9\%$ over an NEDC)

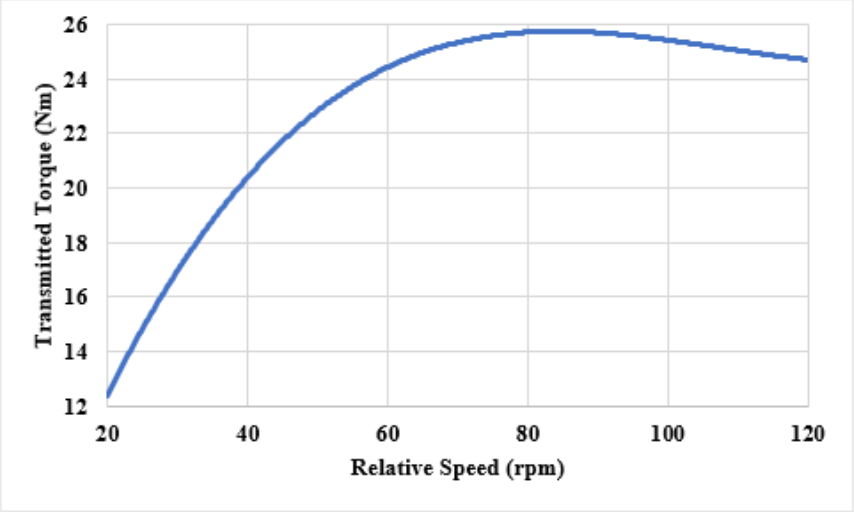

(b) Slot depth 15.5mm $G_f = 668\ (\frac{\text{Nm}}{\text{rpm}})/\text{m}^3$ ($\eta \sim 98.7\%$ over an NEDC)

Fig 3. 23 Variation of transmitted torque with relative speed.

3.2.2 PMECCs with conductive sheet rotor

This section investigates the performance of single sided PMECCs with a conductive sheet rotor. 3-dimensional finite element analysis is employed to investigate the effects of various parameters, such as, PM and conductive sheet thicknesses. Fig 3.24 shows permanent magnets eddy current couplings equipped with sheet conductive rotor. Furthermore, Fig 3.25 and Table 3.3 show the geometry and the parameters of the PMECCs.

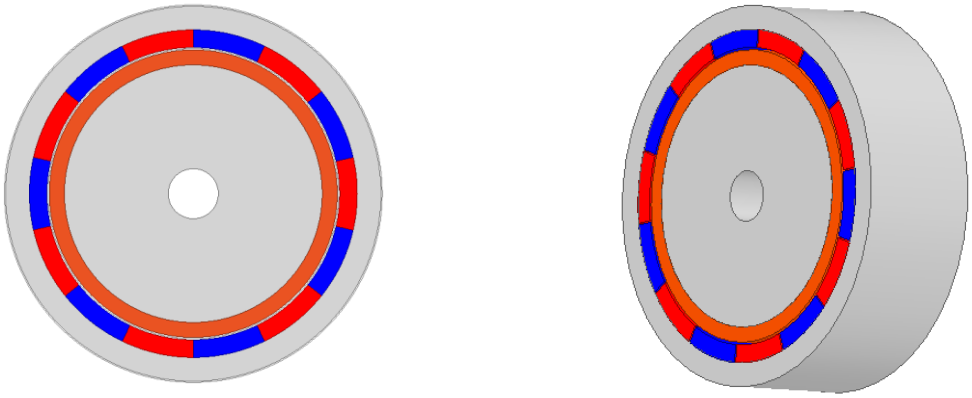

(i) Cross-sectional view (ii) 3D model

Fig 3. 24 PMECCs with a conductive sheet rotor

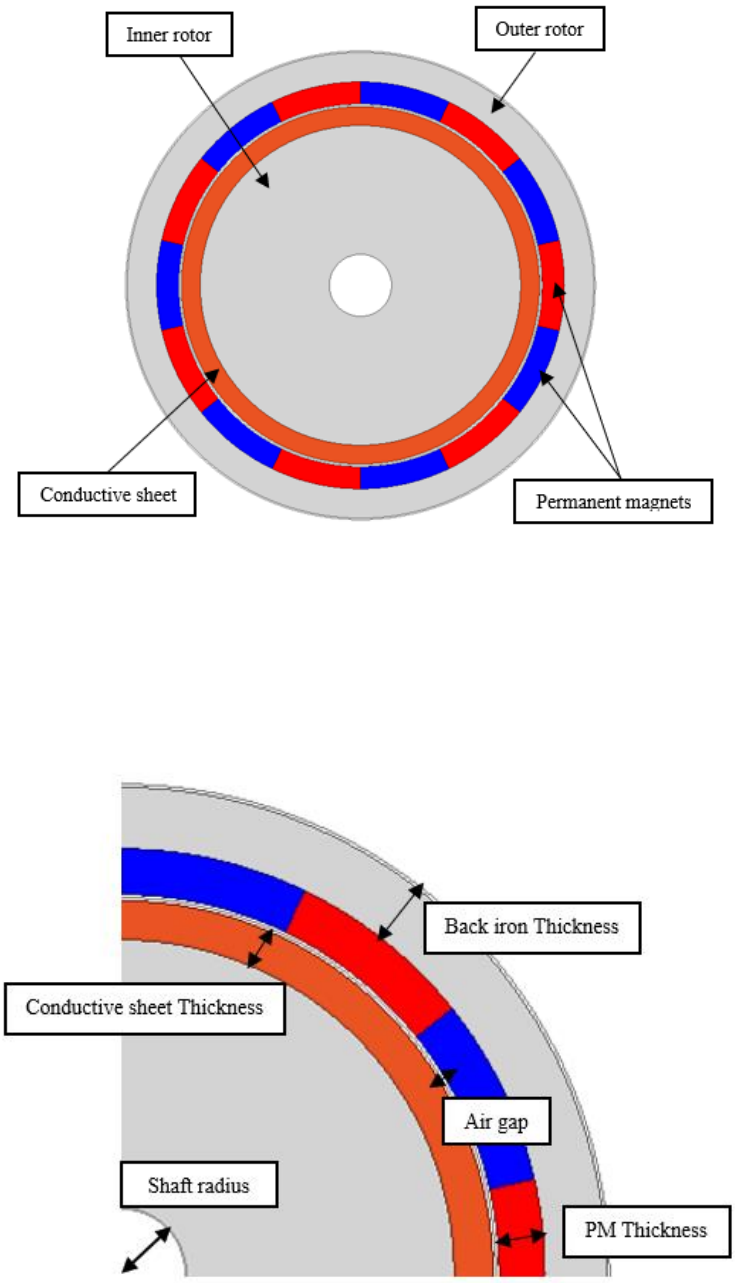

Fig 3. 25 Geometric parameters of the PMECCs

Table 3. 3 Parameters of PMECCs with conductive sheet rotor

Parameter name	Value/ type
Active diameter	150 mm
Air gap length	1 mm
Number of poles	14
Conductive sheet thickness	2-12 mm
Permanent magnets	NdFeB 30
Conductive ring material	Copper / Aluminium
Axial Length	50 mm

3.2.2.1 Copper conductive sheet

Fig 3.26 shows the variation of the transmitted torque with the thickness of permanent magnets, when conductive rotor thickness is kept at 2 mm. Moreover, for a magnet thickness of 7mm, Fig 3.27 shows the variation of the relative speed corresponding to the maximum transmitted torque with the thickness of the conductive sheet. It can be seen, that when a current a conductive sheet is employed, significantly larger transmitted torques are achieved. However, this is a realised at the expense of transmission efficiency, since these maximum transmitted torques occurs at significantly larger relative speeds, approximately an order of magnitude larger than those encountered in squirrel cage topologies. Furthermore, Fig 3.28 shows the variation of transmitted torque for different copper conductive sheet thicknesses.

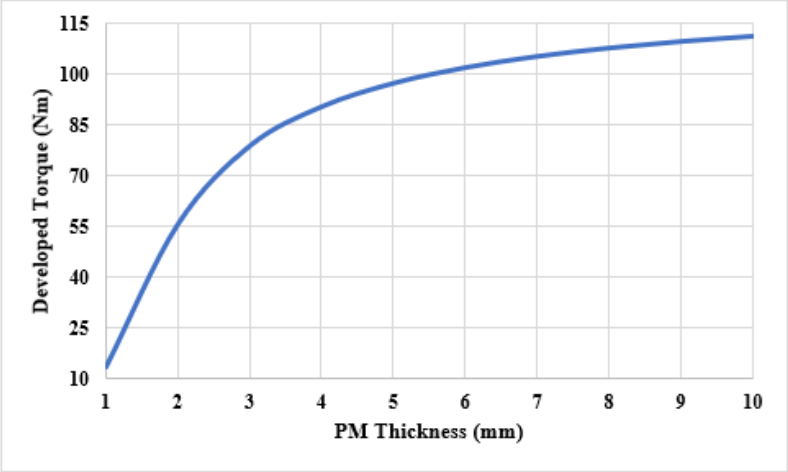

Fig 3. 26 Variation of maximum transmitted torque with PM thickness. (2 mm conductive sheet thickness)

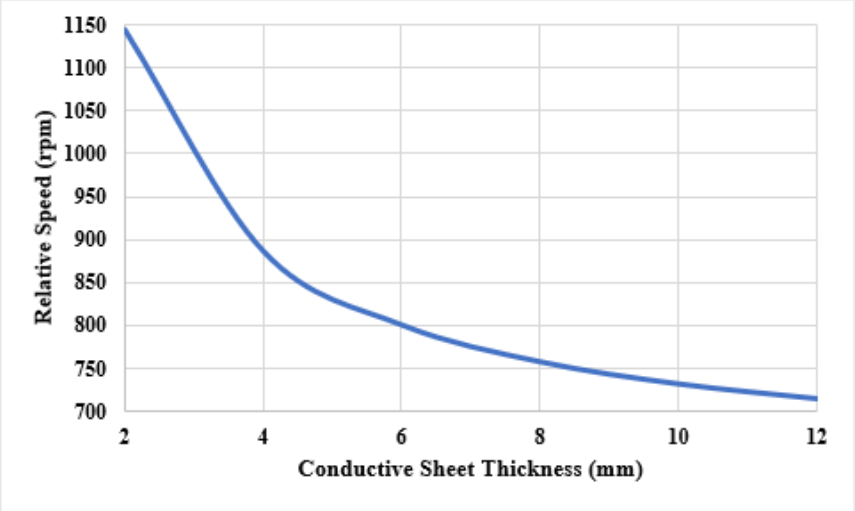

Fig 3. 27 Variation of relative speed corresponding to the maximum transmitted torque with the thickness of conductive sheet. (7 mm PM thickness)

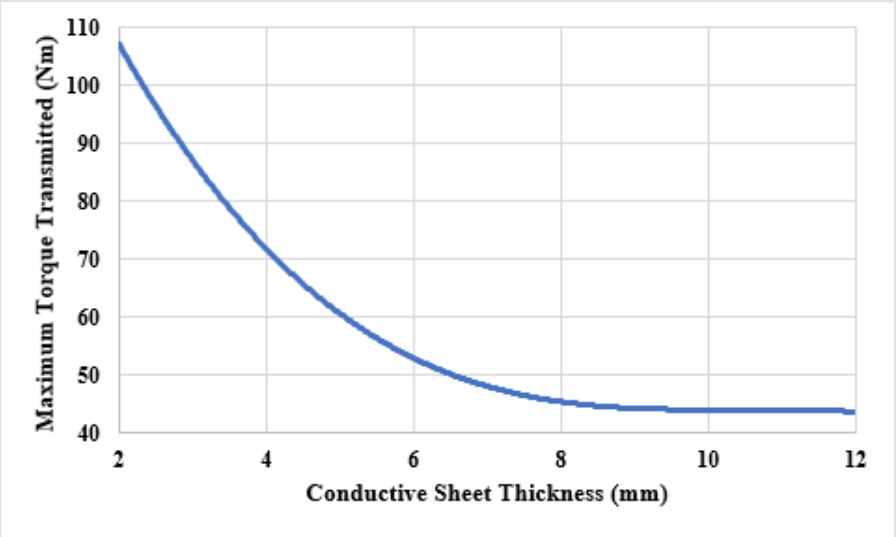

Fig 3. 28 Variation of maximum torque transmitted with different copper conductive sheet thickness.(6mm copper conductive sheet $G_f = 150\ (\frac{\mathrm{Nm}}{\mathrm{rpm}})/\mathrm{m}^3$) ($\eta$ ~ 94.2% over an NEDC)

3.2.2.2 Aluminium conductive sheet

In addition, Fig 3.29 shows the variation of transmitted torque of this coupling with aluminium material with different conductive sheet thickness, and Fig 3.30 shows the variation of the relative speed corresponding to the maximum transmitted torque with the thickness of the conductive sheet.

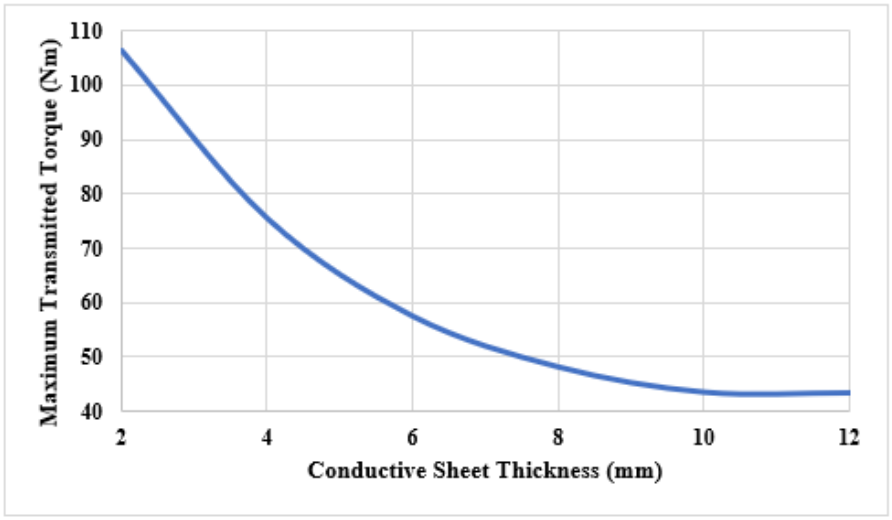

Fig 3. 29 Variation of maximum transmitted torque with different Aluminium conductive sheet thickness.(6mm Aluminium conductive sheet $G_f =$ $100\ (\frac{\text{Nm}}{\text{rpm}})/\text{m}^3$ ($\eta \sim 91.7\%$ over an NEDC)

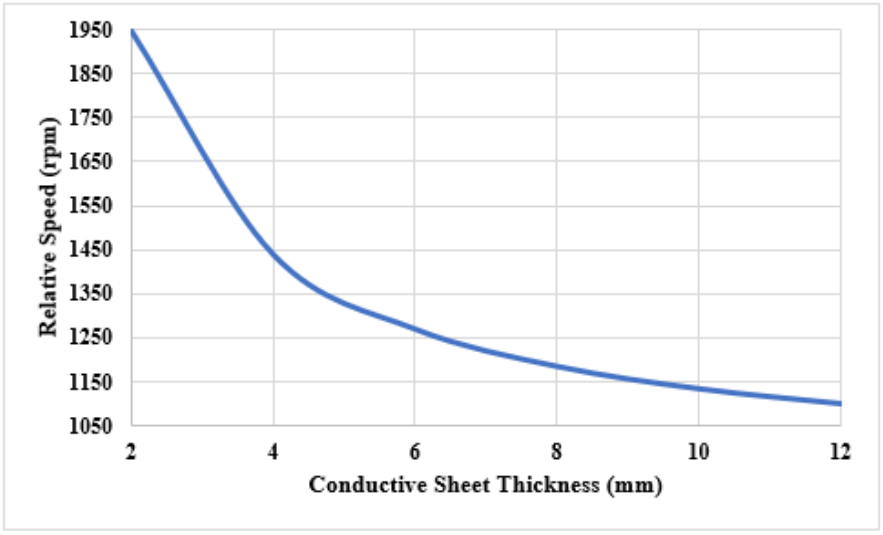

Fig 3. 30 Variation of relative speed corresponding to the maximum transmitted torque with the thickness of conductive sheet. (7 mm PM thickness)

3.3 Double sided permanent magnet eddy current couplings

3.3.1 PMECCs with Squirrel cage rotor type

This section investigates the performance of double-sided PMECCs with a squirrel cage rotor. Fig 3.31 shows a general cross-section of double-sided permanent magnet eddy current couplings equipped with a squirrel cage rotor. Fig 3.32 and Table 3.4 show the geometry and the parameters of PMECCs, under investigation.

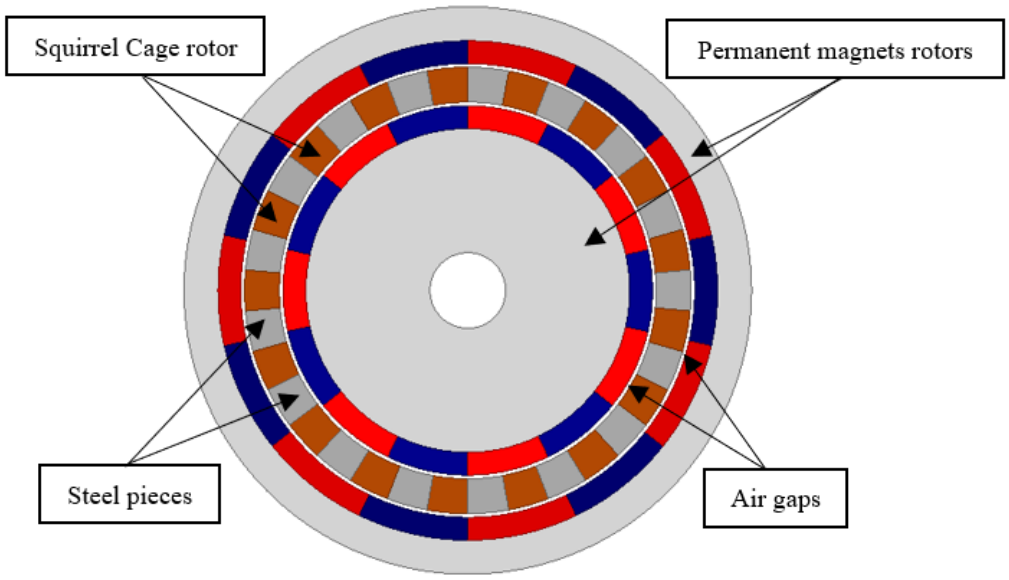

Fig 3. 31 Cross-sectional view of double-sided PMECC

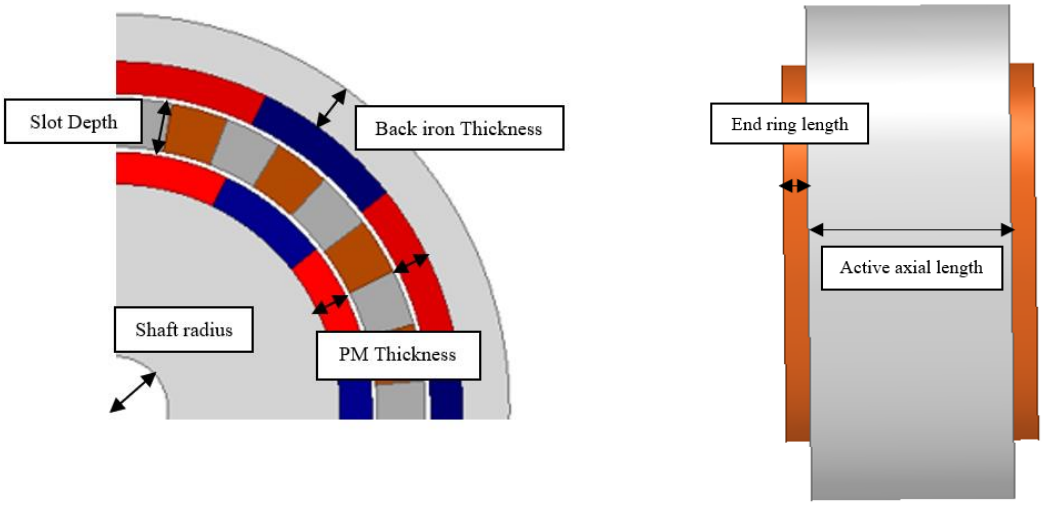

Fig 3. 32 Geometrical parameters of the PMECCs

Table 3. 4 Parameters of double sided squirrel cage PMECCs

Parameter name	Value/ type
Active diameter	150 mm
Air gap length	1mm
Number of poles	14/ 22
Number of slots	17 / 23
Permanent magnets	NdFeB 30
Squirrel cage material	Copper / Aluminium
Axial Length	50mm

3.3.1.1 14/17 pole/slot combination

This section investigates the performance of double sided PMECCs with 14/17 pole/slot combination. Fig 3.33 shows a complete design of double sided PMECC equipped with squirrel cage rotor.

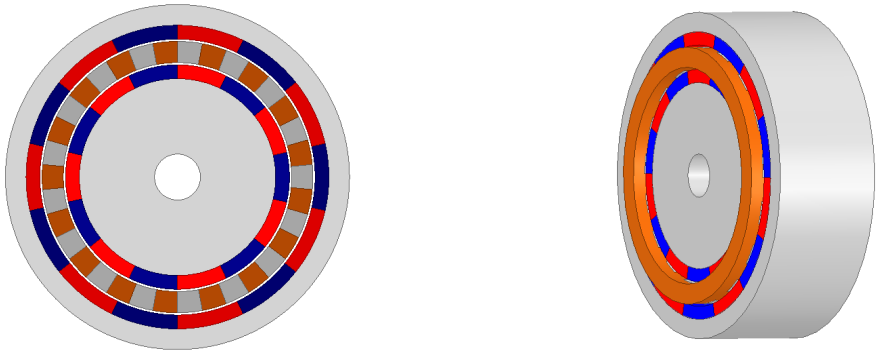

(i) Cross-sectional view (ii) 3D view

Fig 3. 33 Double sided PMECCs with pole / slot combination of 14/17

3.3.1.1.1 Copper squirrel cage

With a selected PM and endring thickness of 6 mm and 5mm respectively, Fig 3.34 shows the variation of the transmitted torque with relative speed for a 9.2 mm slot depth. It can be seen that the maximum transmitted torque is significantly larger than that of the single sided counterpart, however, this occurs at a much larger speed, $\alpha \approx$ 535 rpm. In addition, Fig 3.35 shows the variation of the transmitted torque with relative speed when the slot depth is increased to 13.4 mm, It can be seen that this results in a significant reduction in the relative speed, $\alpha \approx$ 364 rpm.

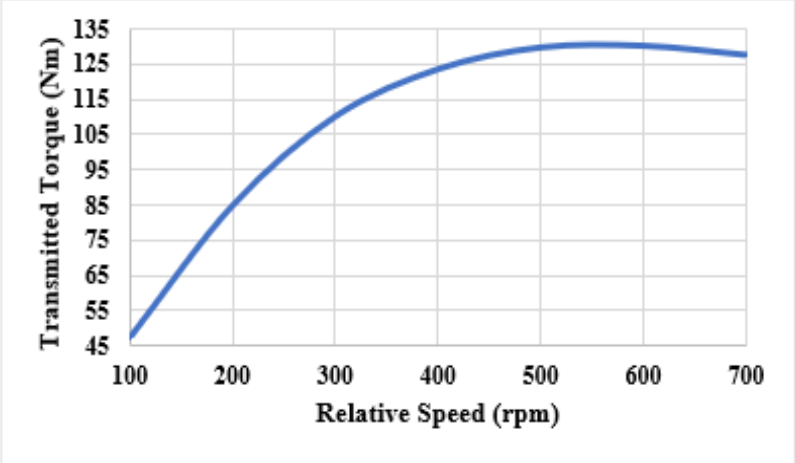

Fig 3. 34 Variation of transmitted torque with relative speed. (9.2 mm slot depth) ($G_f = 535\ (\frac{\text{Nm}}{\text{rpm}})/\text{m}^3$) ($\eta$ ~ 98.4% over an NEDC)

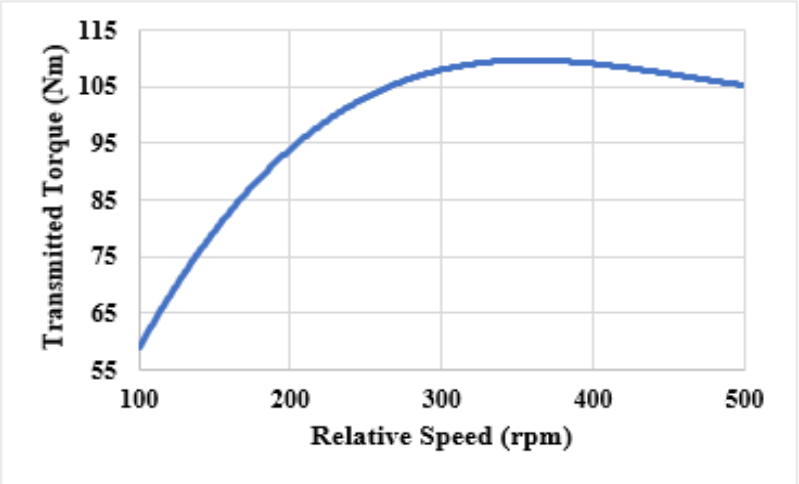

Fig 3. 35 Variation of transmitted torque with relative speed. (13.4 mm slot depth) ($G_f = 691\ (\frac{\text{Nm}}{\text{rpm}})/\text{m}^3$) ($\eta$ ~ 98.6% over an NEDC)

3.3.1.1.2 Aluminium squirrel cage

Similarly, with a selected PM and endring thickness of 6 mm and 5mm respectively, Fig 3.36 shows the variation of the transmitted torque with relative speed for a 9.2 mm slot depth. It can be seen that the maximum transmitted torque is significantly

larger than that of the single sided counterpart, however, this occurs at a much larger speed, $\alpha \approx 790$ rpm. In addition, Fig 3.37 shows the variation of the transmitted torque with relative speed when the slot depth is increased to 13.4 mm, It can be seen that this results in a significant reduction in the relative speed, $\alpha \approx 525$ rpm.

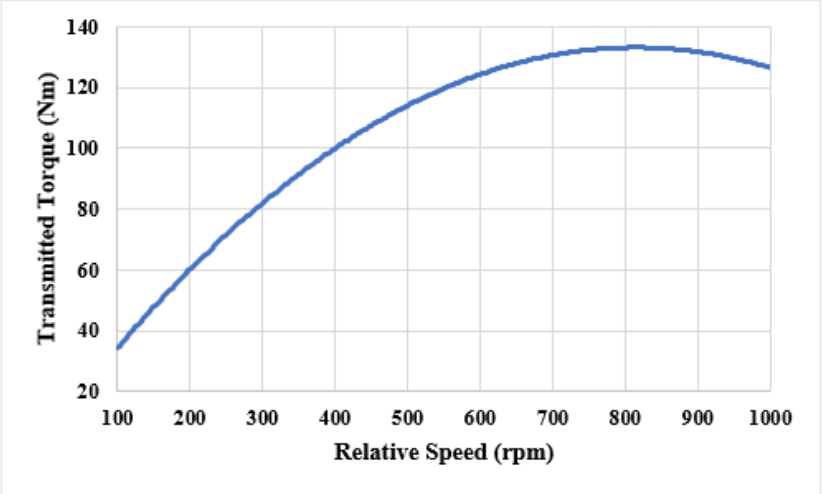

Fig 3. 36 Variation of transmitted torque with relative speed. (9.2 mm slot depth) ($G_f = 358\ (\frac{\text{Nm}}{\text{rpm}})/\text{m}^3$) ($\eta \sim 97.6\%$ over an NEDC)

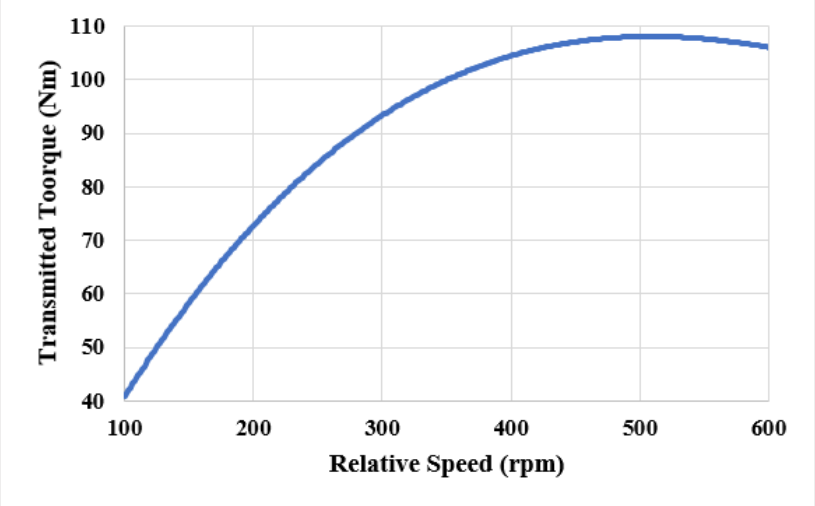

Fig 3. 37 Variation of transmitted torque with relative speed. (13.4 mm slot depth) ($G_f = 474\ (\frac{\text{Nm}}{\text{rpm}})/\text{m}^3$) ($\eta \sim 98.2\%$ over an NEDC)

3.3.1.2 PMECCs with Squirrel cage rotor and 22/23 pole/slot

This section investigates the performance of double sided PMECCs with a squirrel cage rotor equipped with 22/23 pole/slot combination. Fig 3.38 shows schematics of double sided permanent magnets eddy current couplings equipped with squirrel cage.

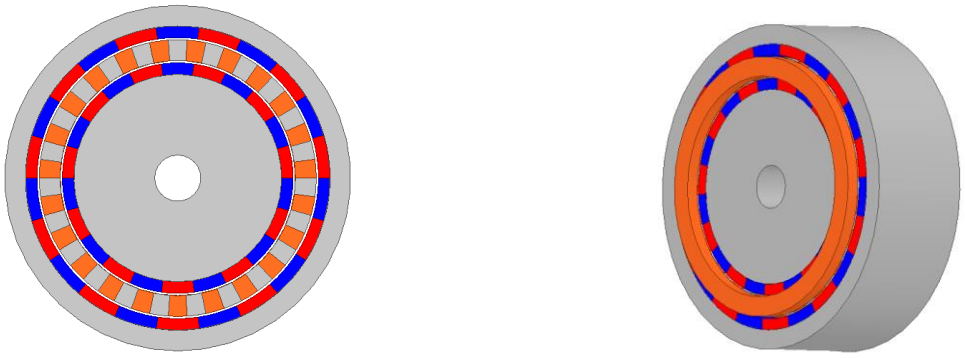

Fig 3. 38 Double sided PMECCs with pole / slot combination of 22-23

3.3.1.2.1 Copper squirrel cage

With a selected PM and endring thickness of 6 mm and 6mm respectively, Fig 3.39 shows the variation of the transmitted torque with relative speed for a 9 mm slot depth. It can be seen that the maximum transmitted torque is significantly larger than that of the single sided counterpart, however, this occurs at a much larger speed, $\alpha \approx$ 442.7 rpm. In addition, Fig 3.40 shows the variation of the transmitted torque with relative speed when the slot depth is increased to 13.1 mm, It can be seen that this results in a significant reduction in the relative speed, $\alpha \approx$ 293.6 rpm.

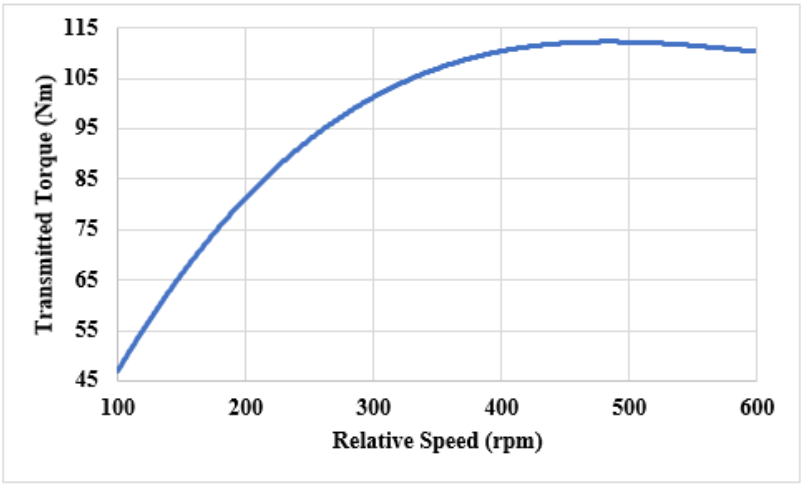

Fig 3. 39 Variation of transmitted torque with relative speed. (9 mm slot depth) ($G_f = 497\ (\frac{\mathrm{Nm}}{\mathrm{rpm}})/\mathrm{m}^3$) ($\eta \sim 98.6\%$ over an NEDC)

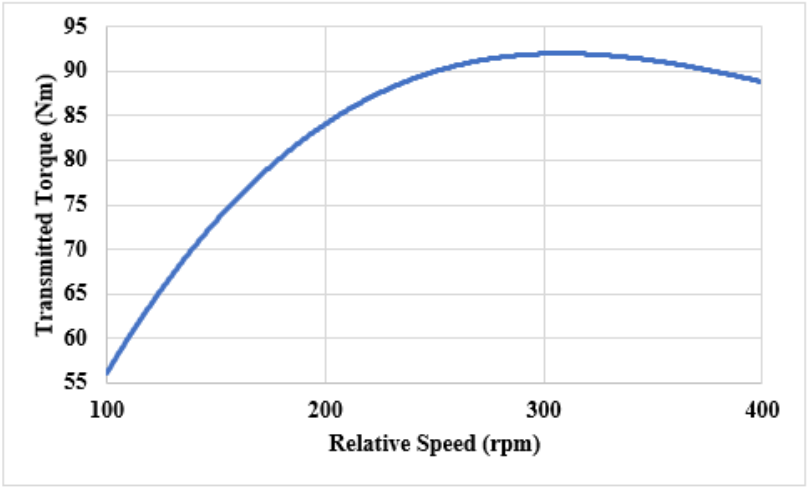

Fig 3. 40 Variation of transmitted torque with relative speed. (13.1 mm slot depth) ($G_f = 650\ (\frac{\mathrm{Nm}}{\mathrm{rpm}})/\mathrm{m}^3$) ($\eta \sim 98.7\%$ over an NEDC)

3.3.1.2.2 Aluminium squirrel cage

Similarly, with a selected PM and endring thickness of 6 mm and 6mm respectively, Fig 3.41 shows the variation of the transmitted torque with relative speed for a 9 mm slot depth. It can be seen that the maximum transmitted torque is significantly larger than that of the single sided counterpart, however, this occurs at a much larger speed,

$\alpha \approx$ 670.6 rpm. In addition, Fig 3.42 shows the variation of the transmitted torque with relative speed when the slot depth is increased to 13.1 mm, It can be seen that this results in a significant reduction in the relative speed, $\alpha \approx$ 429.7 rpm.

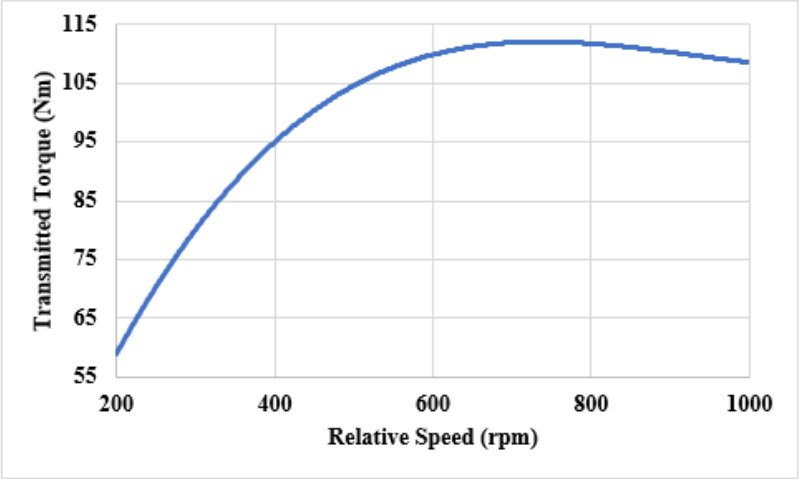

Fig 3. 41 Variation of transmitted torque with relative speed. (9 mm slot depth) ($G_f = 320\ (\frac{\text{Nm}}{\text{rpm}})/\text{m}^3$) ($\eta \sim$ 97.7% over an NEDC)

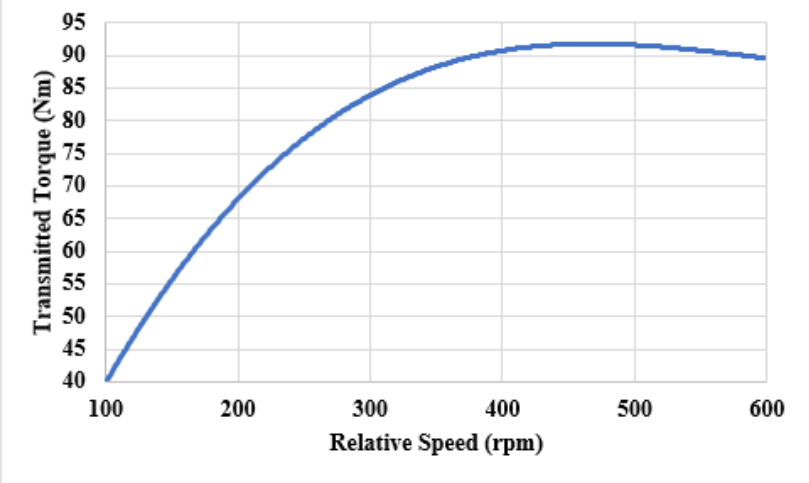

Fig 3. 42 Variation of transmitted torque with relative speed. (13.1 mm slot depth) ($G_f = 433\ (\frac{\text{Nm}}{\text{rpm}})/\text{m}^3$) ($\eta \sim$ 98.2% over an NEDC)

3.3.2 PMECCs with conductive sheet

This section investigates the performance of double sided PMECCs with a conductive sheet rotor. Fig 3.43 shows double sided permanent magnets eddy current couplings equipped with sheet conductive rotor. Furthermore, Fig 3.44 and Table 3.5 show the geometric details and the parameters of the PMECCs.

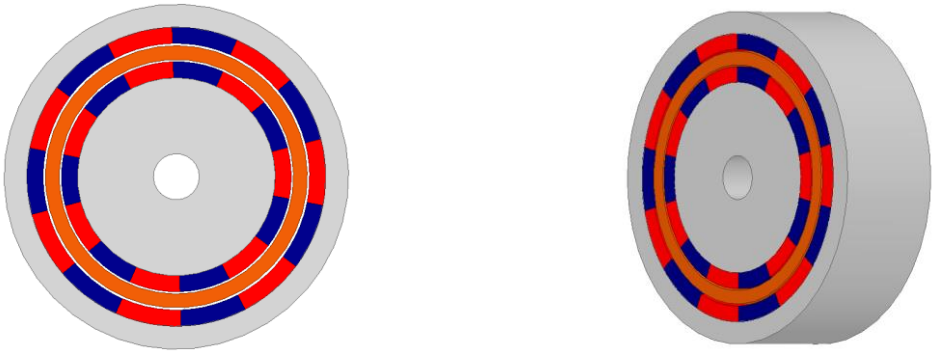

(i) 2D cross section (ii) 3D model

Fig 3. 43 PMECCs with conductive sheet rotor

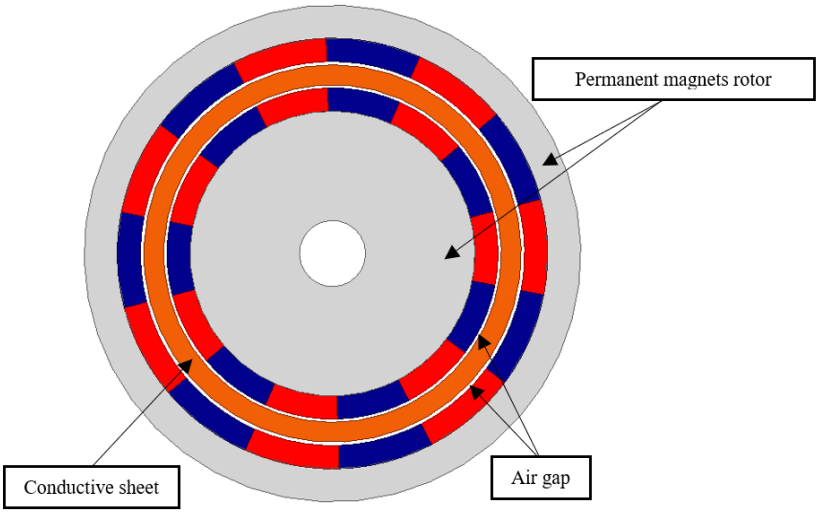

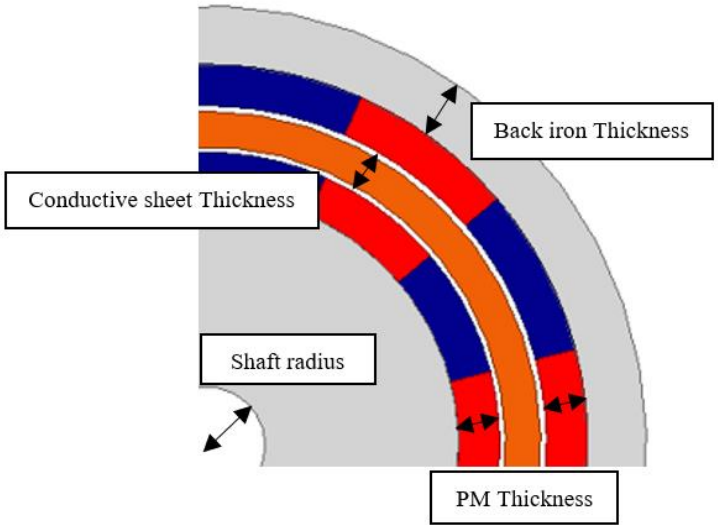

Fig 3. 44 Geometric details of the PMECCs

Table 3. 5 Parameters of double sided PMECCs with conductive sheet rotor

Parameter name	Value/ type
Active diameter	150 mm
Air gap length	1 mm
Number of poles	14
Conductive sheet thickness	4-8 mm
Permanent magnets	NdFeB 30
Conductive ring material	Copper / Aluminium
Axial Length	50 mm

3.3.2.1 Copper squirrel cage

For a PM thickness of 7 mm, Fig 3.45 shows the Variation of relative speed corresponding to the maximum transmitted torque with the thickness of conductive sheet, and Fig 3.46 shows the variation of transmitted torque, for different conductive sheet thicknesses. It can be seen that increasing the thickness of the conductive sheet results in reduced maximum transmitted torque.

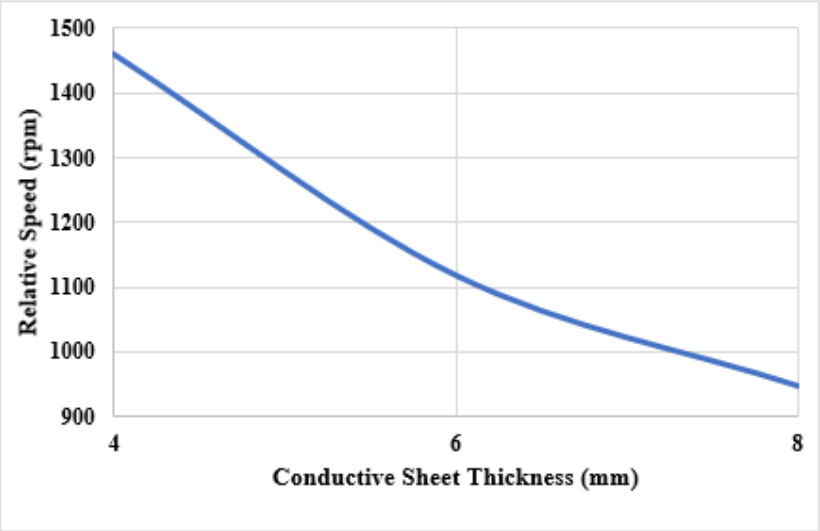

Fig 3. 45 Variation of relative speed corresponding to the maximum transmitted torque with the thickness of conductive sheet.

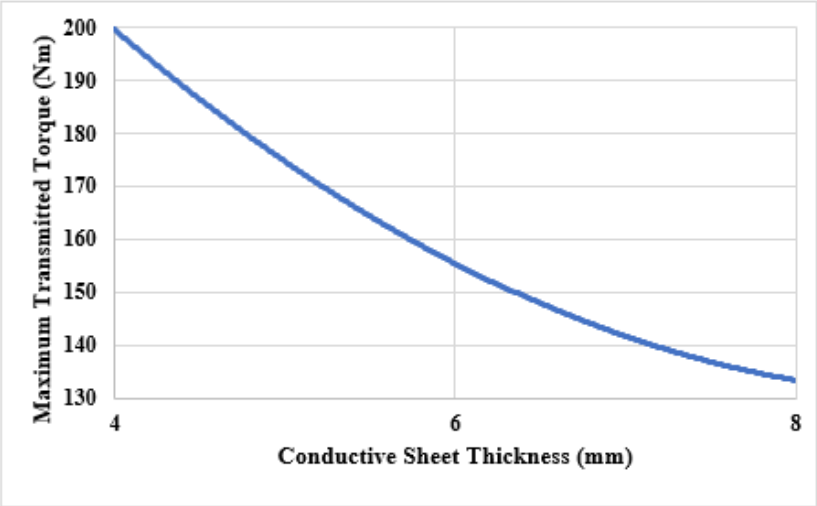

Fig 3. 46 Variation of maximum transmitted torque with different copper conductive sheet thickness.(6mm copper conductive sheet $G_f = 316\ (\frac{\mathrm{Nm}}{\mathrm{rpm}})/\mathrm{m}^3$)

(η ~ 97.2% over an NEDC)

3.3.2.2 Aluminium conductive sheet

Similarly, Fig 3.47 shows the variation of relative speed corresponding to the maximum transmitted torque with the thickness of conductive sheet. and Fig 3.48 shows the variation of transmitted torque, for different conductive sheet thicknesses It can be seen that, similarly to copper, increasing the thickness of the conductive sheet results in reduced maximum transmitted torque.

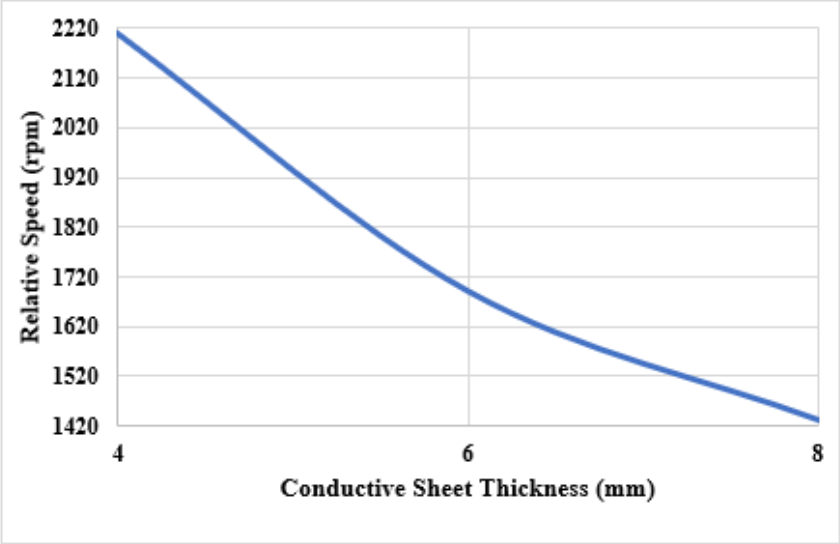

Fig 3. 47 Variation of relative speed corresponding to the maximum transmitted torque with the thickness of conductive sheet.

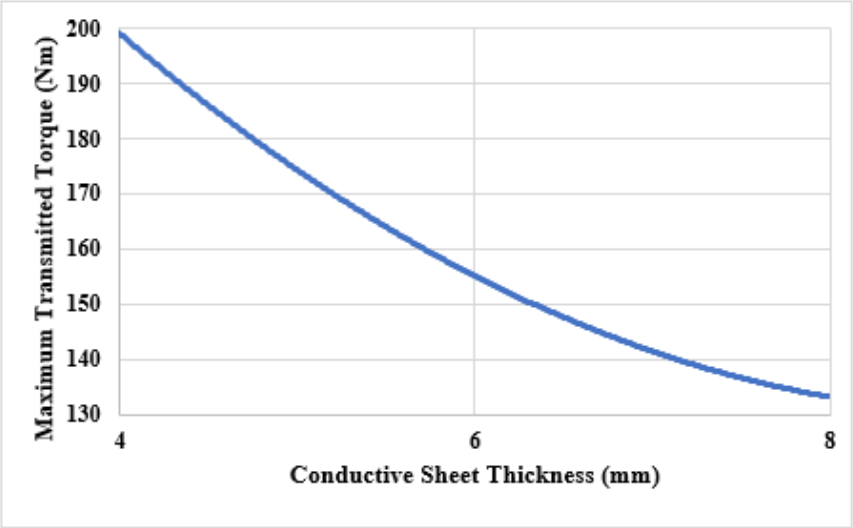

Fig 3. 48 Variation of maximum transmitted torque with different Aluminium conductive sheet thickness. (6mm Aluminium conductive sheet $G_f = 206\ (\frac{\mathrm{Nm}}{\mathrm{rpm}})/\mathrm{m}^3$) ($\eta \sim 95.8\%$ over an NEDC)

3.4 Discussion and conclusion

In this chapter simulation and analysis studies of different radial-field topologies of PMECCs using Copper and Aluminium as conductive materials are presented. It has been shown, that for both Copper and Aluminium using a squirrel cage result in significantly more efficient PMECCs. Employing squirrel cage rotor type improves the torque density of the coupling and strengthen the magnetic field in the air gap. Furthermore, as it can be seen in Table 3.6 for the single sided squirrel cage PMECCs with 14/17 pole/slot combination, and 11mm /15mm slot depth both coupling produce similar transmitted torque however, at different slip speeds, and this is due to reduction in the total impedance of the coupling and increase in the out power. employing conductor sheets may result in higher torque transmission capabilities, but this is at the expense of efficiency. Therefore, the use of conductor sheet material should be reserved to damper/braking applications, instead of power transmission applications. Furthermore, a goodness factor is introduced, in order to assess and compare the performance of the various topologies. The factor is essentially the damping factor volumetric density is essentially the damping coefficient at zero slip-speed. Moreover, Table 3.6 shows a comparison between all different designs' parameters and efficiency. Furthermore, and as would be expected the axial thickness of the end ring has significant effect since it is part of the circuits where the induced current will flow.

Table 3. 6 Comparison between all different radial designs' parameters and efficiency.

Type of conductive rotor	Volume (mm^3)	Poles/slot	Slot/sheet depth (mm)	Sided	Material	G_f	α (rpm)	T_m(Nm)	η %
Squirrel cage	0.883	14/17	11	SS	Cu	680	136.4	39.8	98.7
Squirrel cage	0.883	14/17	15	SS	Cu	980	88.5	39.6	99.1
Squirrel cage	0.883	14/17	11	SS	Alu	452.7	197	39.7	98
Squirrel cage	0.883	14/17	15	SS	Alu	679	126.6	39.5	98.8
Squirrel cage	0.883	22/23	12	SS	Cu	643	87.44	26.87	98.7
Squirrel cage	0.883	22/23	15.5	SS	Cu	997	58	26.2	99.1
Squirrel cage	0.883	22/23	11	SS	Alu	470	133	26.6	97.9
Squirrel cage	0.883	22/23	15.5	SS	Alu	668	80.2	25.9	98.7
Sheet	0.883	14	6	SS	Cu	150	800	52.5	94.2
Sheet	0.883	14	6	SS	Alu	100	1260	57	91.7
Squirrel cage	0.883	14/17	9.2	DS	Cu	535	535	131	98.4
Squirrel cage	0.883	14/17	13.4	DS	Cu	691	364	110.4	98.6
Squirrel cage	0.883	14/17	9.2	DS	Alu	358	790	127.2	97.6
Squirrel cage	0.883	14/17	13.4	DS	Alu	474	525	109.7	98.2
Squirrel cage	0.883	22/23	9	DS	Cu	497	442.7	109	98.6
Squirrel cage	0.883	22/23	13.1	DS	Cu	650	293.6	92	98.7
Squirrel cage	0.883	22/23	9	DS	Alu	320	670.6	112	97.7
Squirrel cage	0.883	22/23	13.1	DS	Alu	433	429.7	92.1	98.2
Sheet	0.883	14	6	DS	Cu	316	1115	155	97.2
Sheet	0.883	14	6	DS	Alu	206	1680	150	95.8

Chapter 4
An Investigation and design of different structures of axial field permanent magnet eddy current couplings

4.1 Introduction

In this chapter different sections are introduced to investigate multiple topologies of an axial permanent magnets eddy current couplings PMECCs and compare their performance and efficiency with PMECCs radial field topology. A single-sided (SS) and double-sided (DS) topologies equipped with an axially magnetized surface permanent magnets (SPM) forming a permanent magnet rotor, and two different types of conductive rotors are studied. The first rotor structure is a squirrel cage rotor, and the second rotor structure is a conductive sheet rotor. 3-dimensional finite elements is used and a transient solution is adopted to simulate, analyse, and compare the results, of different topologies. Moreover, squirrel cage pole/slot combinations have been selected to the best of least common factor to have low cogging torque, also, the conductive material has been chosen based on the difference of their electrical properties to examine their influence on the PMECCs efficiency and performance. Table 4.1 shows the parameters of the different designs considered.

Table 4. 1 Considered designs of PMECCs.

Topology type	Single sided - 3D				Double sided - 3D			
Conductive rotor structure	Squirrel cage		sheet		Squirrel cage		sheet	
Conductive rotor material	Cu	Al	Cu	Al	Cu	Al	Cu	Al
Pole and Pole/Slot combination	14/17		14		14/17		14	
Conductive sheet thickness (mm)			4-8				4-8	

4.2 Single sided permanent magnet eddy current couplings

4.2.1 PMECCs with Squirrel cage rotor type.

This section investigates the performance of axial single-sided PMECCs with a squirrel cage rotor. Fig. 4.1 and Table 4.2 show geometry and the parameters of PMECCs, respectively.

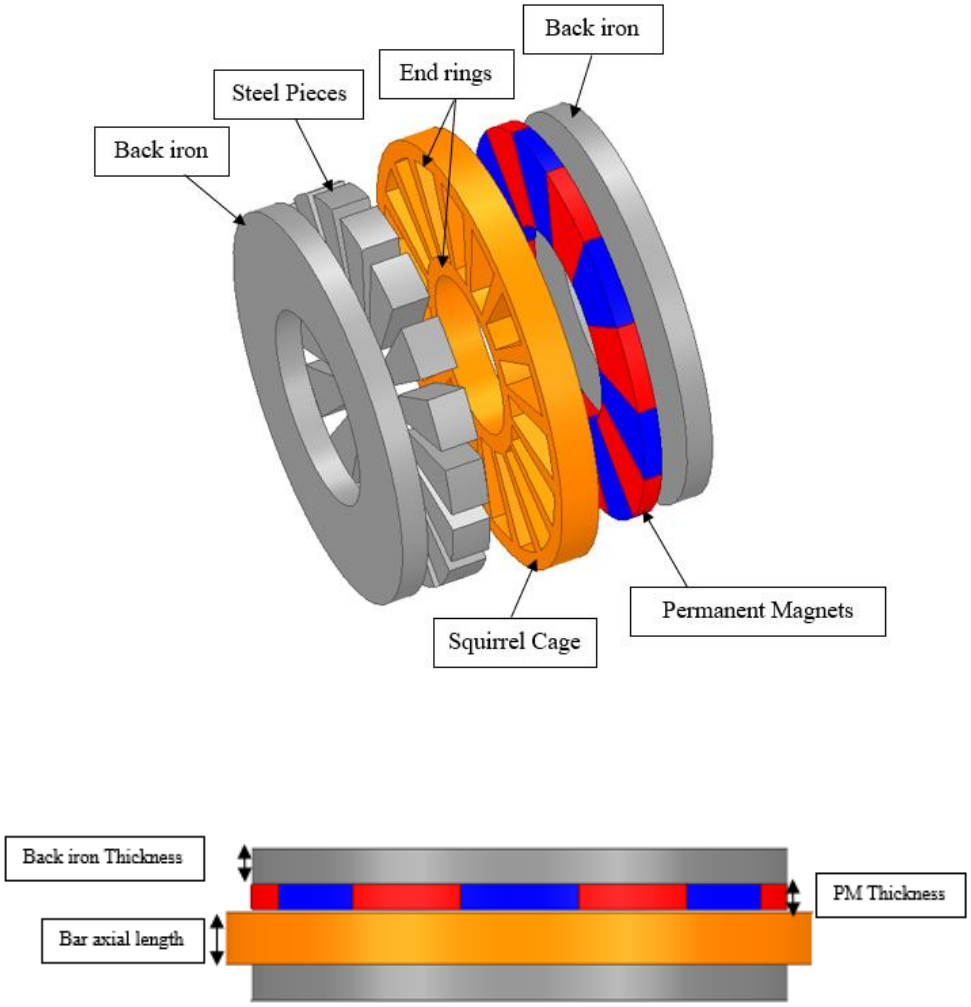

Fig 4. 1 Schematic of an axial single sided squirrel cage PMECC

Table 4. 2 Parameters of an axial single sided squirrel cage PMECCs

Parameter name	Value/ type
Active diameter	150 mm
Air gap length	1mm
Number of poles	14
Number of bars	17
Permanent magnets	NdFeB
Squirrel cage material	Copper / Aluminium
Squirrel cage bar axial length	14.6 / 22 mm

4.2.1.1 Copper squirrel cage

Finite element analysis is employed in order to study the effect of permanent magnets thickness on the developed torque, and the impact of the squirrel cage bars axial length, and end ring radial thickness on relative speed corresponding to the maximum transmitted torque. Fig. 4.2 shows the variation of maximum transmitted torque with the thickness of permanent magnets. It can be seen that the maximum transmitted torque increases with increasing the permanent magnets thickness due to increase in magnetomotive force, albeit with diminishing returns as the magnet thickness is further increased. Furthermore,

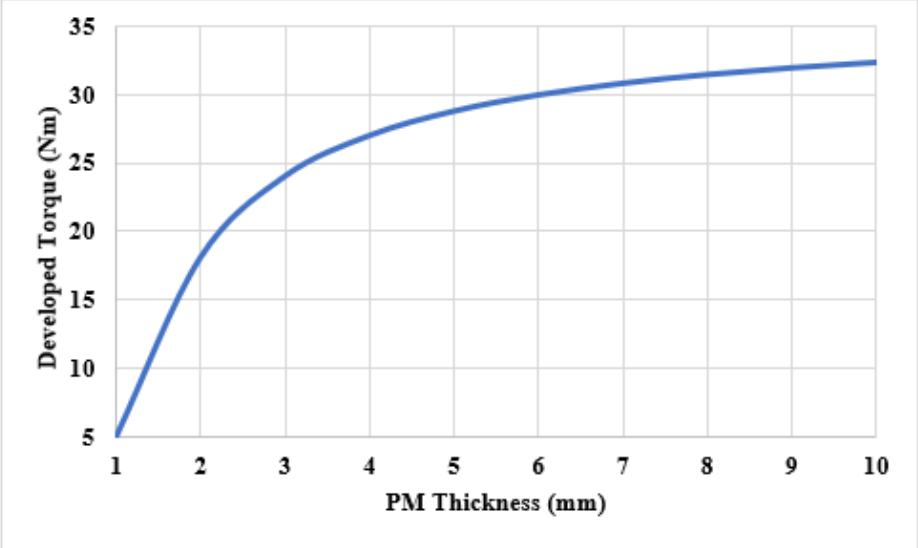

Fig 4. 2 Variation of maximum transmitted torque with thickness of PM.

with a chosen permanent magnet of 7 mm of thickness and 6 mm endring radial thickness, Fig.4.3 shows the variation of transmitted torque with relative speed of this coupling with copper material and bars axial length of 14.6 mm. It can be seen for this coupling the maximum transmitted torque occurs $\alpha \approx 136$ rpm. Furthermore, Fig.4.4 shows the variation of the transmitted torque with relative speed of the same PMECC, when the bars axial length is increased to 22 mm. The result indicates that,

by increasing the amount of copper material, the relative speed α, at which the maximum torque occurs is now reduced to $\alpha \approx 80$ rpm, as would be expected.

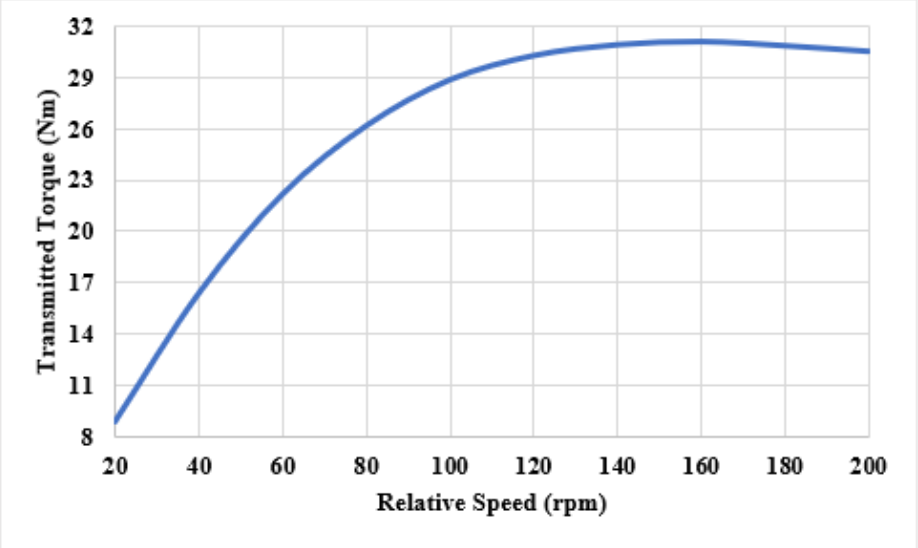

Fig 4. 3 Variation of transmitted torque with relative speed. (14.6 mm bar axial length). $G_f = 605\ (\frac{\text{Nm}}{\text{rpm}})/\text{m}^3$ ($\eta \sim 98.2\%$ over an NEDC)

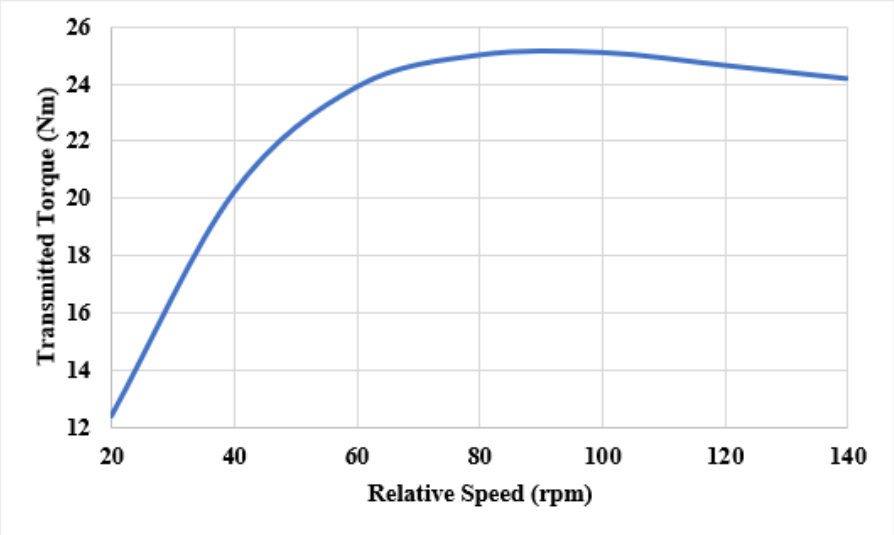

Fig 4. 4 Variation of transmitted torque with relative speed. (22 mm bar axial length). $G_f = 713\ (\frac{\text{Nm}}{\text{rpm}})/\text{m}^3$ ($\eta \sim 98.8\%$ over an NEDC)

Additionally, Fig 4.5 and Fig 4.6 show the variation of maximum transmitted torque and corresponding relative speed with endring radial thickness, respectively. It can

be seen that the endring radial thickness has significant effect on relative speed where the maximum transmitted torque occurs. But, it has a negligible influence on the maximum transmitted torque.

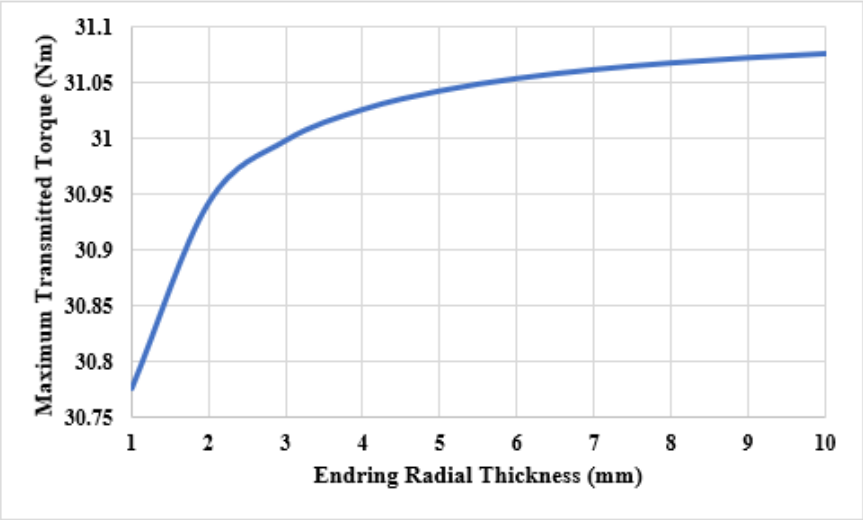

Fig 4. 5 Variation of maximum transmitted torque with endring radial thickness. (14.6 mm bar axial length).

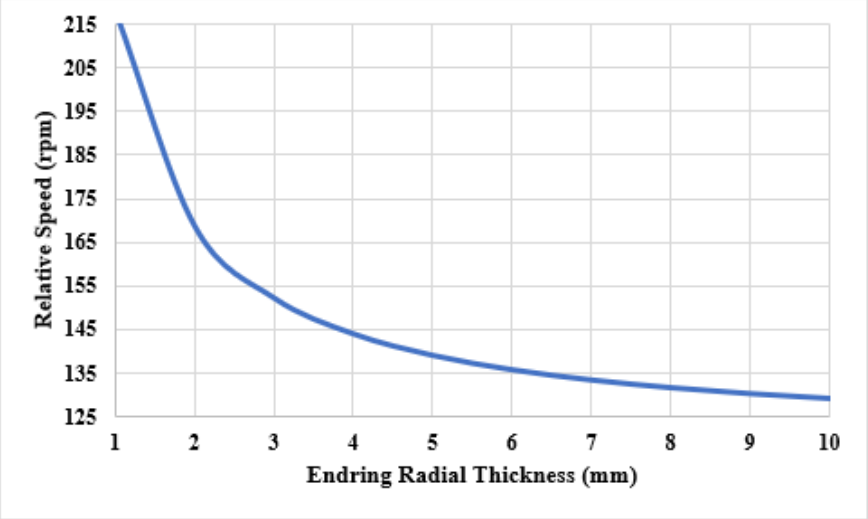

Fig 4. 6 Variation of relative speed corresponding to maximum transmitted torque with endring radial thickness. (14.6 mm bar axial length)

Similarly, but with a 22 mm bar axial length, Fig 4.7 and Fig 4.8 show the variation of maximum torque transmitted and corresponding relative speed with endring radial

thickness, respectively. It can be seen that relative speed at which the maximum torque occurs is reduced with increasing the endring radial thickness. It can also be seen that the maximum transmitted torque is relatively unaffected, while the corresponding relative speed descreases with increaing the radial thickness of the endring.

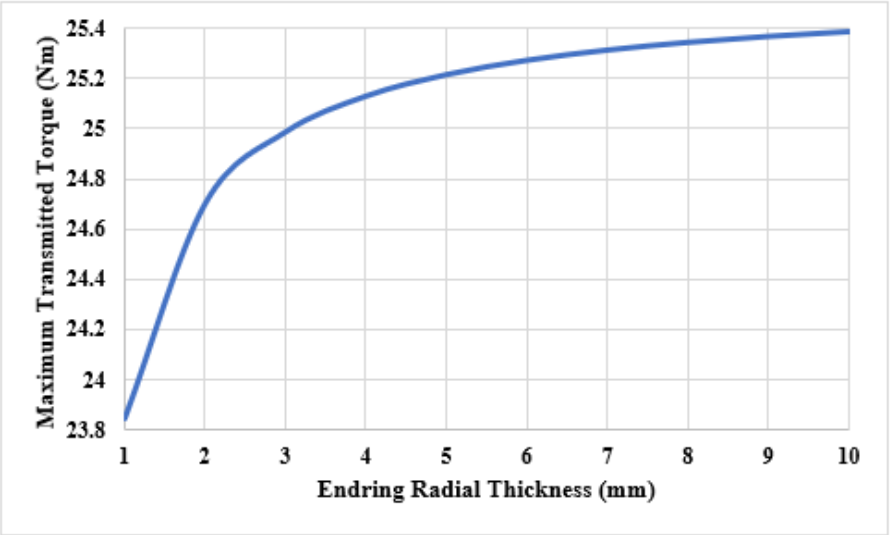

Fig 4. 7 Variation of maximum transmitted torque with endring radial thickness. (22 mm bar axial length)

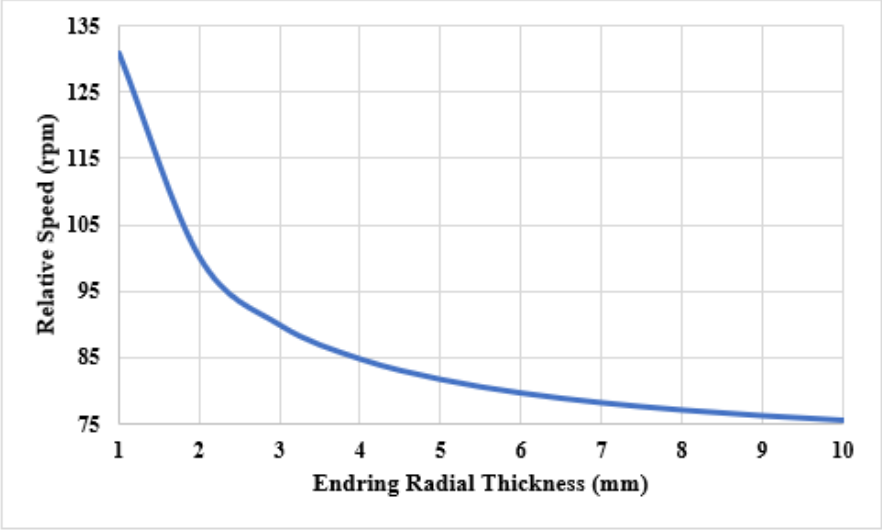

Fig 4. 8 Variation of relative speed corresponding to maximum transmitted torque with endring radial thickness. (22 mm bar axial length)

4.2.1.2 Aluminum squirrel cage

To explore the influence of the material type on the performance of this PMECC a similar study is conducted on the same coupling, however, the squirrel cage rotor material is now assumed to be made from aluminium. Fig. 4.9 shows the variation of transmitted torque with relative speed. It can be seen that the relative speed corresponding to maximum transmitted torque is now significantly larger due to lower electrical conductivity of aluminium. $\alpha \approx 224$ rpm and $\alpha \approx 122$ rpm for 14.6 mm and 22 mm bar axial length, respectively . However, the maximum transmitted torque remains fairly constant.

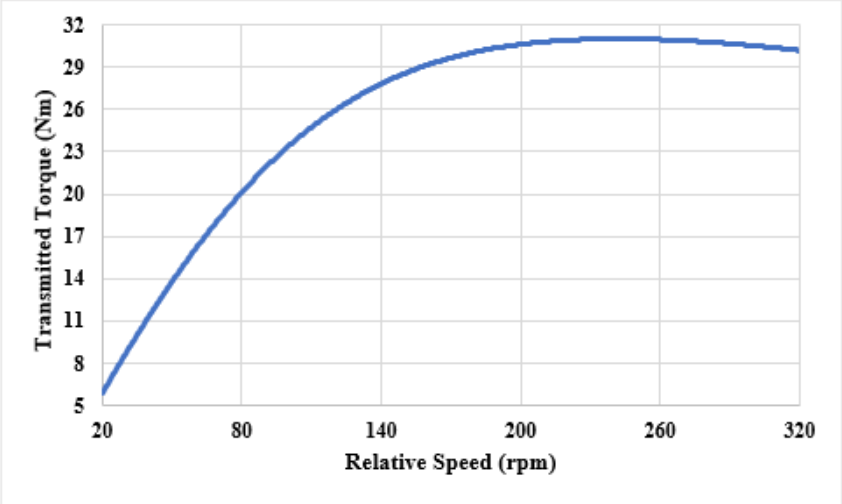

(a) 14.6 mm of bar axial length $G_f = 370\ (\frac{\text{Nm}}{\text{rpm}})/\text{m}^3$ ($\eta \sim 97.1\%$ over an NEDC)

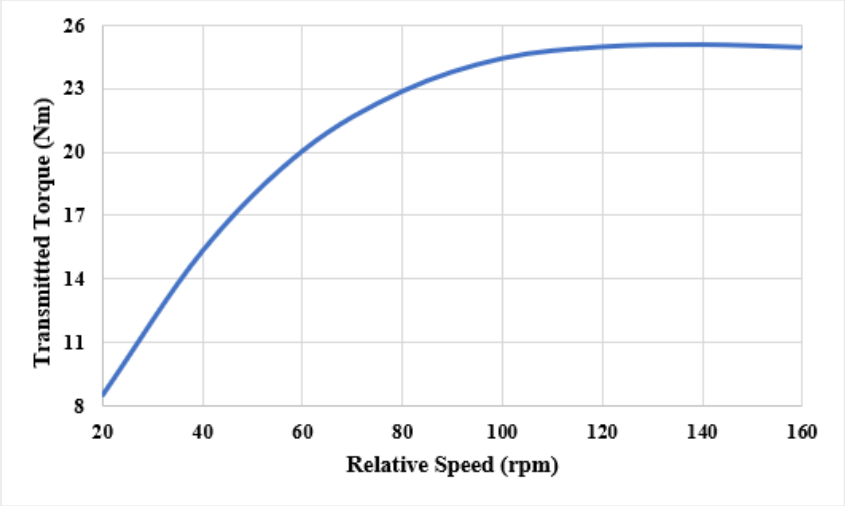

(b) 22 mm of bar axial length $G_f = 469\ (\frac{\text{Nm}}{\text{rpm}})/\text{m}^3$ ($\eta \sim 97.9\%$ over an NEDC)

Fig 4. 9 Variation of transmitted torque with relative speed for different bar axial length. (6mm endring radial thickness)

Furthermore, Fig 4.10 and Fig 4.11 show the variation of maximum torque transmitted and corresponding relative speed with endring radial thickness respectively. It can be seen that endring radial thickness has considerable influence on relative speed, yet, it has a negligible effect on the maximum torque transmitted.

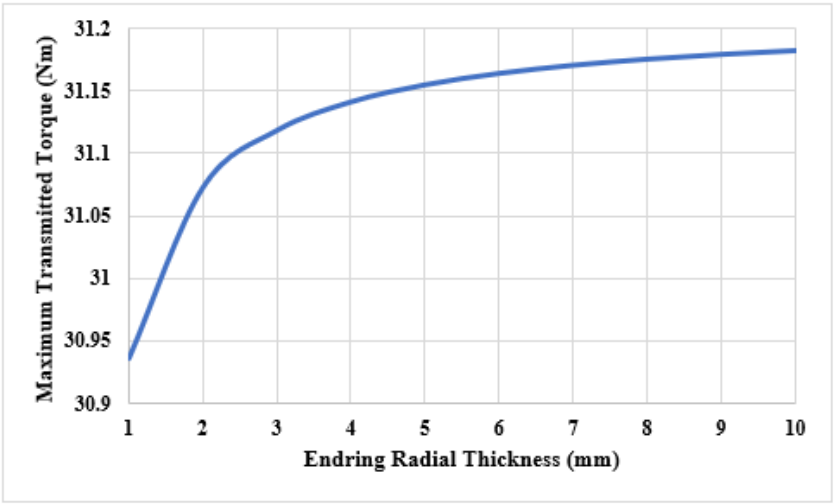

Fig 4. 10 Variation of maximum transmitted torque with endring radial thickness. (14.6 mm bar axial length)

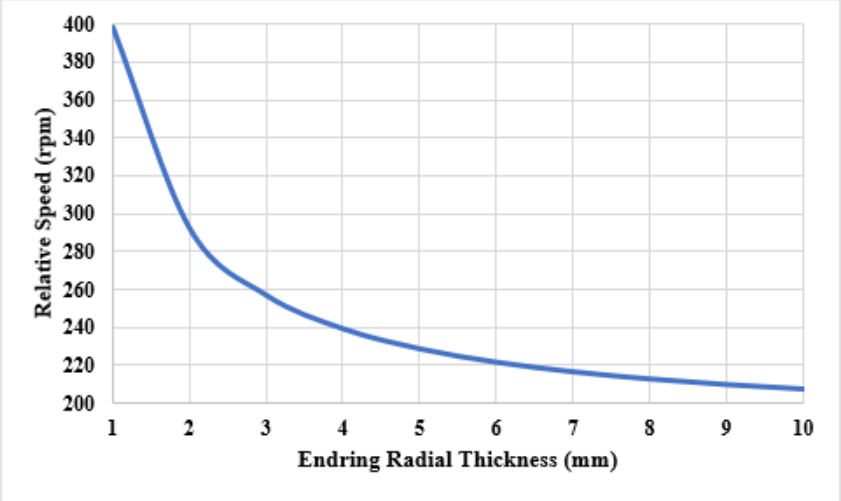

Fig 4. 11 Variation of relative speed corresponding to maximum transmitted torque with endring radial thickness. (14.6 mm bar axial length)

Also, for 22 mm bar axial length, Fig 4.12 and Fig 4.13 show the variations of maximum torque transmitted and corresponding relative speed with endring radial thickness.

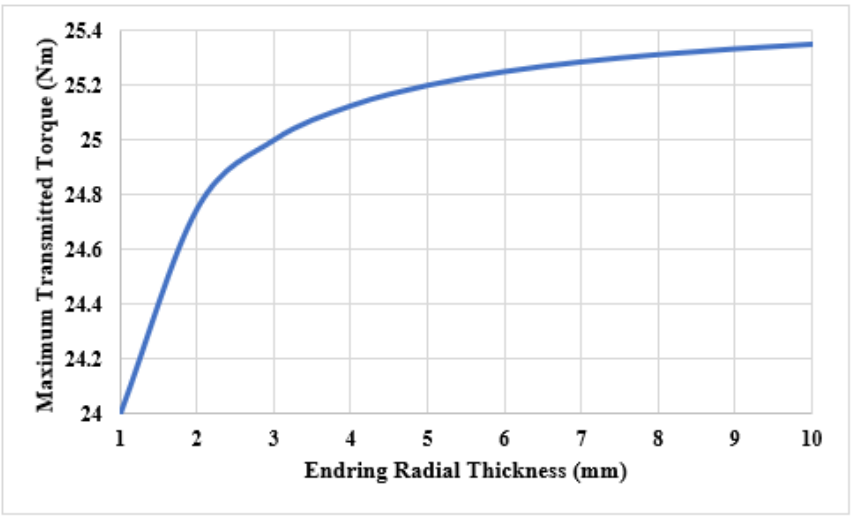

Fig 4. 12 Variation of maximum transmitted torque with endring radial thickness. (22 mm bar axial length)

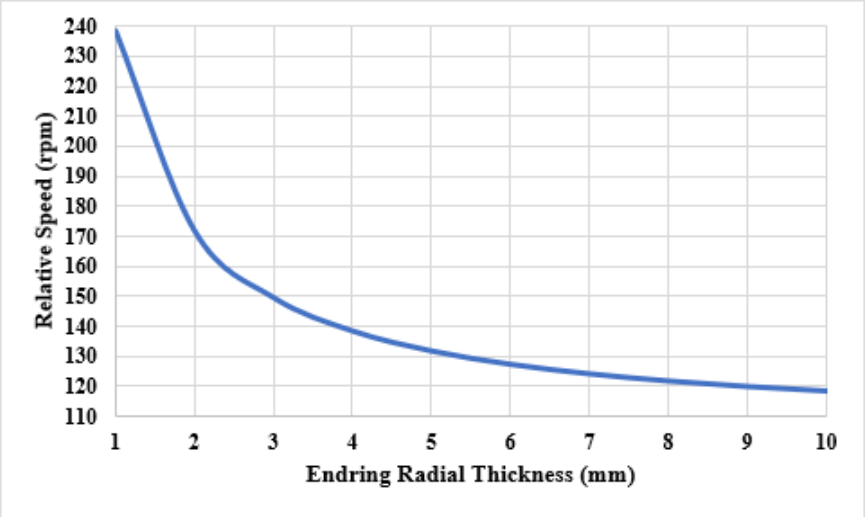

Fig 4. 13 Variation of relative speed corresponding to maximum transmitted torque with endring radial thickness. (22 mm bar axial length)

4.2.2 PMECCs with conductive sheet rotor

This section investigates the performance of an axial single sided PMECCs with a conductive sheet rotor. 3-dimensional finite element analysis is employed to investigate the torque transmission performance of the coupling. Fig 4.14 shows a schematic permanent magnets eddy current coupling equipped with a conductive sheet rotor, and Table 4.3 shows the parameters of PMECCs, respectively.

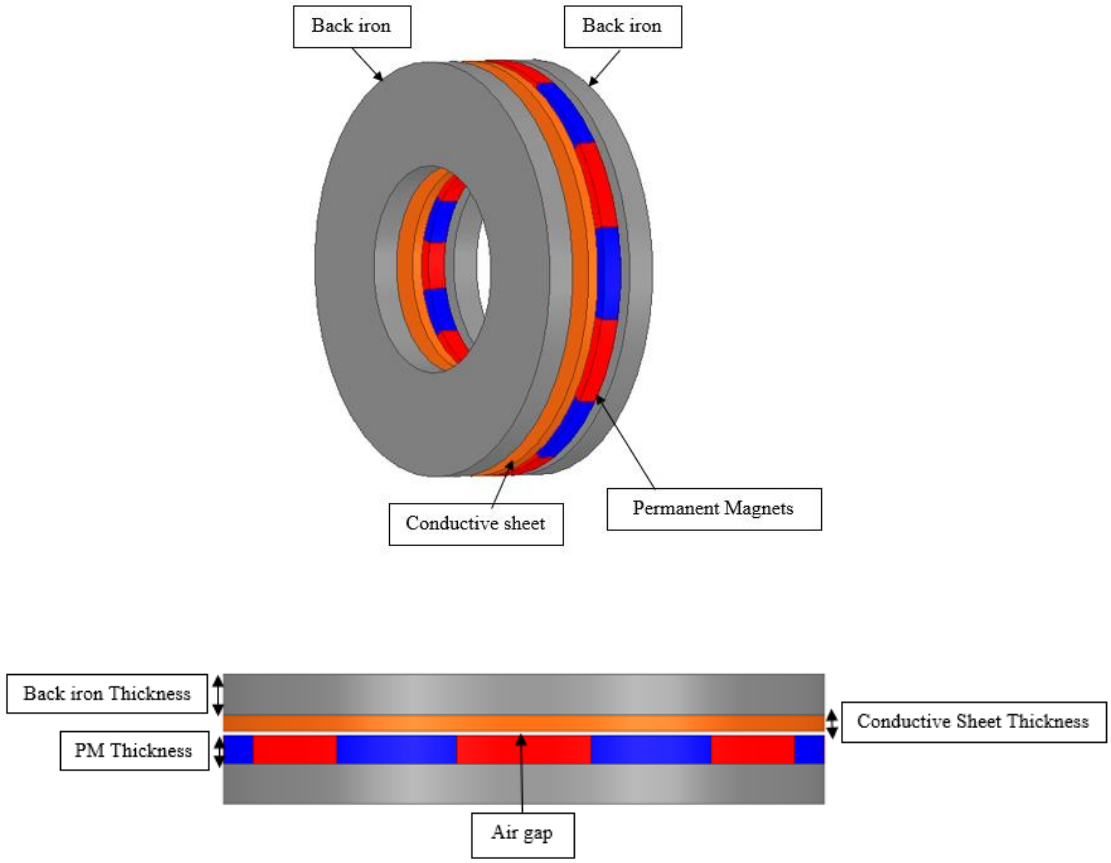

Fig 4. 14 Axial single sided PMECCs with a conductive ring rotor

Table 4. 3 Parameters of conductive ring rotor PMECCs.

Parameter name	Value/ type
Active diameter	150 mm
Air gap length	1 mm
Number of poles	14
Conductive sheet thickness	4-8 mm
Permanent magnets	NdFeB 30
Conductive sheet material	Copper / Aluminium

4.2.2.1 Copper conductive sheet

Fig 4.15 shows the variation of the transmitted torque with the thickness of permanent magnets, when conductive rotor thickness is kept at 4 mm. Moreover, for a magnet thickness of 7mm, Fig 4.16 shows the variation of the relative speed corresponding to the maximum transmitted torque with the thickness of the conductive sheet, and Fig 4.17 shows the variation of transmitted torque for different copper conductive sheet thicknesses. It can be seen that similar to radial-field topologies, employing a conductive sheet, results in signficantly larger relative speeds corresponding to the maximum transmitted torques. This is not desirable for torque transmission applications.

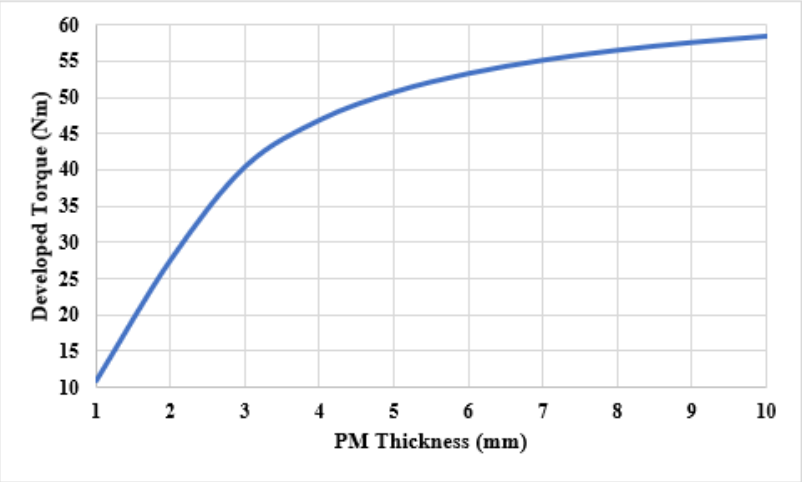

Fig 4. 15 Variation of maximum transmitted torque with thickness of PM. (4 mm conductive sheet thickness)

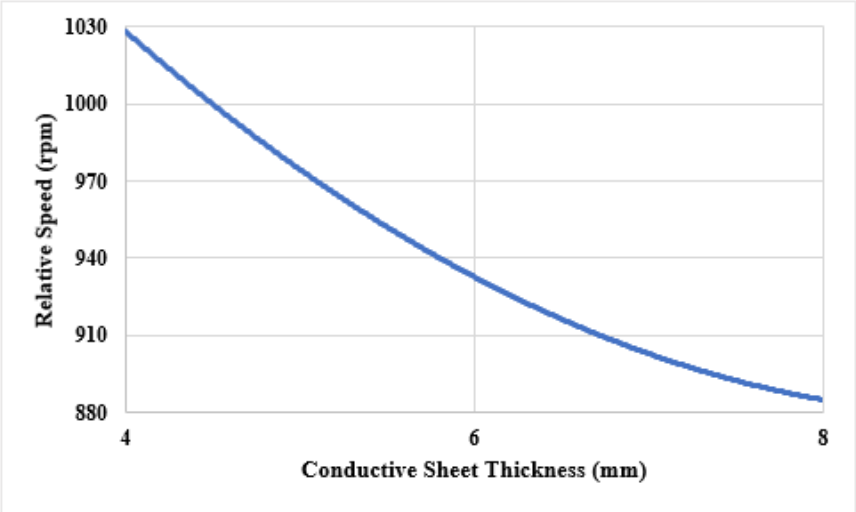

Fig 4. 16 Variation of relative speed corresponding to the maximum transmitted torque with the thickness of conductive sheet.

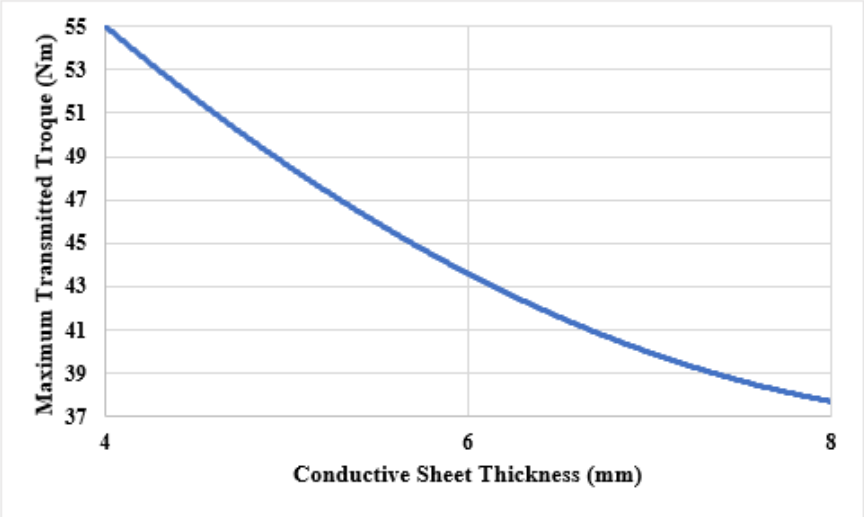

Fig 4. 17 Variation of maximum torque transmitted with different copper conductive sheet thickness. (6mm copper conductive sheet $G_f = 156\ (\frac{\text{Nm}}{\text{rpm}})/\text{m}^3$

(η ~ 91.9% over an NEDC)

4.2.2.2 Aluminum conductive sheet

Fig 4.18 shows the variation of the relative speed corresponding to the maximum transmitted torque with the thickness of the conductive sheet and Fig 4.19 shows the variation of maximum transmitted torque with conductive sheet thickness. It can be

seen that both maximum transmitted torque and corresponding relative speed are decreased with increased sheet thickness.

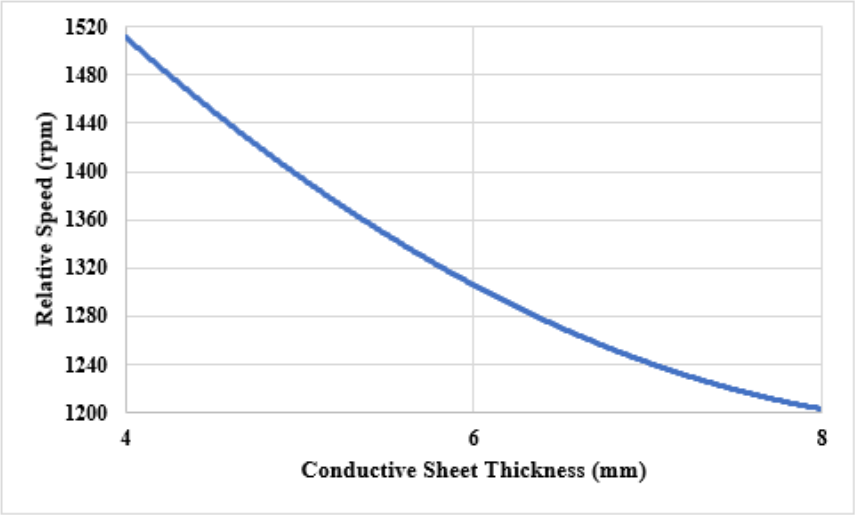

Fig 4. 18 Variation of relative speed corresponding to the maximum transmitted torque with the thickness of conductive sheet.

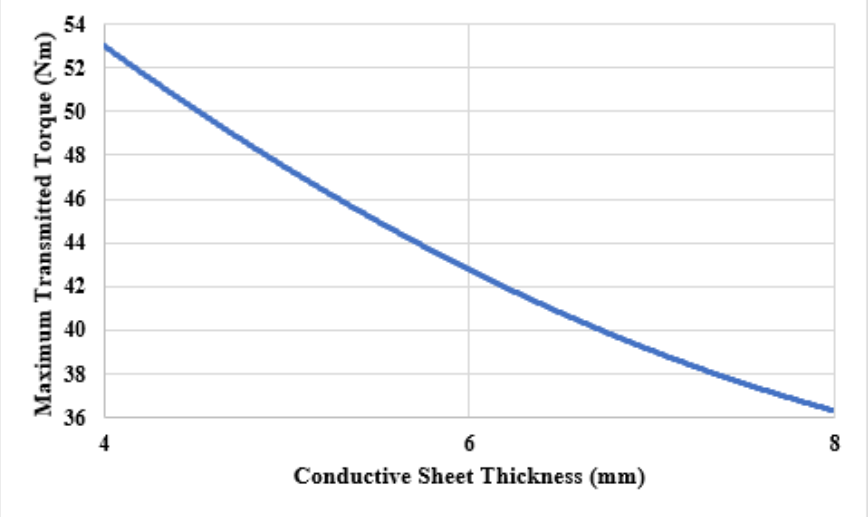

Fig 4. 19 Variation of maximum transmitted torque with different aluminium conductive sheet thickness. (6mm aluminium conductive sheet $G_f =$ $111\ (\frac{\mathrm{Nm}}{\mathrm{rpm}})/\mathrm{m}^3$ ($\eta \sim$ 88.9% over an NEDC)

4.3 Double sided permanent magnet eddy current coupling

4.3.1 PMECCs with Squirrel cage rotor type

This section investigates the performance of an axial double sided PMECCs with a squirrel cage rotor. Fig 4.20 shows an axial double-sided permanent magnet eddy current coupling equipped with squirrel cage rotor, and Table 4.4 gives the geometric parameters of the PMECCs.

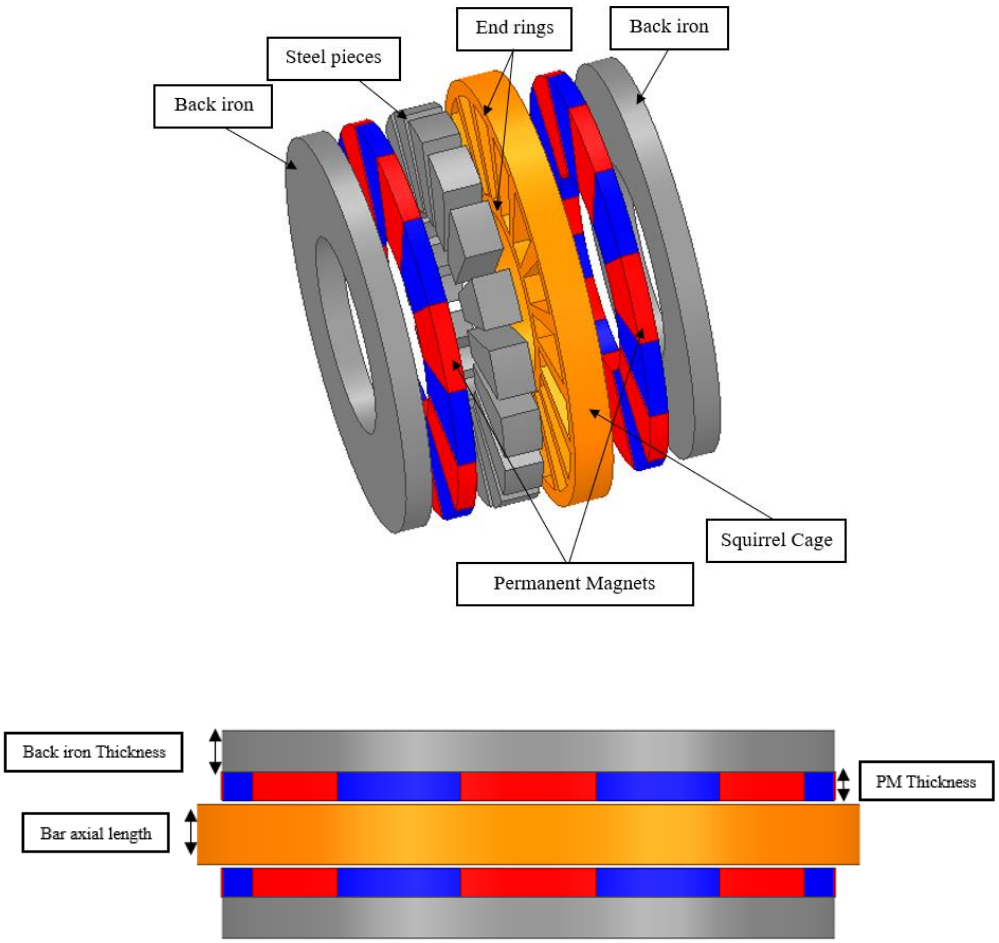

Fig 4. 20 Axial double-sided PMECCs with squirrel cage.

Table 4. 4 Parameters of an Axial double-Sided Parameters of squirrel cage PMECCs.

Parameter name	Value/ type
Active diameter	150 mm
Air gap length	1mm
Number of poles	14
Number of bars	17
Permanent magnets	NdFeB
Squirrel cage material	Copper / Aluminium
Squirrel cage axial length	14.6 / 22 mm

4.3.1.1 Copper squirrel cage

Fig 4.21 shows the variation of maximum transmitted with the thickness of permanent magnets. Clearly, and as would be expected, it can be seen that the transmitted torque is improved by increasing the permanent magnet thickness, albeit with diminishing returns when the PM thickness is increased further. However, it can also be seen that an optimum magnet thickness for which a transmitted torque is maximum exists. Furthermore, with a selected PM and endring radial thickness of 7mm and 6mm respectively, Fig 4.22 shows the variation of transmitted torque with relative speed for bar axial length of 14.6 mm. It can be seen for this coupling the maximum transmitted torque is significantly larger than that of the single sided counterpart, however, this occurs at a much larger relative speed, $\alpha \approx 350$ rpm. In addition, Fig 4.23 shows the variation of the transmitted torque with relative speed when the bars axial length is increased to 22 mm, It can be seen that this results in a significant reduction in the relative speed, $\alpha \approx 224$ rpm.

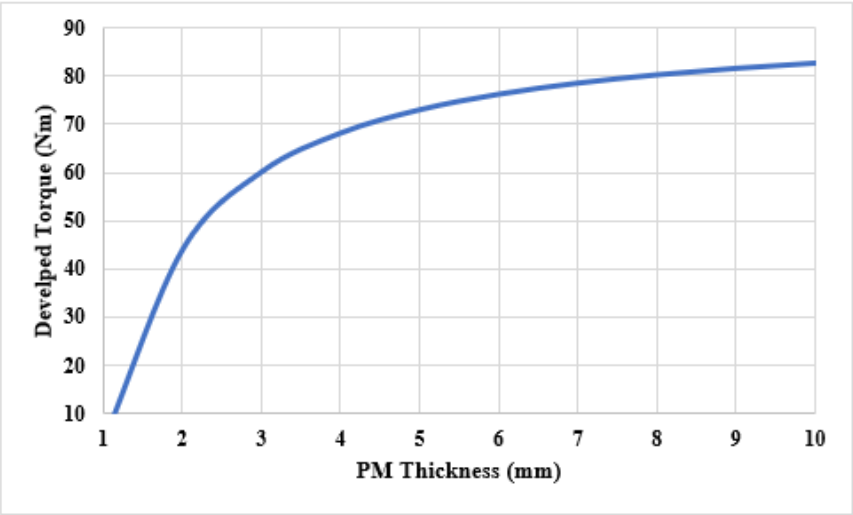

Fig 4. 21 Variation of maximum transmitted torque with thickness of PM.

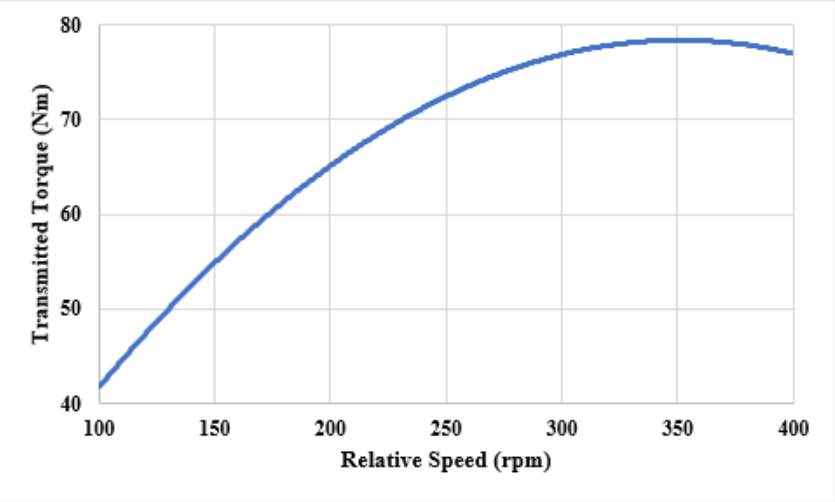

Fig 4. 22 Variation of transmitted torque with relative speed (14.6 mm of bar axial length) $G_f = 498\ (\frac{\text{Nm}}{\text{rpm}})/\text{m}^3$ (η ~ 98.3% over an NEDC)

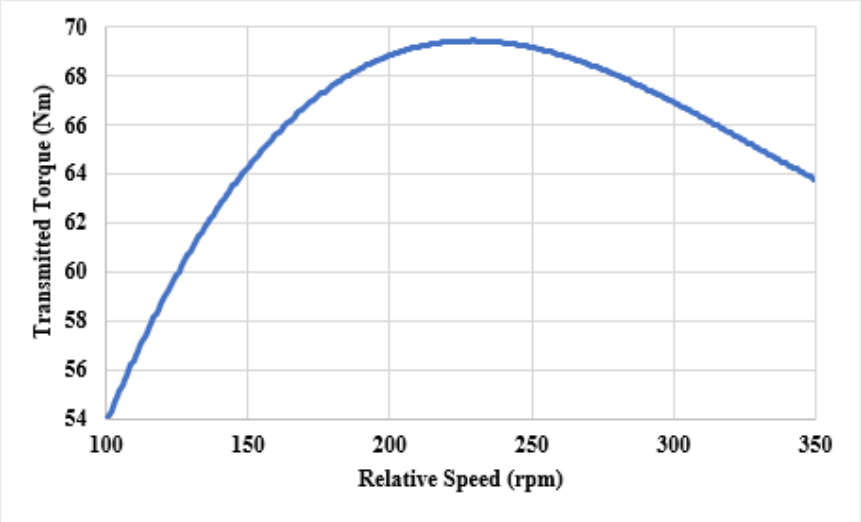

Fig 4. 23 Variation of transmitted torque with relative speed (22 mm of bar axial length) $G_f = 601\ (\frac{\text{Nm}}{\text{rpm}})/\text{m}^3$ ($\eta \sim 98.7\%$ over an NEDC)

Additionally, Fig 4.24 and Fig 4.25 show the variation of maximum transmitted torque and corresponding relative speeds with endring radial thickness, respectively. It can be seen that endring radial thickness has significant effect on relative speed where the maximum transmitted torque occurs. But has a slight influence on the maximum transmitted torque.

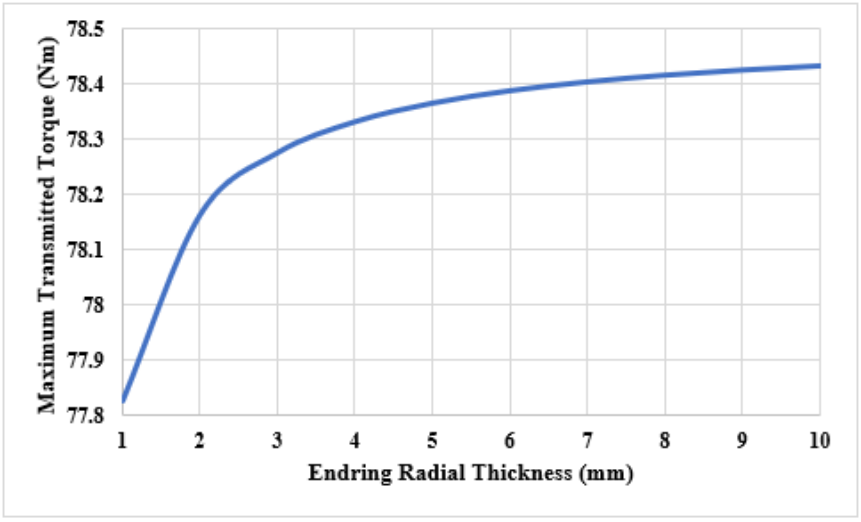

Fig 4. 24 Variation of maximum transmitted torque with endring radial thickness. (14.6 mm bar axial length)

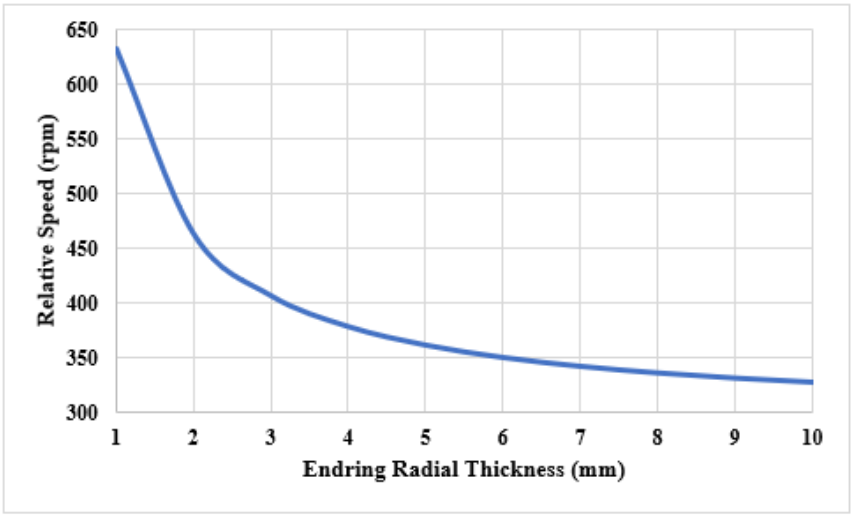

Fig 4. 25 Variation of relative speed corresponding to maximum transmitted torque with endring radial thickness. (14.6 mm bar axial length)

Moreover, for 22 mm bar axial length Fig 4.26 and Fig 4.27 show the maximum torque transmitted and the corresponding relative speed with endring radial thickness. It can be seen that an endring radial thickness exists, beyond which variation in transmitted torque and corresponding relative speed, are negligible.

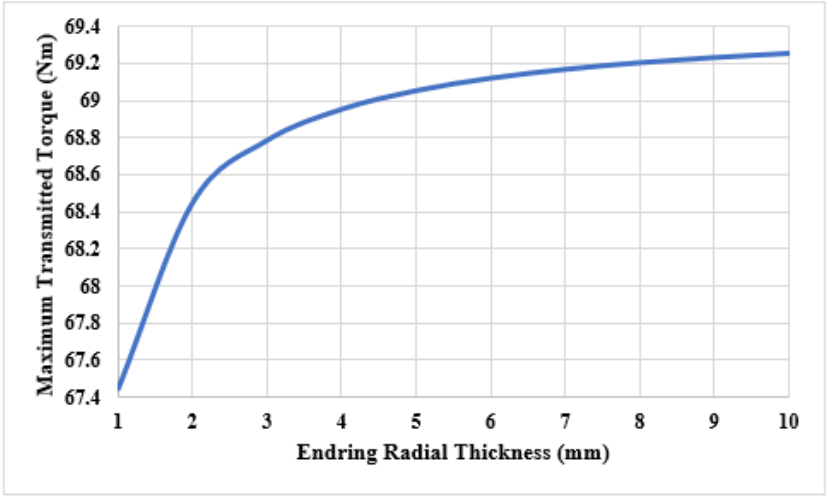

Fig 4. 26 Variation of maximum transmitted torque with endring radial thickness. (22 mm bar axial length)

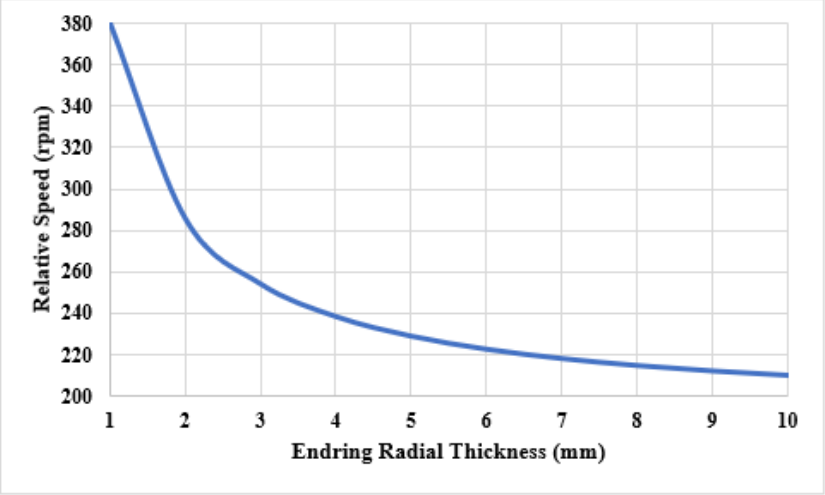

Fig 4. 27 Variation of relative speed corresponding to maximum transmitted torque with endring radial thickness. (22 mm bar axial length)

4.3.1.2 Aluminium squirrel cage

Comparably, with a selected PM and endring radial thickness of 7 mm and 6mm, Fig 4.28 and Fig 4.29 show the variation of transmitted torque with relative speed for bar axial length of 14.6 and 22 mm, respectively. It can be seen that when aluminium is employed, which has a lower electrical conductivity than copper, the relative speed at which the maximum torque occurs is now significantly larger, $\alpha \approx 542$ rpm and $\alpha \approx 318$ rpm, for 14.6 mm and 22 mm bar axial length, respectively. However, the maximum transmitted torque remains fairly constant.

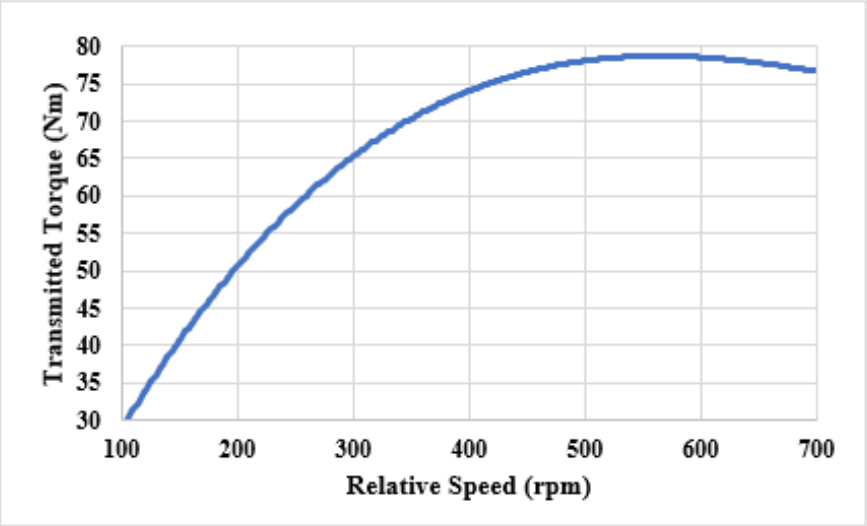

Fig 4. 28 Variation of transmitted torque with relative speed with aluminium material (14.6 mm of bar axial length) $G_f = 326\ (\frac{\text{Nm}}{\text{rpm}})/\text{m}^3$ ($\eta \sim 97.4\%$ over an NEDC)

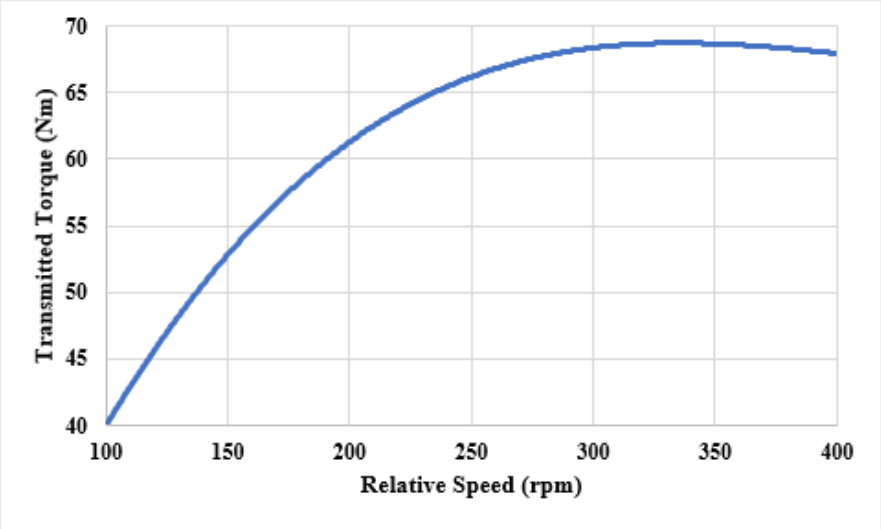

Fig 4. 29 Variation of transmitted torque with relative speed with aluminium material (22 mm of bar axial length) $G_f = 417\ (\frac{\text{Nm}}{\text{rpm}})/\text{m}^3$ ($\eta \sim 98.2\%$ over an NEDC)

Moreover, Fig. 4.30 and Fig. 4.31 show the variation of maximum transmitted torque and corresponding relative speed with endring radial thickness for bar axial length

of 14.6 mm. It can be seen that endring length has a major effect on relative speed nevertheless, it has a minor influence on the maximum torque transmitted.

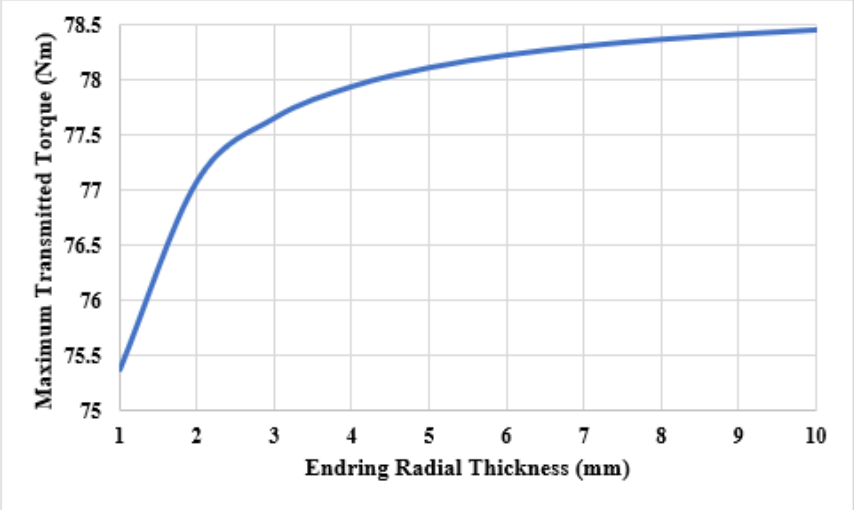

Fig 4. 30 Variation of maximum transmitted torque with endring radial thickness. (14.6 mm bar axial length)

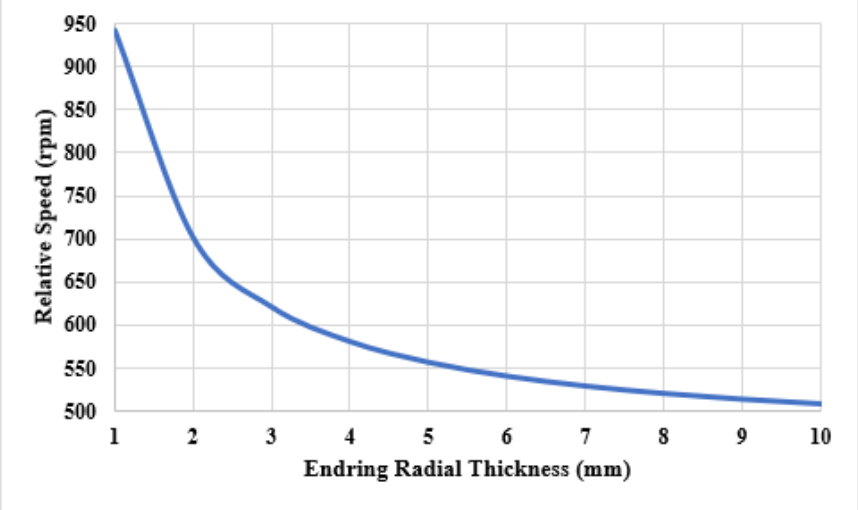

Fig 4. 31 Variation of relative speed corresponding to maximum transmitted torque with endring radial thickness. (14.6 mm bar axial length)

Likewise, Fig 4.32 and Fig 4.33 show the variation of maximum transmitted torque and corresponding relative speed with endring radial thickness for a bar axial length

of 22 mm. Similarly, to 14.6 mm endring radial thickness has a significant effect on the relative speed corresopnding to maximum transmitted torque.

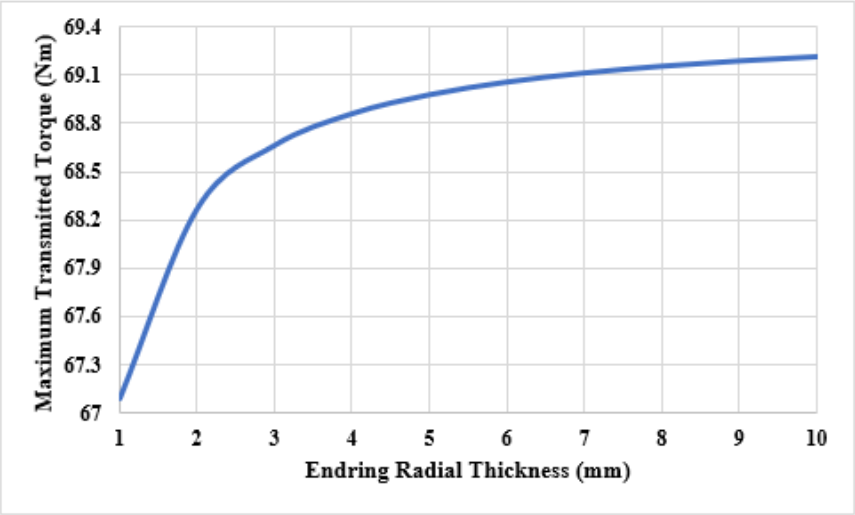

Fig 4. 32 Variation of maximum transmitted torque with endring radial thickness. (22 mm bar axial length)

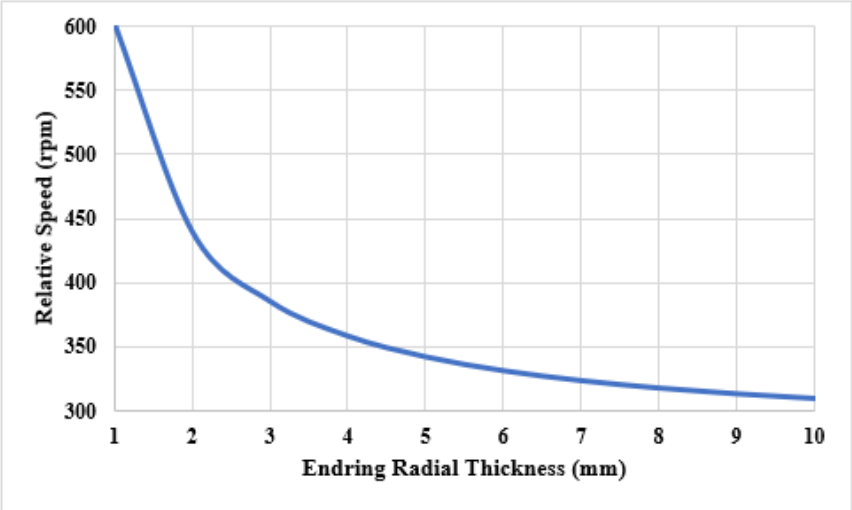

Fig 4. 33 Variation of relative speed corresponding to maximum transmitted torque with endring radial thickness. (22 mm bar axial length)

4.3.2 PMECCs with conductive sheet

This section investigates the performance of axial double sided PMECCs with a conductive sheet rotor. 3-dimensional finite element analysis is completed to

examine the developed torque of this coupling along with increasing the thickness of permanent magnets. As well, it studies the effect of the thickness of the conductive sheet on relative speed. Fig 4.34 and Table 4.5 show the geometric details and the parameters of the PMECCs, respectively.

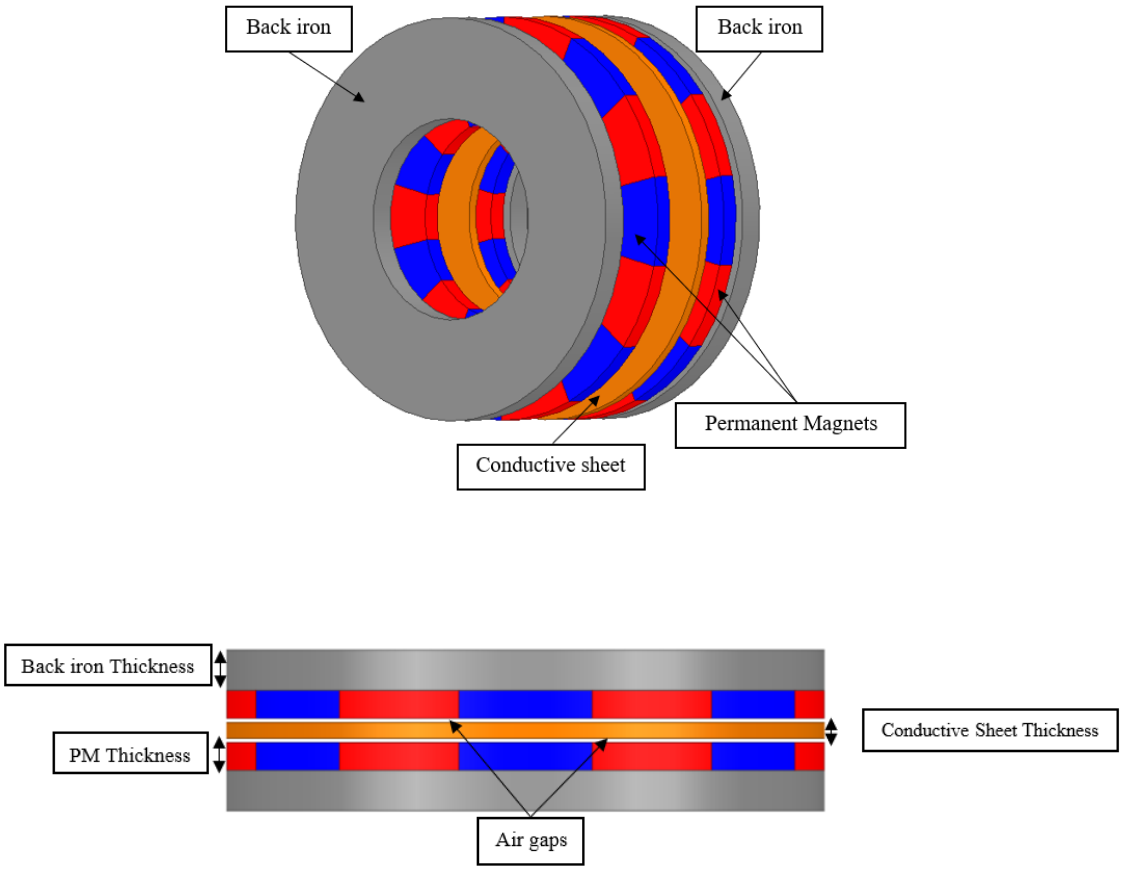

Fig 4. 34 Axial double-sided permanent magnet eddy current coupling with a conductive ring rotor

Table 4. 5 Parameters of axial double sided PMECCs with conductive sheet rotor.

Parameter name	Value/ type
Active diameter	150 mm
Air gap length	1 mm
Number of poles	14
Conductive sheet thickness	4-8 mm
Permanent magnets	NdFeB 30
Conductive sheet material	Copper / Aluminium

4.3.2.1 Copper conductive sheet

Fig 4.35 shows the variation of maximum transmitted torque with increased thickness of permanent magnets, when conductive rotor thickness is kept at 4 mm. For a 7 mm thickness, Fig 4.36 shows the effect of the thickness of conductive sheet on relative speed. Furthermore, Fig 4.37 shows the variation of maximum transmitted torque with conductive sheet thickness.

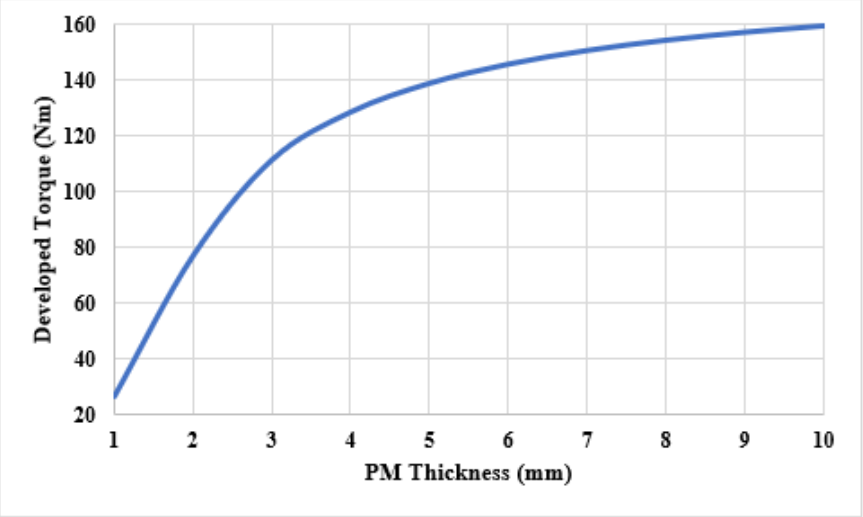

Fig 4. 35 Variation of maximum transmitted torque with thickness of PM

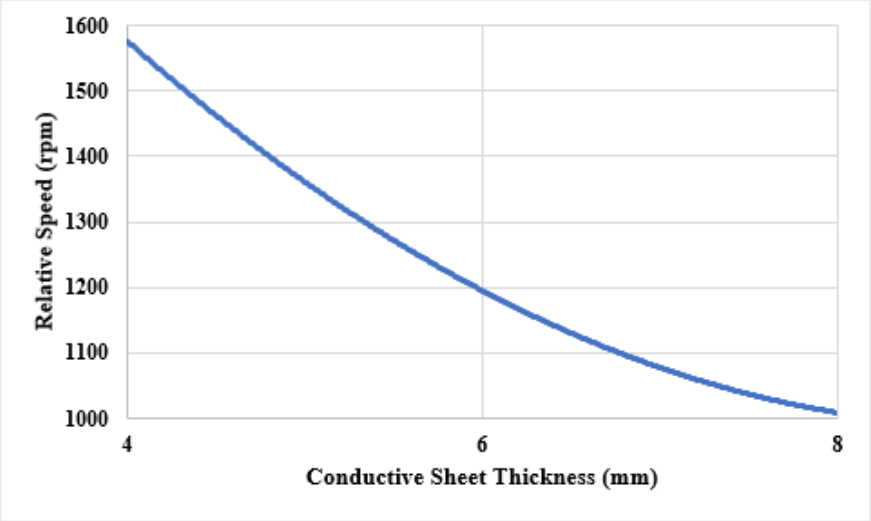

Fig 4. 36 Variation of relative speed corresponding to the maximum transmitted torque with the thickness of conductive sheet.

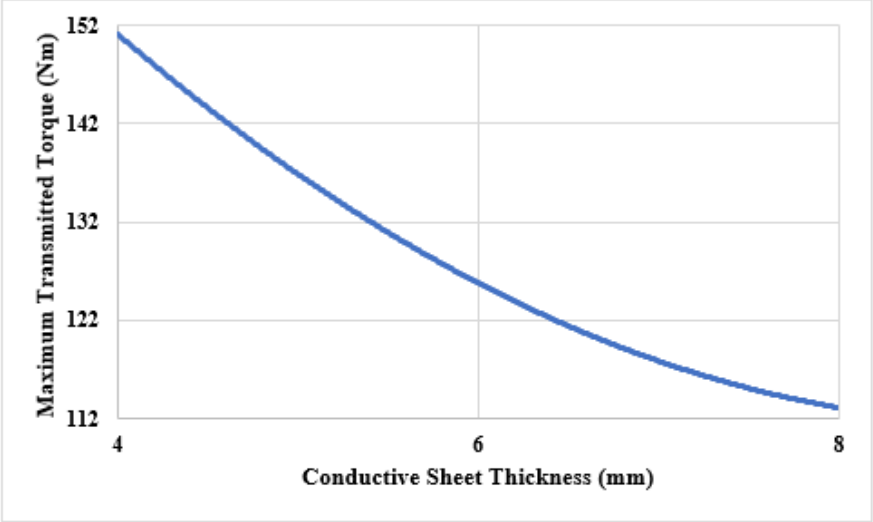

Fig 4. 37 Variation of maximum transmitted torque with different copper conductive sheet thickness. (6mm copper conductive sheet $G_f = 281\ (\frac{\text{Nm}}{\text{rpm}})/\text{m}^3$

(η ~ 96.4% over an NEDC)

4.3.2.2 Aluminium conductive sheet

Likewise, Fig 4.38 shows the variation of relative speed corresponding to the maximum transmitted torque with the thickness of aluminum conductive sheet, and Fig 4.39 shows the variation of maximum transmitted torque, with different

conductive sheet thickness. It can be seen that, similarly to copper, increasing the thickness of the conductive sheet results in reduced maximum transmitted torque and corresponding relative speed.

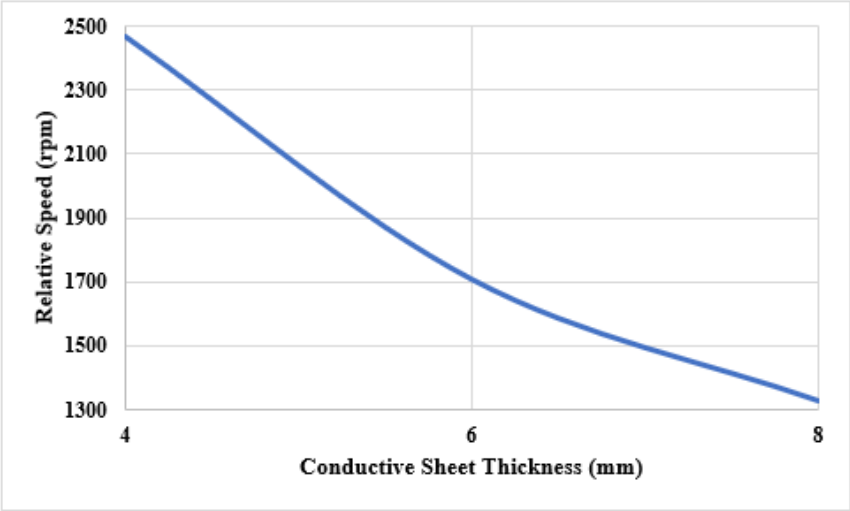

Fig 4. 38 Variation of relative speed corresponding to the maximum transmitted torque with the thickness of aluminium conductive sheet.

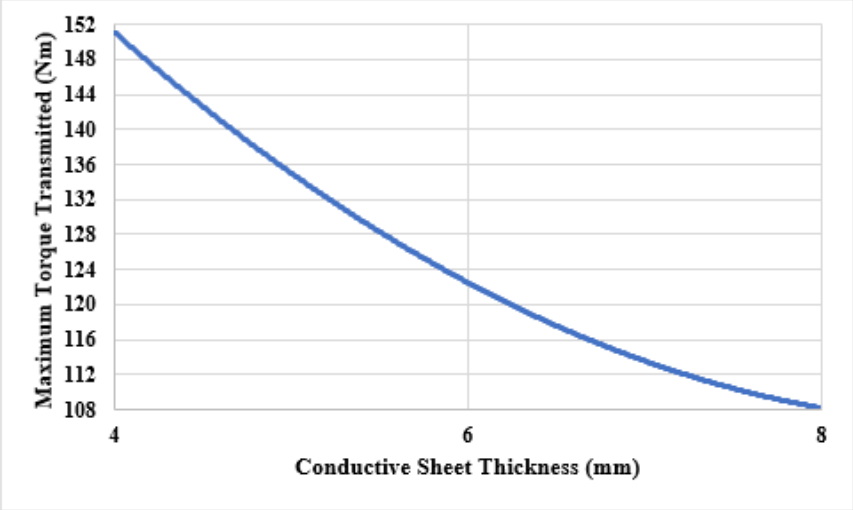

Fig 4. 39 Variation of maximum transmitted torque with different aluminium conductive sheet thickness. (6mm copper aluminium sheet $G_f = 192\ (\frac{\text{Nm}}{\text{rpm}})/\text{m}^3$)

($\eta \sim$ 79.8% over an NEDC)

4.4 Discussion

It can be observed that different PMECCs designs have distinctive torque and speed characteristics. However, as previously explained PMECCs' efficiency is mainly affected by input speed and relative speed and either the higher input speed or smaller relative speed the higher the efficiency. Furthermore, Table 4.6 shows a comparison between all different axial field designs' parameters and efficiency.

Table 4. 6 comparison between all different axial field designs' parameters and efficiency.

Type of conductive rotor	Volume (litre)	Poles/slot	Slot/sheet depth (mm)	Sided	Material	G_f	α (rpm)	T_m (Nm)	η %
Squirrel cage	0.753	14/17	14.6	SS	Cu	605	136	31	98.2
Squirrel cage	0.883	14/17	22	SS	Cu	713	80	25.2	98.8
Squirrel cage	0.753	14/17	14.6	SS	Alu	370	224	31.2	97.1
Squirrel cage	0.883	14/17	22	SS	Alu	469	122	25.3	97.9
Sheet	0.060	14	6	SS	Cu	156	927	43.5	91.9
Sheet	0.060	14	6	SS	Alu	111	1305	43.7	88.9
Squirrel cage	0.984	14/17	14.6	DS	Cu	498	350	78	98.3
Squirrel cage	10.24	14/17	22	DS	Cu	601	224	69	98.7
Squirrel cage	0.984	14/17	14.6	DS	Alu	326	542	79	97.4
Squirrel cage	10.24	14/17	22	DS	Alu	417	318	68	98.2
Sheet	0.742	14	6	DS	Cu	281	1195	125	96.4
Sheet	0.742	14	6	DS	Alu	192	1705	122	79.8

Similarly, to radial field PMECCs, employing squirrel cage rotor type improves the torque density of the coupling and strengthen the magnetic field in the air gap. Furthermore, as it can be seen in Table 4.6 for the single sided squirrel cage PMECCs with 14/17 pole/slot combination and comparing between 14.6mm /22mm slot depth, efficiency has been improved , and this is due to reduction in the total impedance of the squirrel cage and increase in the out power. Furthermore, in order to meet the

requirement of energy efficiency of the couplings over the NEDC cycle, for example, with the studied vehicle, the coulping should be able to transmit a minimum of 40 Nm and at low slip speed. Therefore, the selection of the coupling depends on the one which best meets these conditions. For instance, within the limits of the provided active diameter, the simulation result indicate that an axial single sided PMECCs equipped with squirrel cage rotor and bar axial length of 22 mm can transmit a maximum torque of 25.27 Nm and occurs at low correspoding relative speed $\alpha \approx 80$ rpm, suggesting an excellent energy efficiency. However it does not meet the peak torque requirement of the coupling. Therefore, in the following a comparison between axial single and double sided permanent magnet eddy current couplings with copper material is presented. Fig 4.40 shows the variation of transmitted torque with relative speed of single sided PMECCs with copper material and bars axial length of 22 mm. It can be seen that a torque of 24.9 Nm is transmitted at $\alpha \approx 100$. Furthermore, Fig 4.41 shows the variation of transmitted torque with relative speed of double sided PMECCs with copper material and bars axial length of 22 mm and can be observed that a torque of 54 Nm is transmitted at relative speed $\alpha \approx 100$.

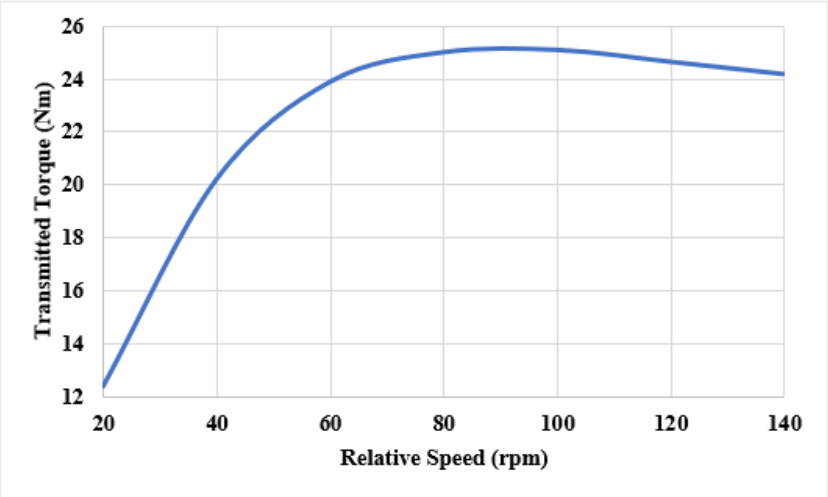

Fig 4. 40 Variation of transmitted torque with relative speed. (axial single sided)
$G_f = 713\ (\frac{\text{Nm}}{\text{rpm}})/\text{m}^3$ (η ~ 98.8% over an NEDC)

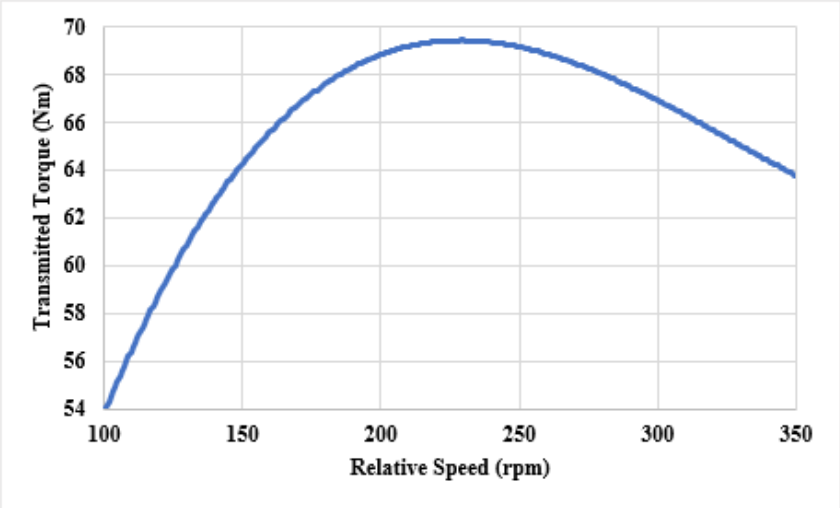

Fig 4. 41 Variation of transmitted torque with relative speed. (axial double sided)
$G_f = 601\ (\frac{\text{Nm}}{\text{rpm}})/\text{m}^3$ (η ~ 98.7% over an NEDC)

Moreover, Fig 4.42 and Fig 4.43 show the variation of transmitted torque with relative speed of a radial single and double sided PMECCs with copper material. It can be seen that for a single sided coupling a torque of 39.6 Nm is transmitted at $\alpha \approx$ 100 rpm.

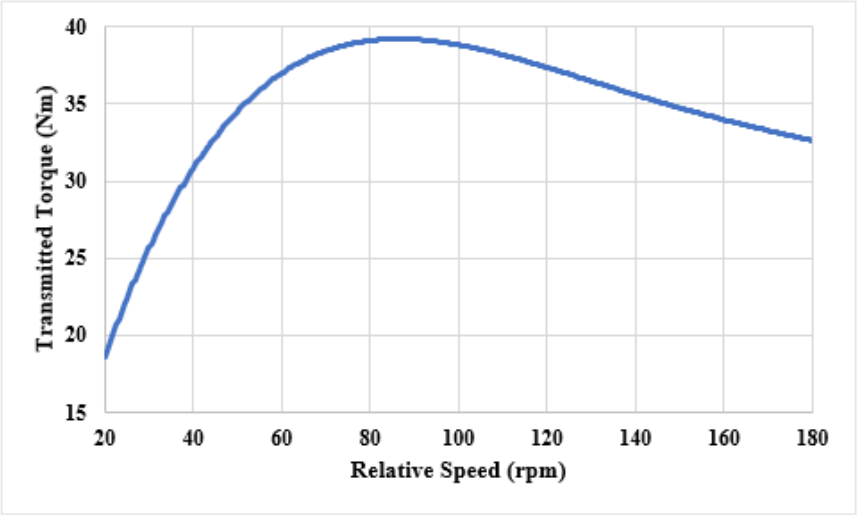

Fig 4. 42 Variation of transmitted torque with relative speed. (radial single sided- 15mm slot depth)) $G_f = 980$ $(\frac{\text{Nm}}{\text{rpm}})/\text{m}^3$ ($\eta \sim$ 99.1% over an NEDC)

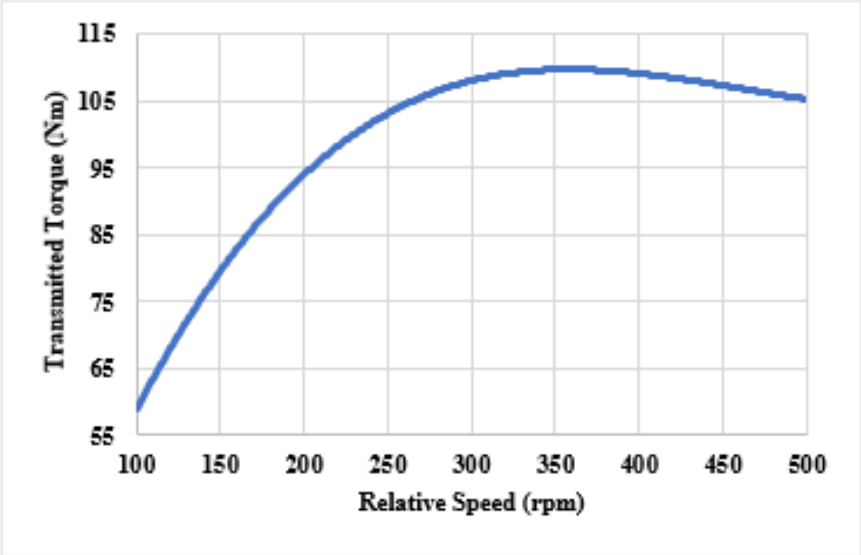

Fig 4. 43 Variation of transmitted torque with relative speed. (radial double sided - 13.4mm slot depth)) $G_f = 691$ $(\frac{\text{Nm}}{\text{rpm}})/\text{m}^3$ ($\eta \sim$ 98.6% over an NEDC)

Based on the the previous findings, and considering the values of the goodness factor, it is clear that for the vehicle, application for example, it can be concluded that a single sided PMECCs for both axial and radial topologies would be the better option.

4.4.1 Conclusion

In this chapter simulation and analysis of different topologies, structures and conductive material types of an axial permanent magnet eddy current coupling are presented. Based on the finite element analysis, the torque and speed characteristics of the PMECCs are predicted. It can be observed that PMECCs with Copper and Aluminium material produce a similar maximum trasmitted torque, however, with aluminum material maximum transmitted torque occurs at a higher corresponding relative speed due to the lower conductivity. It has also been shown, and similar to radial topologies, the end ring length of squirrel cage PMECCs has a significant effect on the relative speed corresponding to the maximum torque, but it has a practically negligible impact on the maximum transmitted torque. Furthermore, increasing the thickness of conductive sheet for both copper and aluminium material results in reduction of maximum transmitted torque, due to the increased effective airgap and reduced PM field.

Chapter 5

Squirrel cage end ring's influence on PMECCs

5.1 Introduction

In this chapter a comparison between 2D and 3D modelling of Single- and double-sided squirrel cage permanent magnet eddy current couplings using finite element analysis FEA is undertaken. This primarily focuses on the modelling and representation of the end rings impedance in the circuit coupled 2D finite element analysis. Although the calculation of resistance of the end-rings is straightforward, the inductance is more complicated. Nevertheless, the ability to design and predict the performance of PMECCs using 2D finite element is very useful and saves a significant amount of time, and can be used for the initial dimensioning and parametric studies before, one or more designs are selected for further analysis.

5.2 Single sided PMECCs with Squirrel cage rotor

This section studies single sided squirrel cage PMECCs. Figure 5.1 shows a cross-section of a single sided PMECC equipped with a squirrel cage rotor. It consists of an outer rotor that includes permanent magnets and a back iron, and an inner rotor which includes a squirrel cage made from a conductive material backed by an iron material. Fig 5.2 shows 2D and 3D view of the PMECCs.

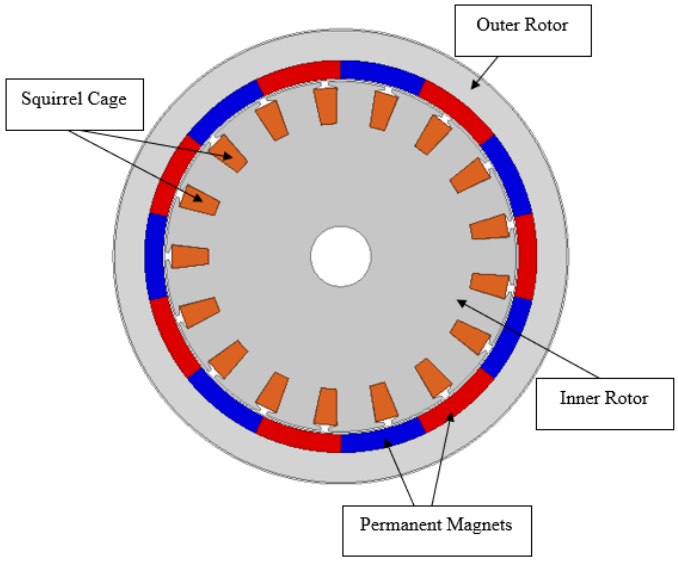

Fig 5. 1 Cross section of single sided of PMECCs

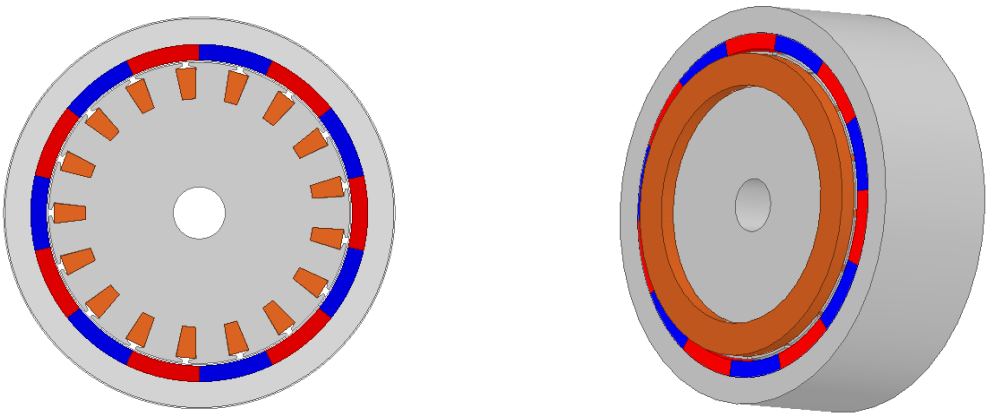

(ii) 2D (ii) 3D

Fig 5. 2 PMECCs equipped with squirrel cage rotor

A main component of this PMECCs is its rotor, which is cylindrically shaped with conductive bars short circuited at each end making a close loop. When currents are induced in the bars during rotation, the end rings form a return path. Fig 5.3 shows a 3D view of squirrel cage.

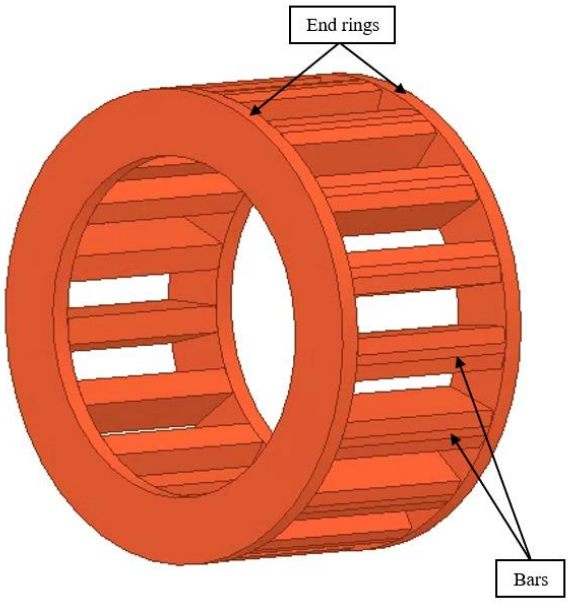

Fig 5. 3 Squirrel cage (3D view)

Consequently, the impedance of cage rotor includes the resistances and inductances of the bars and the endrings [41]. In 3D modelling, the impedances of the bars and endrings are parts of the finite element analysis, and there is no need for external circuit connections. However, in the 2D analysis, although the impedances of the bars are considered in the finite element analysis, the end-rings are not considered. Therefore, incorporation of an external circuit representing the end-rings is required, and in this study the focus will only be on the end ring impedance calculation. Figure 5.4 shows the external circuits which were employed to represent the squirrel cage rotor, with one considers the end ring impedance as a resistance and an inductance and the other one neglects the inductance. Furthermore, Fig 5.5 shows a 3D view of an end ring.

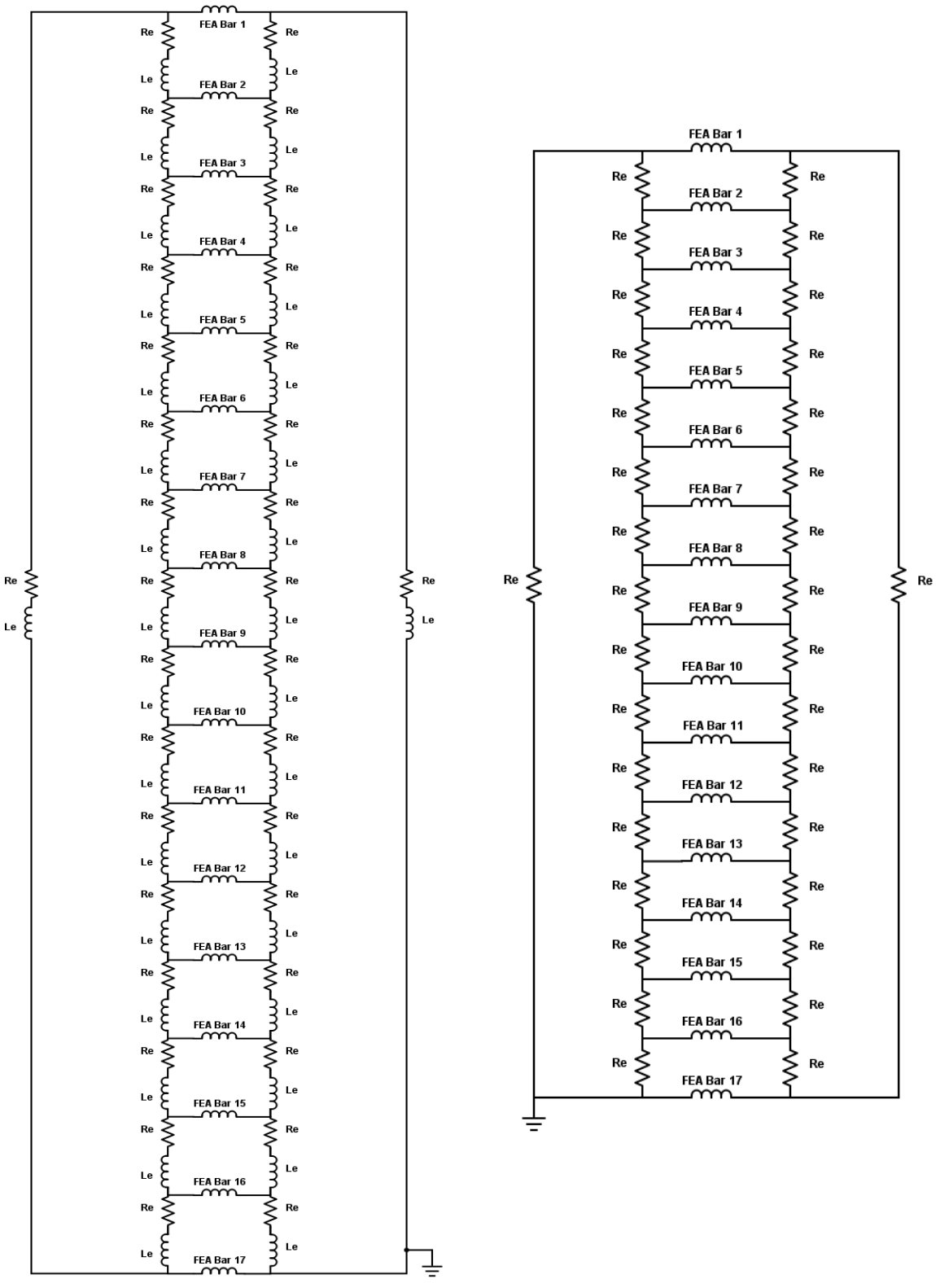

Fig 5. 4 External circuits representing the cage rotor (i) end ring consist of resistance and inductance (ii) end ring consist of resistance.

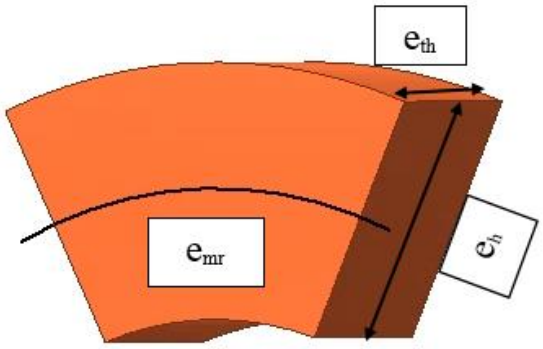

Fig 5. 5 end ring (3D view)

Impedance of the end ring can add a considerable amount to the total impedance of the rotor and may affect the PMECCs performance [42]. Nevertheless, the inductance of an end ring is sometimes ignored and only a simple resistance is used instead to represent the total impedance of the rotor [41]. Therefore, and in the following in order to examine the influence of end-ring's impedance on the PMECCs performance, the calculation of end ring impedance is completed and a comparison between 2D results and 3D predictions are presented. In order to calculate the resistance and inductance of an end ring, two equations are used, and for the reason of simplicity the end ring cross section is assumed to be square and equals to the bar cross section area. Therefore, the end-ring resistance is given by:

$$Re = \rho * l/A \tag{5.1}$$

Moreover, the end ring inductance can be found by applying Trickey's equation and the inductance of one segment of an end ring can be calculated as [43]:

$$Le = \pi \left(\frac{\mu 0}{Nr}\right) (e_{mr} \lambda e) \quad (5.2)$$

Where

$$\lambda e = 0.365 \log(3\pi \frac{e_{mr}}{4 (e_h + e_{th})}) \quad (5.3)$$

5.2.1 Squirrel cage rotor with 17 bars

This section concentrates on single sided squirrel cage PMECCs rotor with 17 bars. A 2D finite element design is completed and an external circuit is modelled and added to the simulation to study the influence of an end ring on the PMECCs performance with different slot depth and conductive material and compared to a 3-dimensional solution result. Figure 5.6 shows a single sided PMECCs cage rotor with 17 bars. Table 5.1 shows the parameters of the studied end ring.

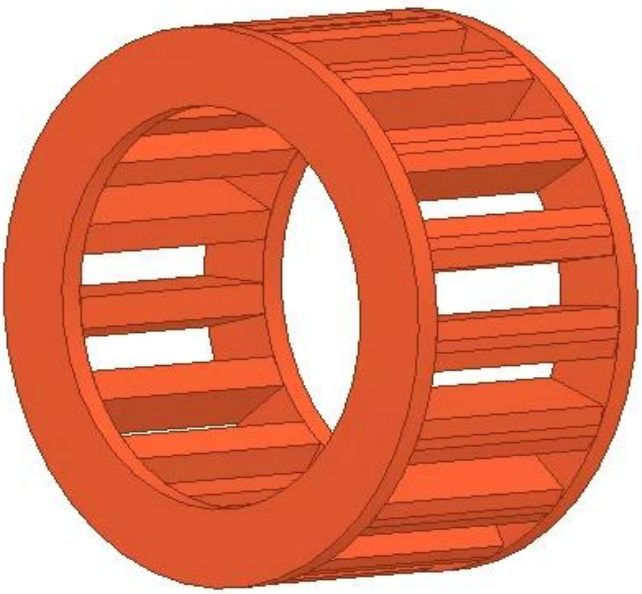

Fig 5. 6 Single sided PMECCs cage rotor with 17 bars

Furthermore, Figure 5.7 shows the variation of transmitted torque with relative speed using 2D and 3D finite element for a copper squirrel cage. Figure 5.8 shows the variation of transmitted torque with relative speed of the same PMECCs, however the squirrel cage rotor material is now changed to aluminium. It can be seen that the 2D predictions for both copper and aluminium squirrel cage rotors are slightly higher than 3D predictions, whilst adding the inductance to the end-ring impedance has an insignificant effect on the predicted 2D torque. This is due to the method adopted to calculate the end ring resistance and inductance which mainly consider the geometrical dimensions of the end ring without taking into account of the complexity of the magnetic field distribution around the end ring . Nevertheless, there is agreement between 2D and 3D in the prediction of the relative speed corresponding to the maximum transmitted torque.

Table 5. 1 Single sided PMECC end ring parameters

End ring	Value / type	
Height = slot depth (e_h)	11 mm / 15 mm	
Cross section area (A)	75.8 mm^2 / 131.3 mm^2	
Mean radius (e_{mr})	50 mm / 48.5 mm	
Thickness (e_{th})	5 mm	
Number of bars (Nr)	17	
Conductive material	Cu / Alu	
Material resistivity (ρ)	Cu = 1.7×10^{-8}	Alu = 2.65×10^{-8}

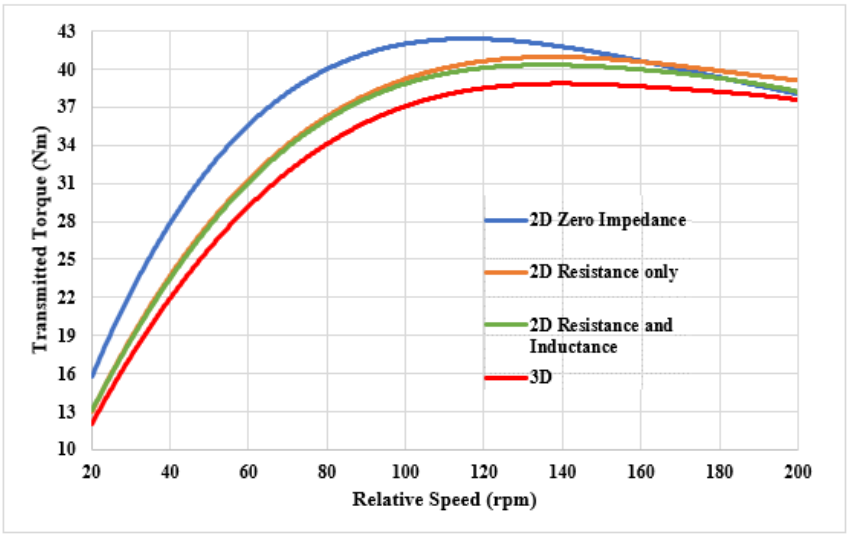

(a) 11 mm slot depth

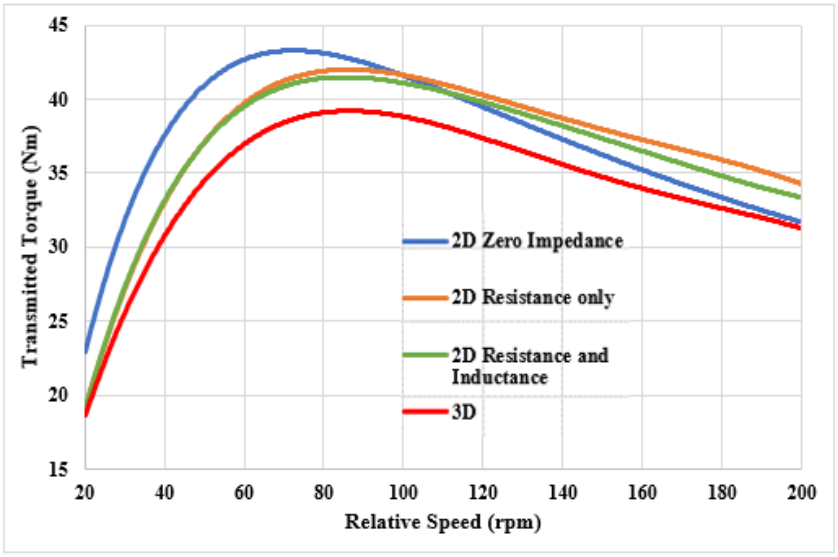

(b) 15 mm slot depth

Fig 5. 7 Variation of transmitted torque with relative speed. (Copper squirrel cage)

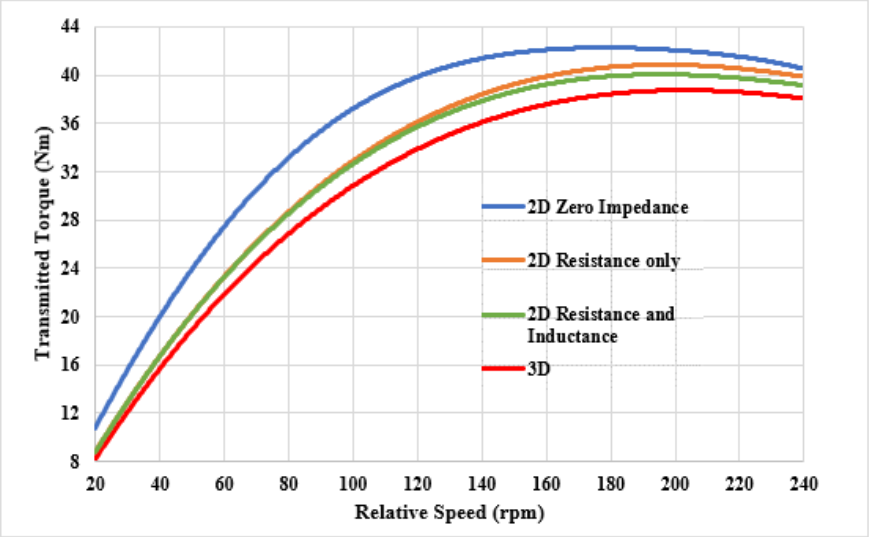

(a) 11 mm slot depth

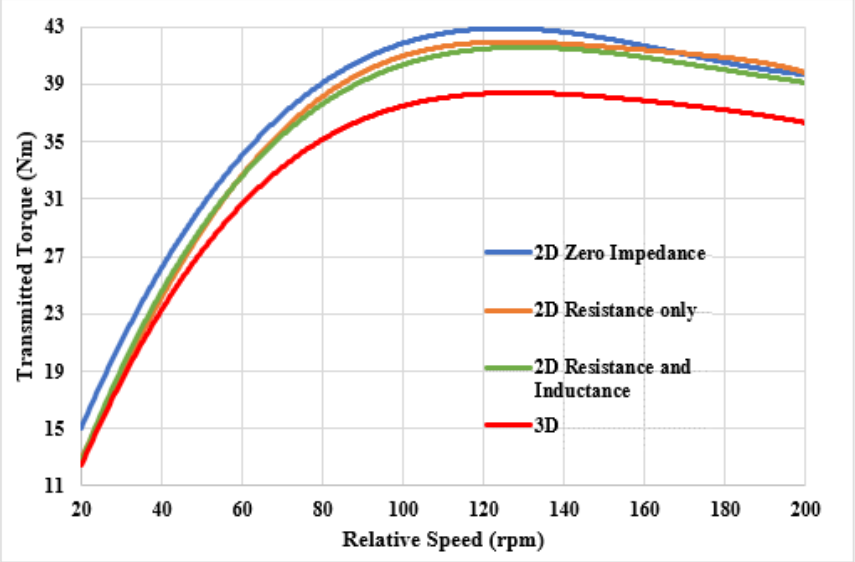

(b) 15 mm slot depth

Fig 5. 8 Variation of transmitted torque with relative speed. (Aluminium squirrel cage)

5.3 Double sided PMECCs with Squirrel cage rotor

5.3.1 Squirrel cage rotor with 17 bars

This part of this chapter studies double sided squirrel cage PMECCs. Figure 5.9 shows a cross section of a double sided PMECCs equipped with a squirrel cage rotor. It consists of two rotors, one has permanent magnets fitted on inner and outer back iron, and a rotor which consists of a squirrel cage made of conductive material and pole-pieces located between the bars. Fig 5.10 shows 2D and 3D view of the PMECCs.

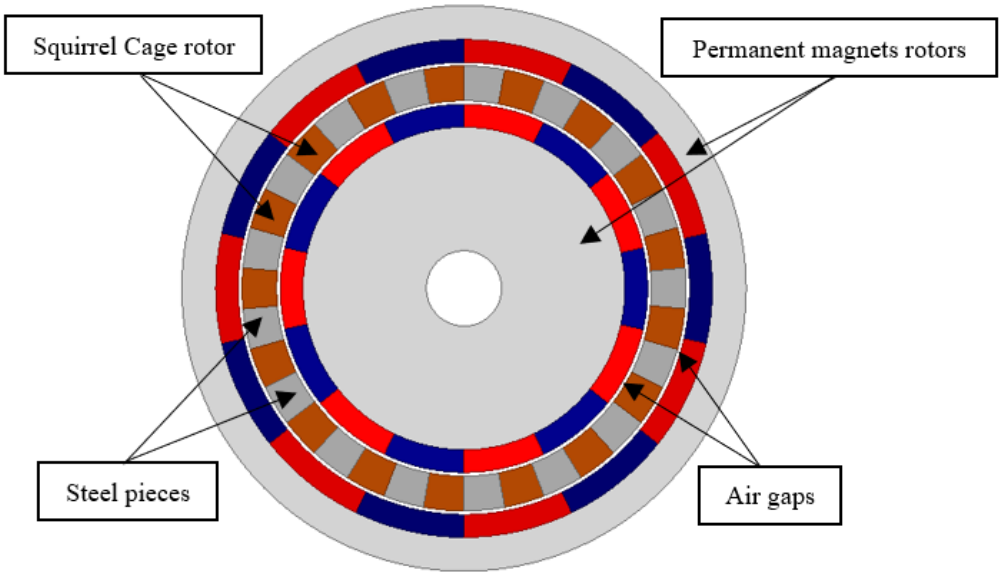

Fig 5. 9 Cross section of double sided PMECCs

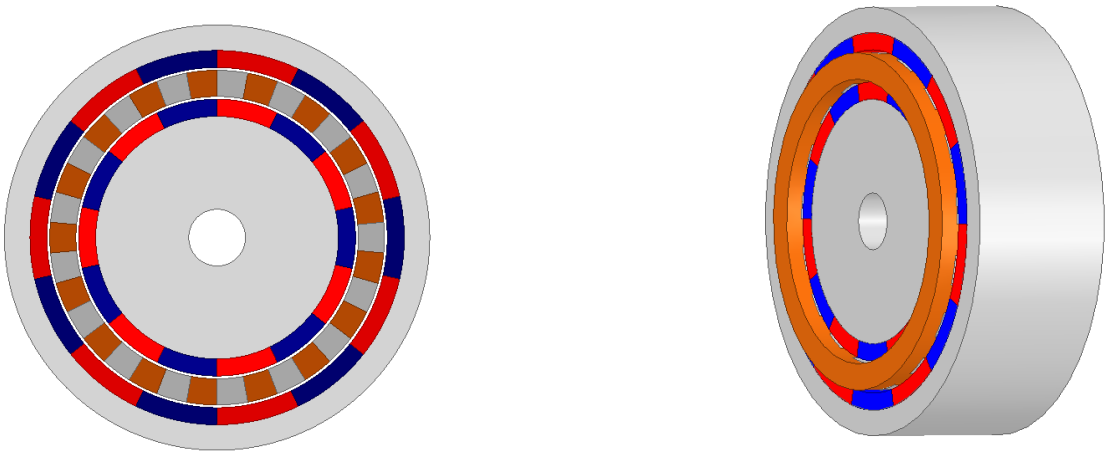

(i) 2D (ii) 3D

Fig 5. 10 Double sided PMECCs equipped with squirrel cage rotor

Similarly, a 2D finite element design is completed and an external circuit is developed and linked to the simulation to study the influence of end ring on the PMECCs performance for different slot depth and conductive material and compared to a 3D predictions. Figure 5.11 show the double sided PMECCs cage rotor, and Table 5.2 shows the parameters of the studied PMECCs.

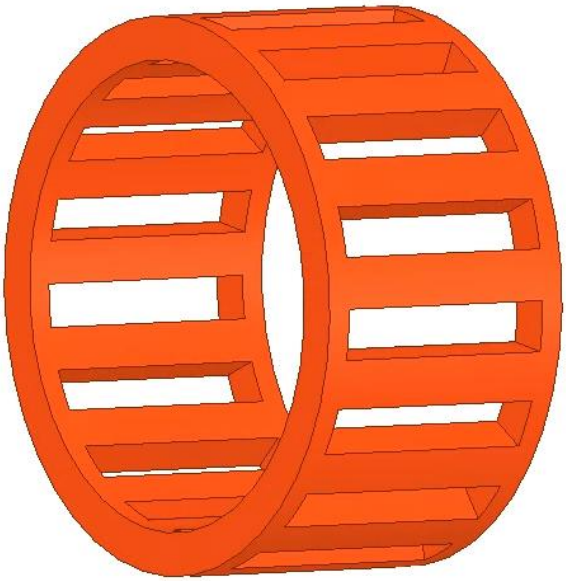

Fig 5. 11 Double sided PMECC cage rotor with 17 bars

Table 5. 2 Double sided PMECC end ring parameters

End ring	Value / type	
Height = slot depth (e_h)	9.2 mm / 13.4 mm	
Cross section area (A)	92.48 mm^2 / 129.51 mm^2	
Mean radius (e_{mr})	54.4 mm / 52.3 mm	
Thickness (e_{th})	5 mm	
Number of bars (Nr)	17	
Conductive material	Cu / Alu	
Material resistivity (ρ)	Cu = 1.7×10^{-8}	Alu= 2.65×10^{-8}

Figure 5.12 shows the variation of transmitted torque with relative speed using 2D and 3D finite element with copper squirrel cage and with different slot depth. While, Figure 5.13 shows the variation of transmitted torque with relative speed of the same PMECCs but with an aluminium squirrel cage rotor. Similarly, for 2D results can be seen that more torque is predicted. Furthermore, in contrast to the single sided PMECCs, adding the end ring inductance results in predicted results closer to 3D finite element. Also, it can be seen in this double sided PMECC and as a result of having two airgaps, The result of 2D simulation and between end ring containing resistance only and when inductance is added to the total impedance of the endring may explain the difference between 2D single and double sided topologies results. On the other hand, it can be viewed that 3D predictions are still less than 2D predictions due to 3D simulation effects.

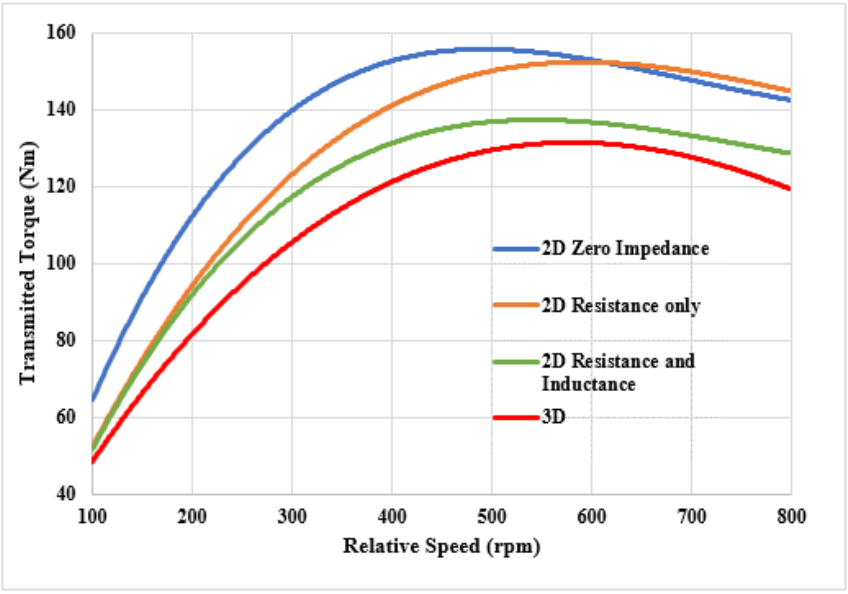

(a) 9.2 mm slot depth

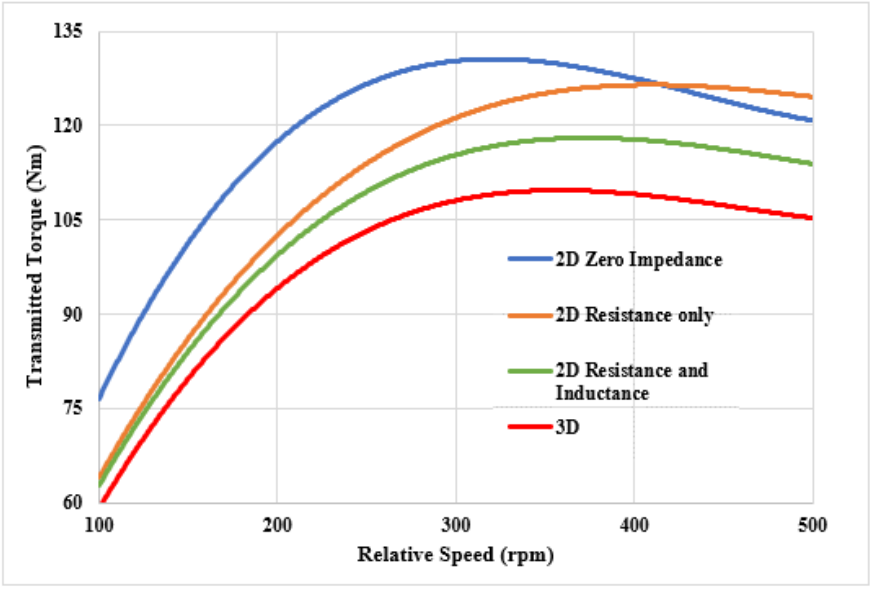

(b) 13.4 mm slot depth

Fig 5. 12 Variation of transmitted torque with relative speed. (copper squirrel cage).

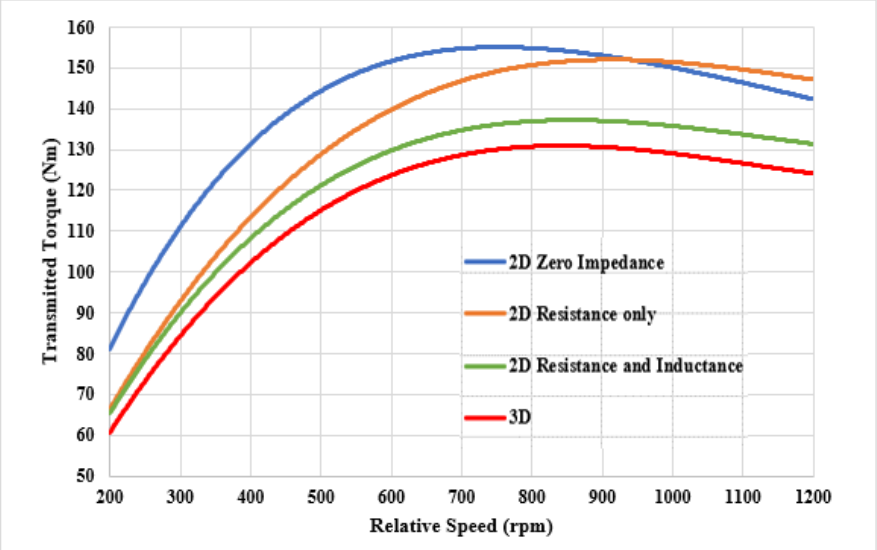

(a) 9.2 mm slot depth

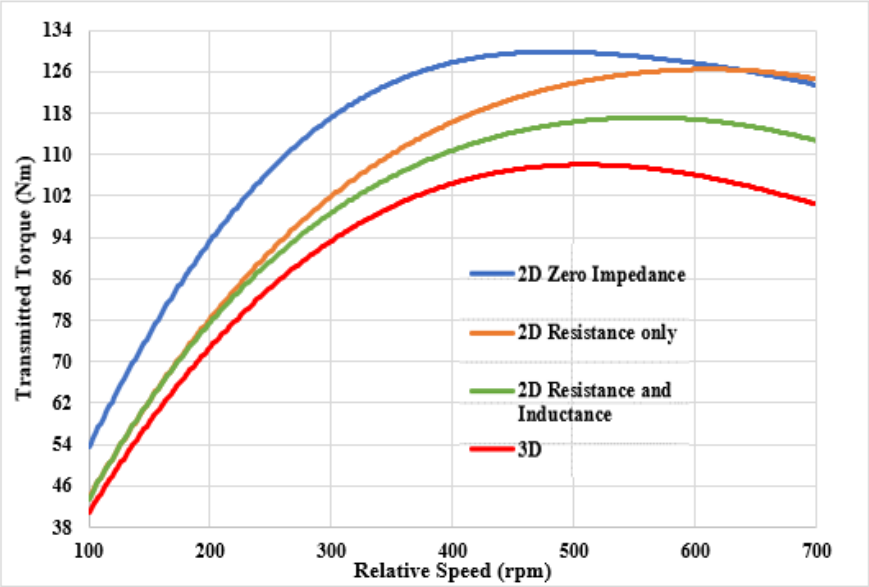

(b) 13.4 mm slot depth

Fig 5. 13 Variation of transmitted torque with relative speed. (Aluminium squirrel cage).

5.4 Summary

In this chapter a comparison between radial 2D and 3D finite element predictions of the torque slip-speed curves of single- and double-sided squirrel cage is undertaken.

As squirrel cage rotor is a major component of the PMECCs and end-ring impedance of the cage rotor contributes to the total impedance of the cage, its representation is considered. Therefore, in 2D simulations an external circuit should be added, and an estimation of the end ring impedance is required. In order to have a better insight of the squirrel cage end ring impedance influence on the PMECCs torque and speed characteristics, two assumptions are considered. First one is that a simple resistance represents the end ring impedance, and the second assumption is to have resistance and inductance to represent the total impedance of the end-ring. It is shown that in circuit-coupled 2D simulations, and the predicted torque slip-speed characteristic is closer to 3D predictions, when compared with the characteristic neglecting the end-ring impedance. It has also been noticed that for single-sided PMECCs, the effect of the end-ring inductance is less significant than the resistance.

Chapter 6

Experimental validation

6.1 Introduction

In this chapter the manufacturing and assembly process of the different components of a single-sided squirrel cage PMECC are presented. Furthermore, tests on the prototype are undertaken and results are compared with predictions and discussed with respect to temperature effects.

6.2 Prototype Squirrel Cage PMECC

The 3D exploded view of the Squirrel Cage PMECC prototype is shown in Fig. 6.1. For the purpose of testing and validation as well as the determination of the variation of the transmitted torque with slip speed, only one rotor is required to rotate, while the other rotor can be made to be part of the stator, i.e. fixed to the stator. This would greatly simplify the manufacture of the prototype, nevertheless, a decision was made to design and manufacture a 2-rotor coupling in order to have a feel of the manufacturing steps/difficulties required to achieve it.

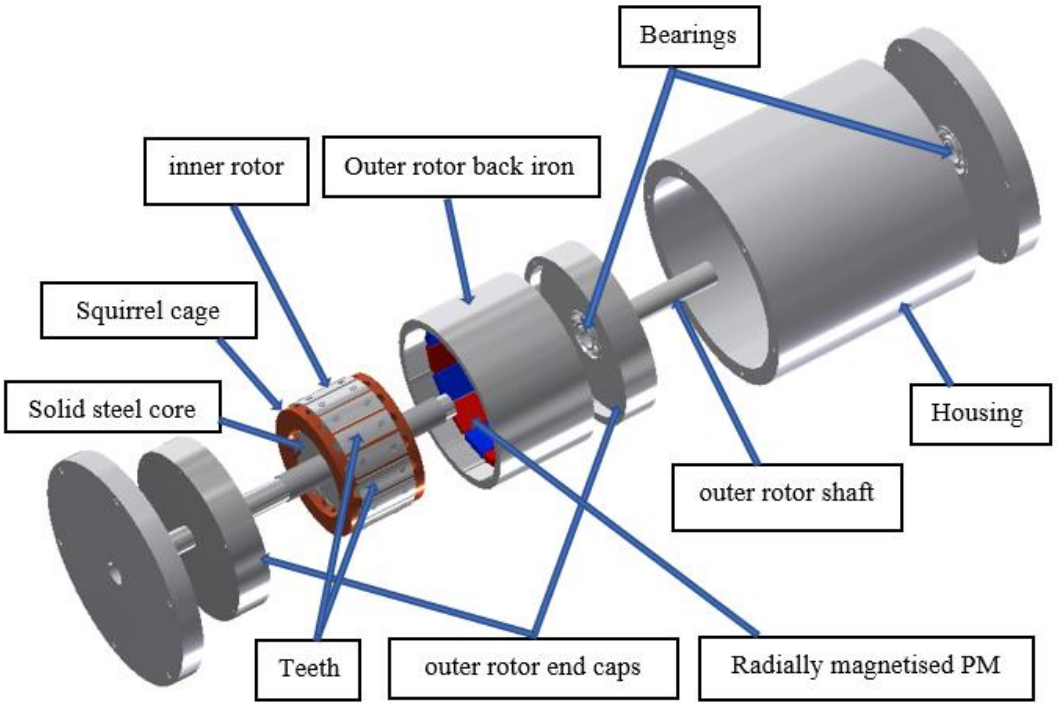

Fig 6. 1 3d exploded view of the SC PMEEC prototype.

6.2.1 Inner Squirrel Cage rotor

The inner rotor of the PMECC is shown in Fig 6.2. It consists of:

- A copper cage with 17 bars.
- A solid steel core with 17 teeth.
- shaft

In order to avoid the contact issues associated with brazing copper rings to the copper bars, the Squirrel cage is manufactured from a solid piece of copper, and slots, where the steel teeth would be inserted are CNC machined. This enables perfect electrical contact between the bars and the rings, see Figs 6.3 and 6.4. Furthermore, since eddy currents induced in a solid steel core, will actually improve the torque transmission capability of the coupling, and for the simplicity of manufacturing the teeth and the back-iron of the Squirrel Cage rotor are manufactured from solid mild steel.

Furthermore, replacing the laminated core to solid could result in slight improved in the torque slip-speed characteristic. However, this affect would be practically negligible due significantly larger electrical resistivity of the steel and compared to that of copper or aluminium conductor. Additionally, Each tooth is fixed to the back-iron using two bolts, as can be seen in Fig. 6.3 and 6.4.

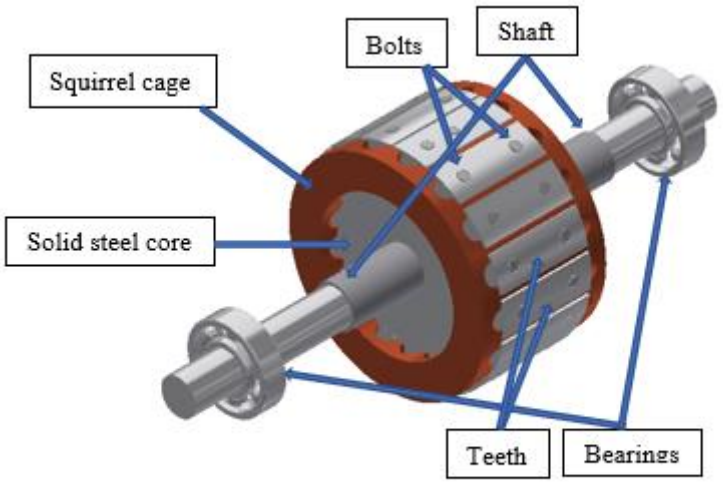

Fig 6. 2 Inner rotor of the PMECC prototype.

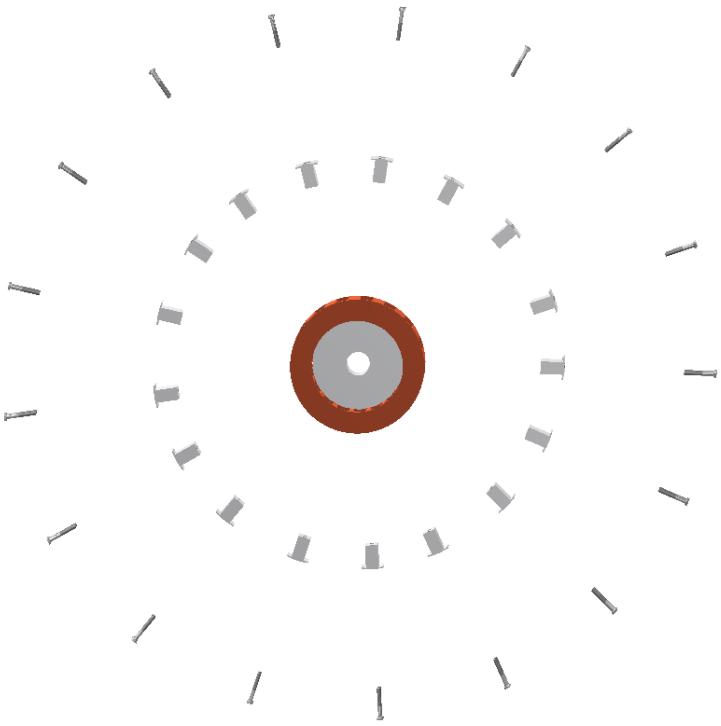

Fig 6. 3 Expanded view for inner rotor of the PMECC prototype.

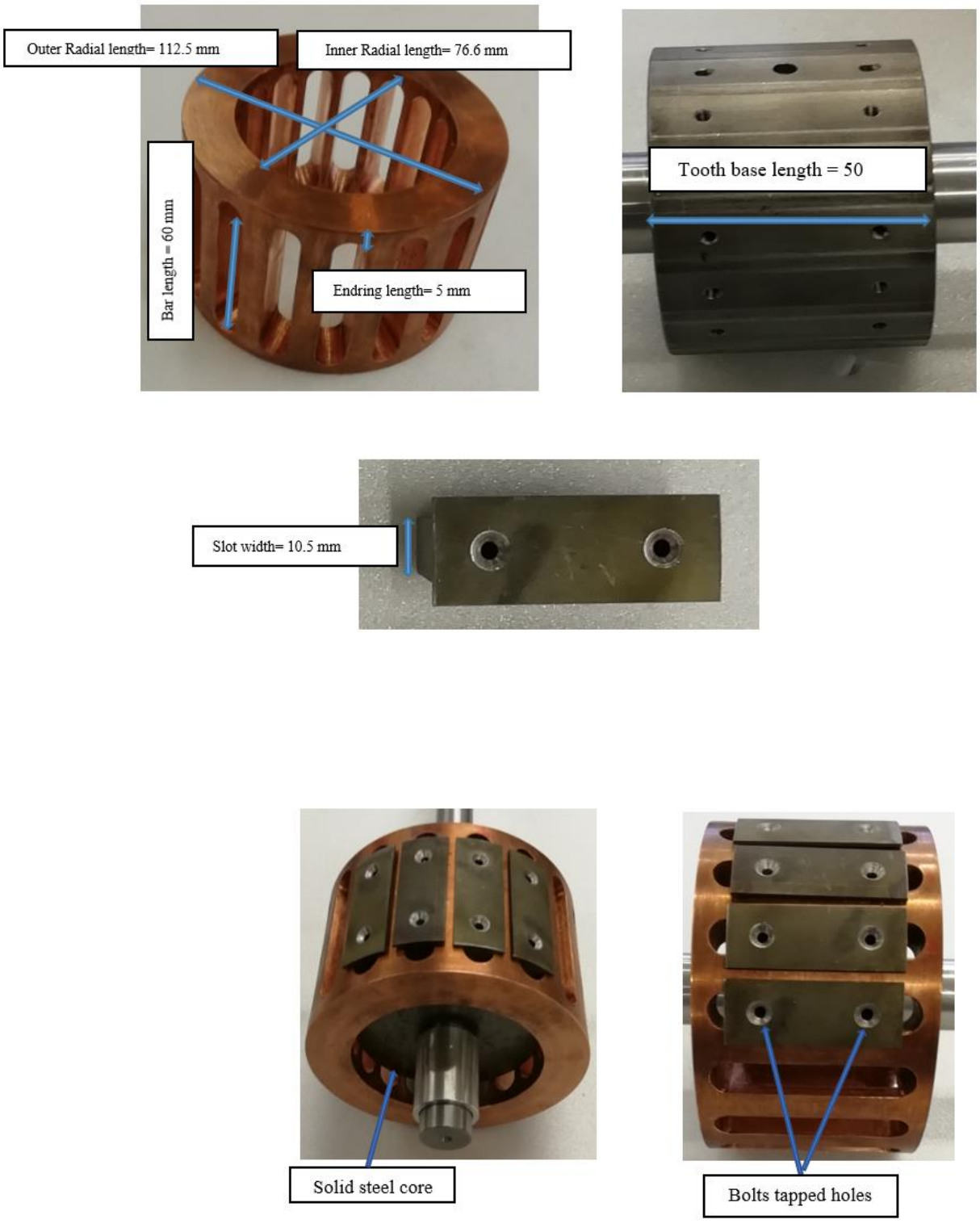

Fig 6. 4 Inner Squirrel Cage rotor of the PMECC prototype during assembly.

6.2.2 Outer PM rotor

The outer rotor part of the PMECC is shown in Fig. 6.5 and it consists of:

- a solid steel back-iron
- 14 permanent magnets poles, assembled using rectangular permanent magnet pieces.
- end caps
- shaft

For simplicity of manufacturing, rectangular-shaped permanent magnets grade (NdFeB 38) are selected and placed on the solid steel back-iron forming the outer rotor of the coupling. Fig. 6.5 shows the outer rotor with magnets and Fig. 6.6 shows expanded view of the Squirrel cage PMECC.


Back iron length=90mm

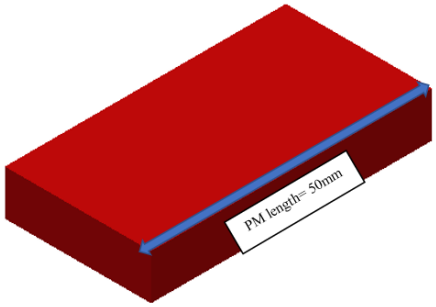
PM length= 50mm

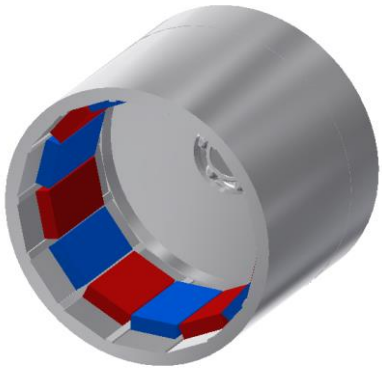

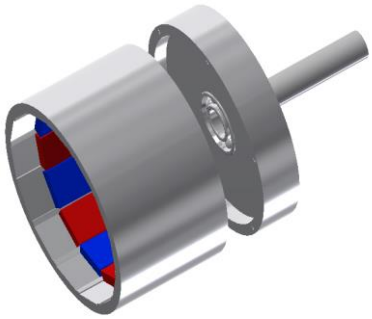

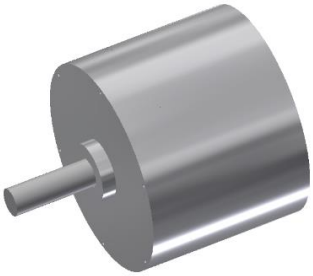

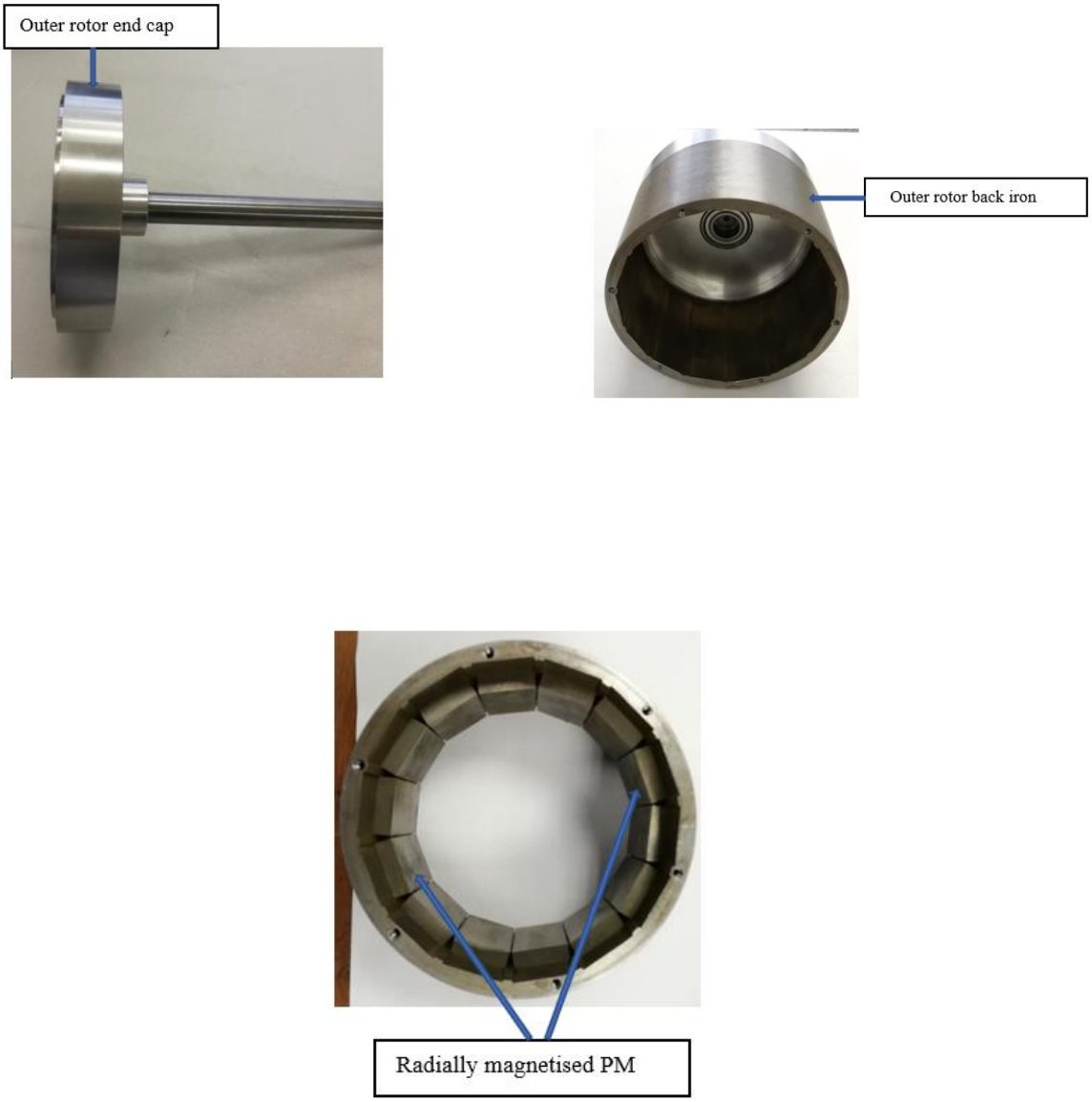

Fig 6. 5 Outer rotor with magnets of the PMECC prototype

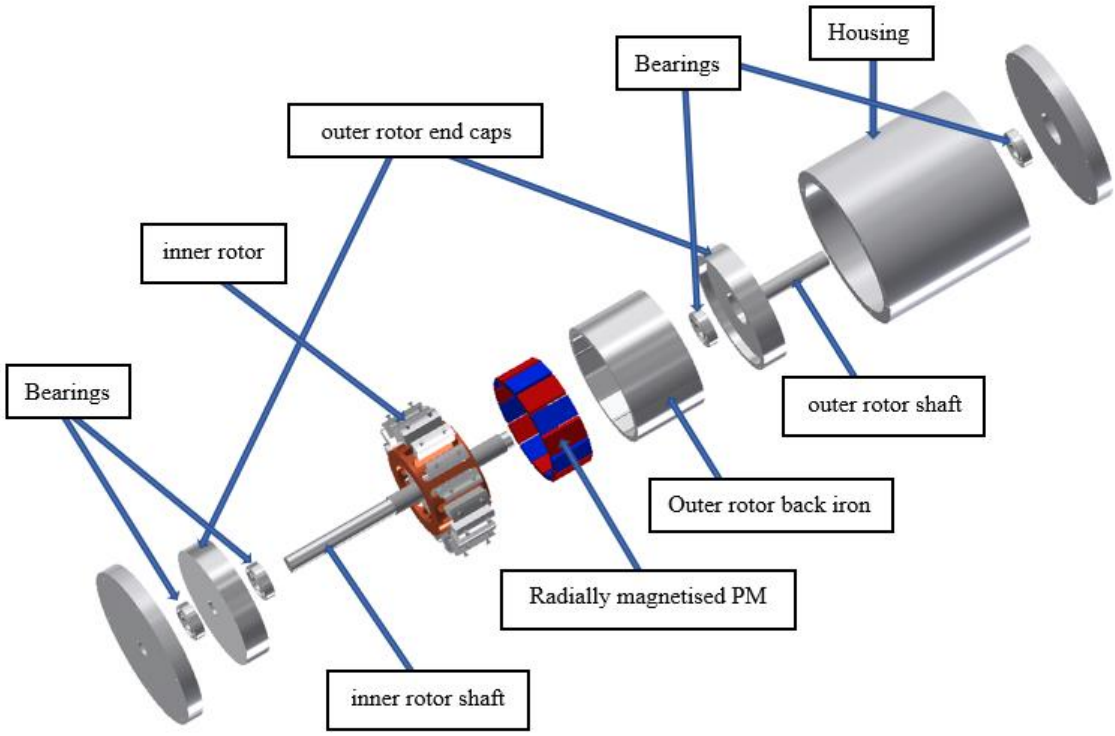

Fig 6. 6 Expanded view of the SC PMECC.

6.2.3 Experimental results and validations

The torque slip-speed characteristic of the coupling is measured using the set-up shown in Fig. 6.7. It includes, dynamometer used as variable speed drive and a torque transducer. During the testing, the outer rotor is locked, using a special bracket to stop it from rotating with respect to the case. Thus, the input speed to the coupling is now also the slip speed between the rotors. Fig. 6.7 shows the test rig of the PMECC, whilst Figs. 6.8 and 6.9 show how the outer rotor is fixed to the rotor and the dynamometer control panel, respectively.

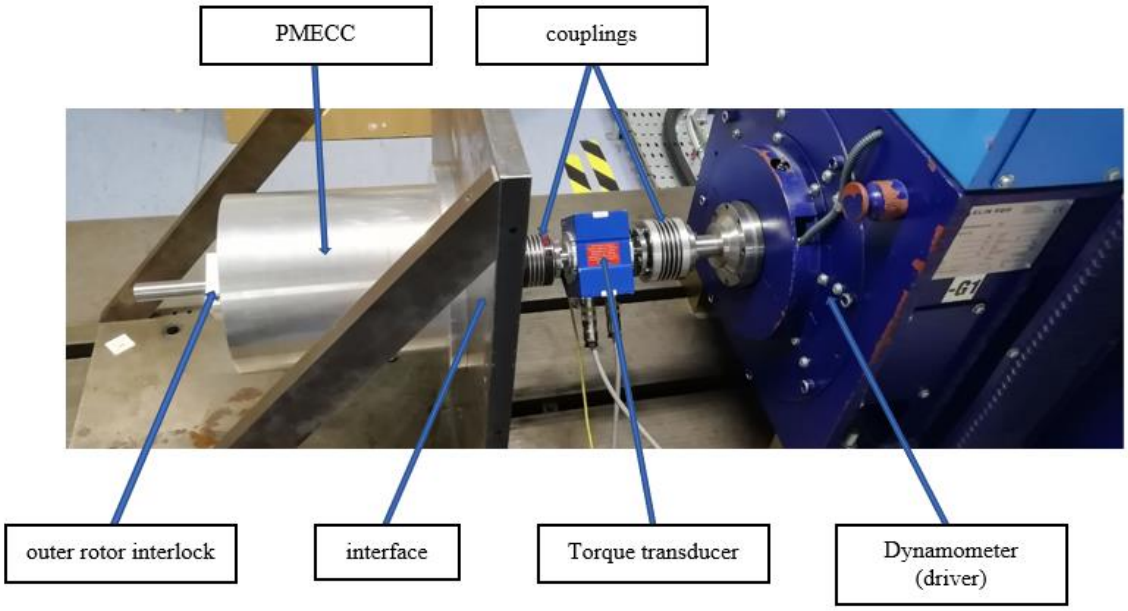

Fig 6. 7 Test rig of the PMECC.

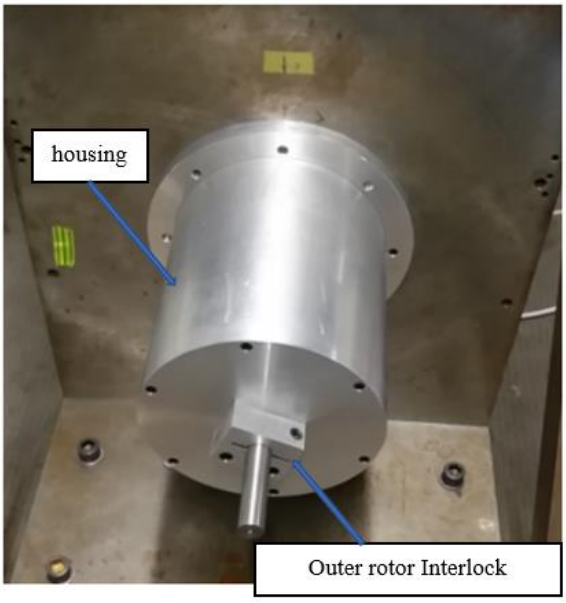

Fig 6. 8 Interlock of the outer rotor.

Fig 6. 9 Dynamometer control panel.

Since the resistivity of the Squirrel Cage material has a significant effect on the torque slip-speed characteristic of the PMECC, and due to a large amount of eddy currents induced in the cage and caused by interaction between the two rotors, the temperature of the PMECC rises and leads to an increase in resistivity of the conductive materials of the cage. Therefore, in order to produce test results which can be reliably compared to predictions, the test points have to be taken at a specific temperature. Therefore, each test point is undertaken from cold, and about 2-hour cool down period is left between consecutive test points, in order to ensure that temperature in the device is close to the ambient laboratory temperature. Fig. 6.10 compares the measured and predicted transmitted torques with relative speed of the coupling at room temperature. It can be seen, that good agreement exists between

measured and predicted results. It can also be seen, that for this particular coupling the speed at which the maximum torque occurs is $\alpha \approx 100$ rpm, which is conductive to higher efficiency and more precise torque transmission. On the other hand, if temperature rise of the cage is neglected, and is allowed to rise, Fig 6.11 compares the measured torques, without consideration to temperature and 3D predicted torque at room temperature. It can be clearly seen, temperature has a significant effect on relative speed, and that if temperature is not appropriately monitored, comparison with predictions would not be useful.

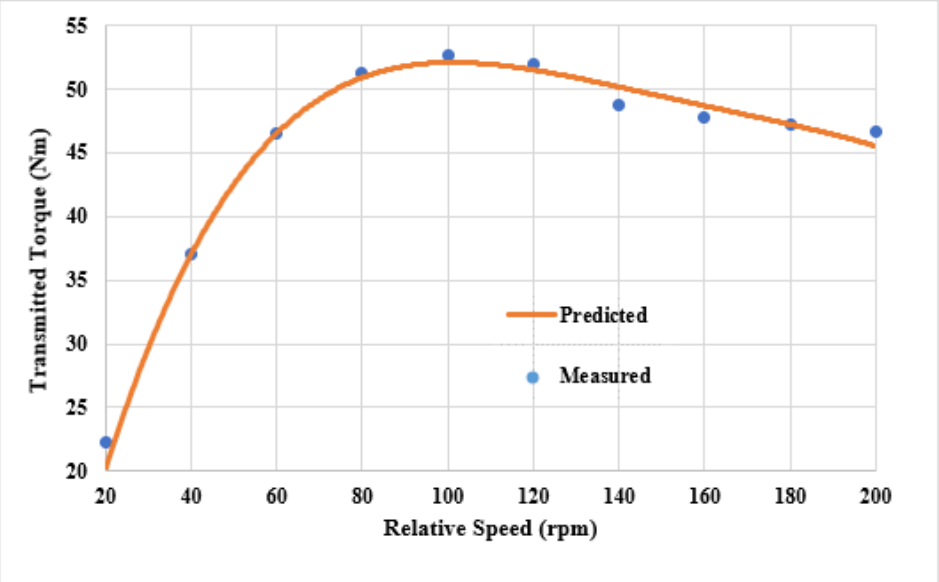

Fig 6. 10 Measured and predicted torque vs relative speed at room temperature

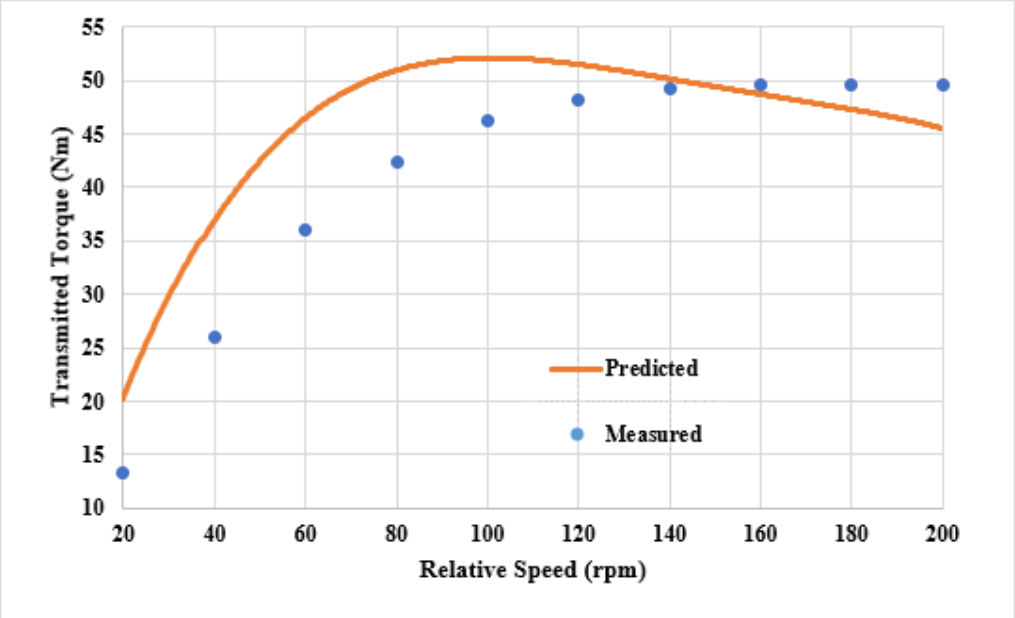

Fig 6. 11 Measured and predicted torque vs relative speed at high temperature.

Additionally, PM are placed on the outer rotor of the coupling to be away from the heat generated from copper due to eddy currents flow. Therefore, the permanent magnets properties will not be affected by heat. Furthermore, In order to better understand the effects of temperature due to eddy currents in squirrel cage on the coupling performance, Fig 6.12 shows the variation of the predicted transmitted torques with relative speed of the coupling at different temperatures. It can be seen that temperature of the cage has a negligible effect on the maximum transmitted torque, while having a significant effect on the speed at which the maximum torque occurs, as can also be seen in Figs 6.13 and 6.14 which show the variation of the maximum transmitted torque and the corresponding relative speed, α, with temperature.

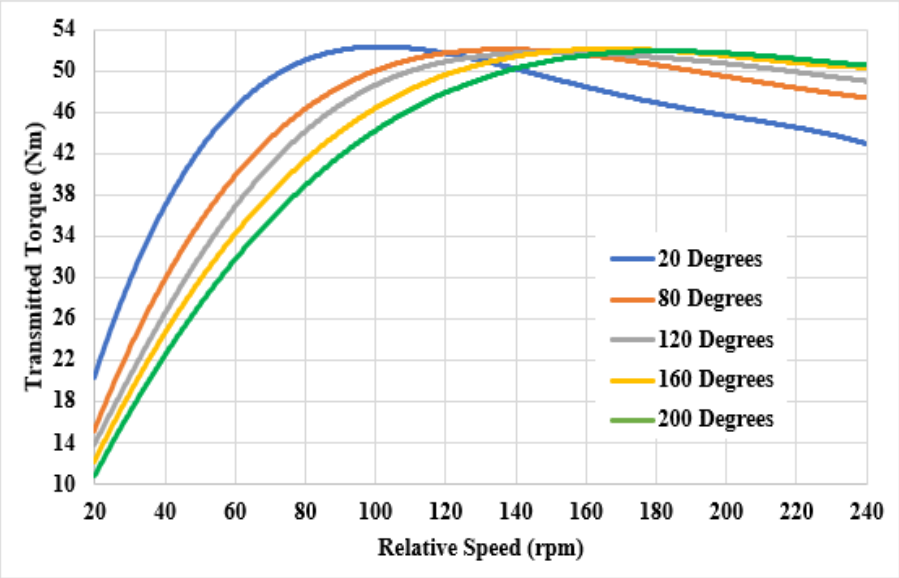

Fig 6. 12 Variation of transmitted torque with relative speeds with copper material.

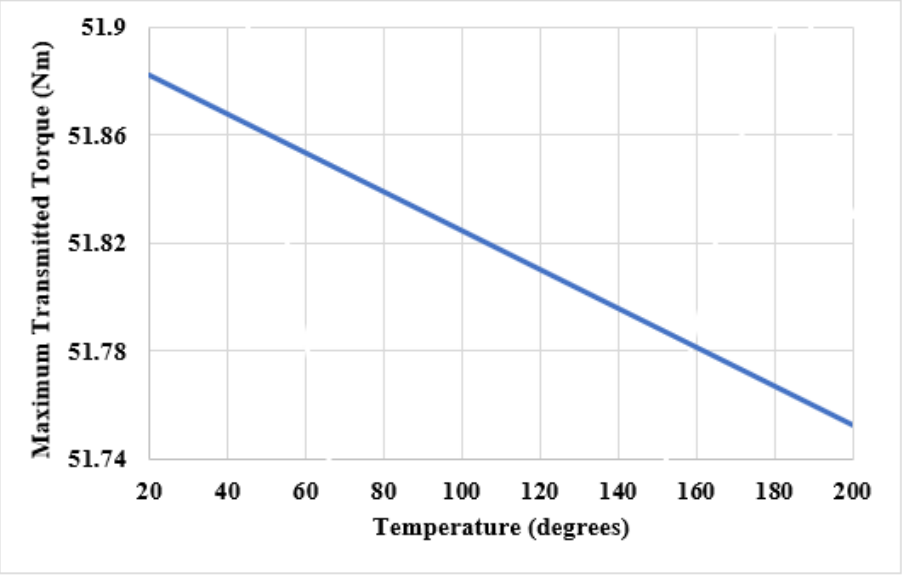

Fig 6. 13 Variation of maximum transmitted torque with temperature with copper cage.

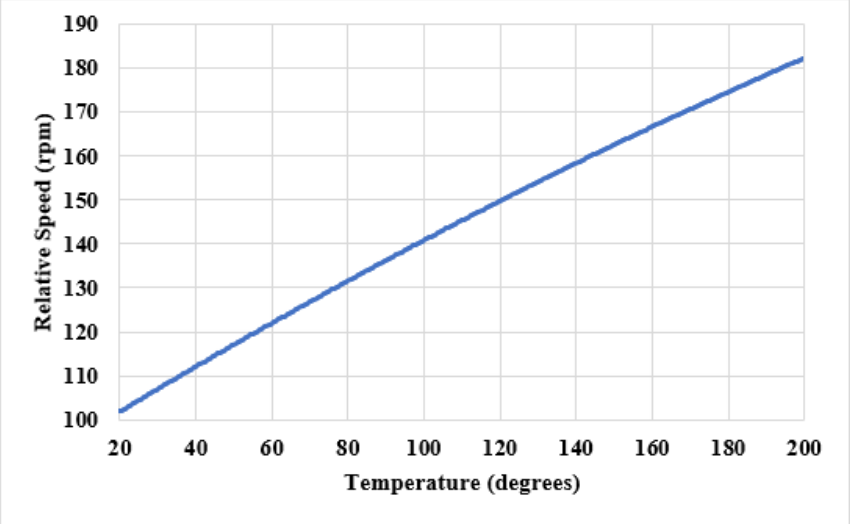

Fig 6. 14 Variation of relative speed with temperature with copper cage.

Similarly, for an Aluminium cage, Fig 6.15 shows the variation of the predicted transmitted torques with relative speed of the coupling at different temperatures. It can be seen that temperature of the cage has a negligible effect on the maximum transmitted torque, while having a significant effect on the speed at which the maximum torque occurs, as can also be seen in Figs 6.16 and 6.17 which show the variation of the maximum transmitted torque and corresponding speed α with temperature.

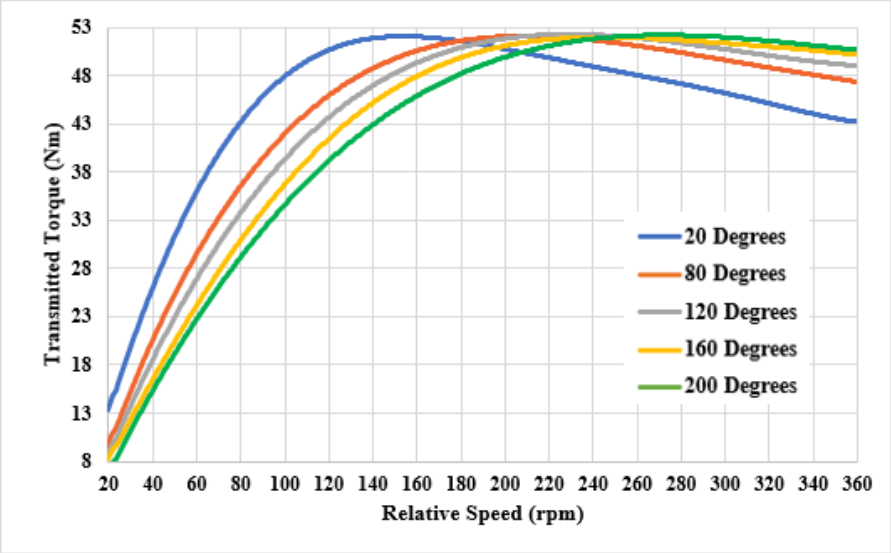

Fig 6. 15 Variation of transmitted torque with relative speeds for Aluminium cage.

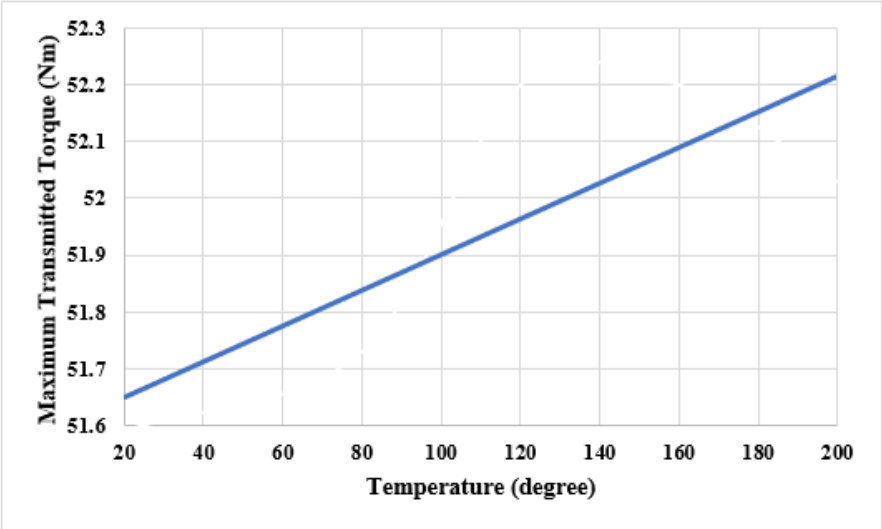

Fig 6. 16 Variation of maximum transmitted torque with temperature for aluminium cage.

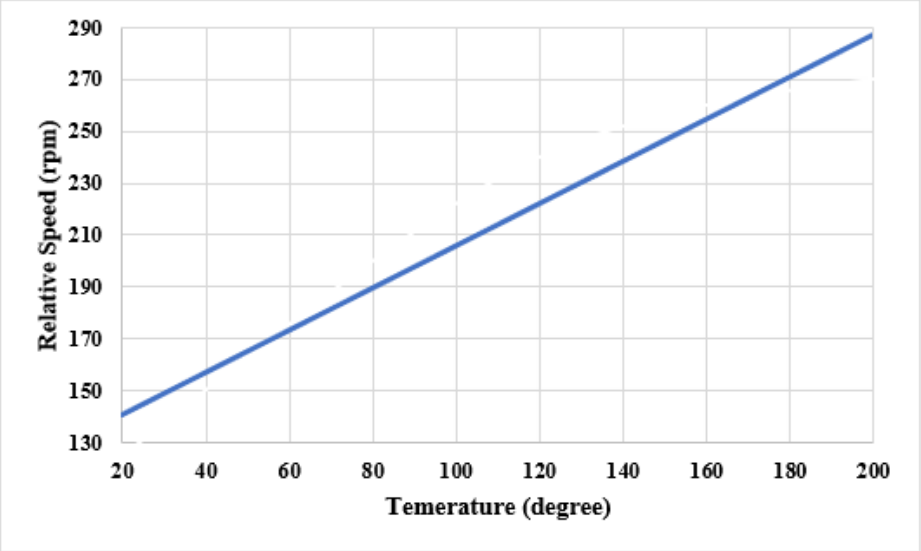

Fig 6. 17 Variation of relative speed with temperature for aluminium cage.

In addition, in order to understand the extent of the temperature rise in the copper cage, a test is undertaken, whereby the coupling is run at a constant speed of 40 rpm and the transmitted torque is monitored and recorded every 3 minutes, up to maximum time of 160 min. Fig 6.18 shows the variation of transmitted torque with time, whilst Fig. 6.19 shows the variation of the estimated temperature of the cage. The temperature of the cage is estimated by varying the resistivity of the squirrel cage in the finite element model, until the predicted torque matches the measured torque. It can be seen, that at 40rpm, which is located at the resistance limited section of the torque slip-speed curve, temperature rise has a significant effect on the transmitted torque.

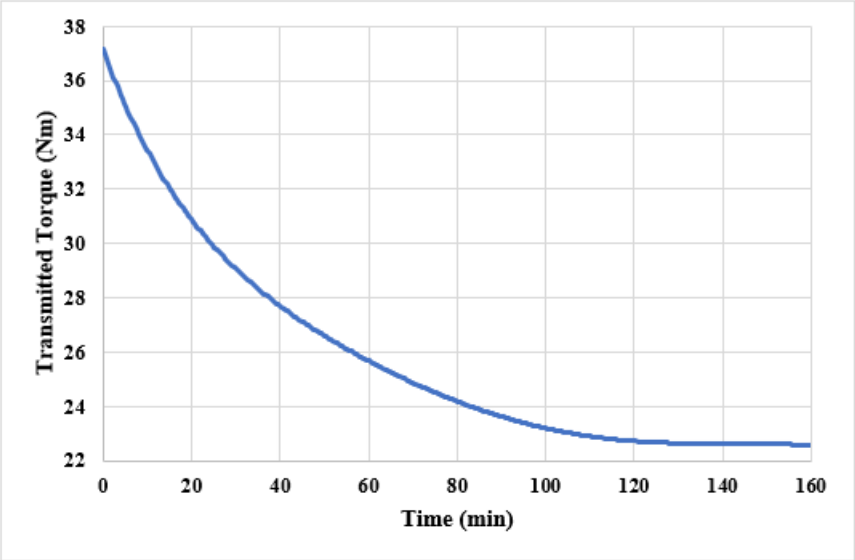

Fig 6. 18 Variation of transmitted torque against time at 40 rpm.

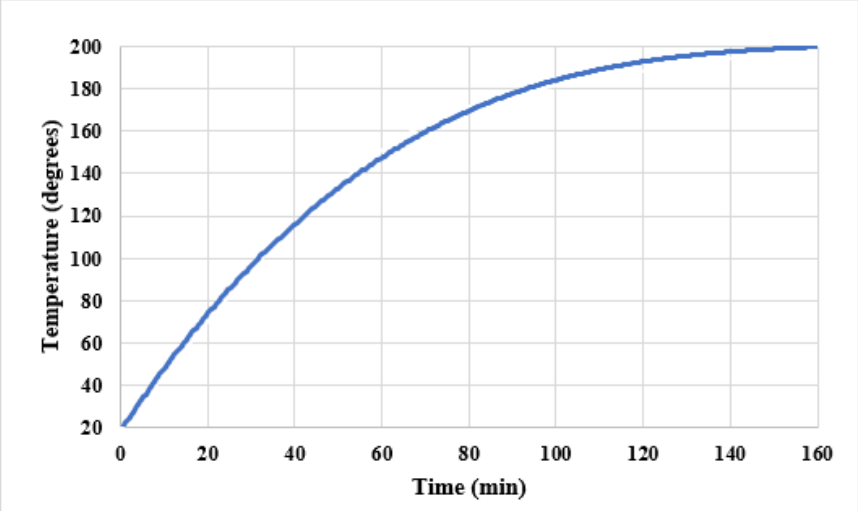

Fig 6. 19 Variation of the estimated temperature of the cage.

6.3 Summary

In this chapter, the manufacturing steps for the squirrel cage PMECC are described, and a prototype is tested. In order, to eliminate contact issues between the bars and the rings, the squirrel cage has been machined from a solid block of copper, whilst the teeth are made from solid mild steel and fixed to the back-iron using high strength bolts. It has been shown that good agreement exists between measured and 3D-FEA predicted transmitted torque at room temperature. It has also been shown that temperature rise has a negligible effect on the maximum transmitted torque, while having a significant effect on the slip speed it occurs. Furthermore, when operated continuously, such as during the 40rpm slip-speed test, squirrel cage temperatures in excess of 200^{o}C can be reached, however, this is well within the operating temperatures of the materials of the squirrel cage rotor.

Chapter 7

Conclusion and future work

In this thesis an investigation into the design and analysis of PMECC devices for the use of electric vehicle as a limited slip-differentials as well as power transmission are introduced. The examined models includes radial and axial single- and double-sided topologies. Various parameters of the PMECCs are analysed, these include conductive rotor structures, mainly a squirrel cage and sheet rotor type, permanent magnets thickness, conductive rotor material, squirrel cage PMECCs pole/ slot combinations, and finally the thickness of the conductive sheet rotor. Due to the geometry of the various topologies, 3D has been the main technique employed for the determination of torque and slip-speed characteristics of the different design of the PMECCs. However, a comparison between 2D and 3D designs predictions is also undertaken for radial-field single- and double-sided squirrel cage PMECCs, where it has been shown that circuit coupled 2D finite element analysis can be employed to approximate the value of the end ring impedance. Furthermore, it has been shown that improvement in efficiency can be realized by reducing the resistance of the conductor without significantly reducing the PM air gap field. This can be realized by employing the squirrel cage which enable reduction in the conductor resistance through an increase in slot depth without significantly reducing the PM air gap field. Especially, when the conductor rotor is internal in radial field topologies where an increase in slot depth does not lead to an increase in PMECC size. In contrast, for PMECC using conductor sheet a reduction in a conductor resistance

through increasing the sheet thickness always leads to decrease in the PM air gap flux due to an increase in the effective air gap.

For LSD applications in electrical vehicles, it has been shown that for the particular vehicle investigated, PMECC energy efficiency in excess of 99% can be achieved over the NEDC driving cycle, if the slip-speed corresponding to the maximum transmitted torque is kept below 100rpm. Furthermore, different drivetrain topologies have been proposed, where the LSD using PMECC could be a good candidate. and a variety of potential drivetrains configuration for the Hybrid /Electric vehicle and electrical machine where PMECCs can be employed as a limited slip-differential are proposed.

Moreover, a single- sided radial PMECCs fitted with 14 poles and a copper squirrel cage rotor containing 17 slots is selected and manufactured. The steps of the assembly are explained, and the prototype is tested. . Results have shown that at room temperature there is a good agreement between measured and 3D-FEA predicted transmitted torque. However, it was also highlighted that care should be taken in terms avoiding the effects of the cage temperature rise, which affects the torque slip-speed characteristic. It has been confirmed that temperature rise has a negligible effect on the maximum transmitted torque, whilst having a major impact on the corresponding slip speed.

For future investigation, some recommendations could be proposed as follows:

1- Investigation of the performance of the radial field electrically excited eddy current couplings topology (EMECCs), in terms of mass and/or cost of active materials and efficiency over a driving cycle, and temperature effect on the magnets and conductive materials.

2- Investigation of the performance of transverse flux eddy current coupling topologies, both PM and coil excited.

3- Experimental investigation of the PMECCs with different load conditions.

4- Investigation of different squirrel cage rotor slots shapes on PMECCs performance.

References

[1] Qingzhong G, Wang D and Sheng L 2014 Application of field theory to air gap permanent magnet eddy current coupling **73** 44–51

[2] Wallace A and Jouanne A Von 2001 Wallace, A., C. Wohlgemuth, and K. Lamb. 'A high efficiency, alignment and vibration tolerant, coupler using high energy-product permanent magnets.' (1995): 232-236. 57–63

[3] MAGNETIC DRIVE COUPLINGS A.C.Smith, S.Williamson, A.Benhama, L Counter and J.M.Papadopoulos Brook Hansen, UK and Rexnord Technical Services, USA

[4] Wallace, Alan, and A. Von Jouanne. 'Industrial speed control: Are PM couplings an alternative to VFDs?.' IEEE Industry Applications Magazine 7.5 (2001): 57-63.

[5] Canova A, Freschi F, Gruosso G and Vusini B 2005 Genetic optimisation of radial eddy current couplings *COMPEL - Int. J. Comput. Math. Electr. Electron. Eng.* **24** 767–83

[6] Erasmus A S and Kamper M J 2015 Analysis for design optimisation of double PM-rotor radial flux eddy current couplers *2015 IEEE Energy Convers. Congr. Expo. ECCE 2015* 6503–10

[7] Atallah K and Wang J 2011 A brushless permanent magnet machine with integrated differential *IEEE Trans. Magn.* **47** 4246–9

[8] Lequesne B 1997 Eddy-current machines with permanent magnets and solid rotors *IEEE Trans. Ind. Appl.* **33** 1289–94

[9] Canova A and Vusini B 2003 Design of axial eddy-current couplers *IEEE Trans. Ind.*

Appl. **39** 725–33

[10] Rahideh A and Korakianitis T 2011 Analytical magnetic field distribution of slotless brushless machines with inset permanent magnets *IEEE Trans. Magn.* **47** 1763–74

[11] 2014 Mohammadi, S., Mirsalim, M., Niazazari, M. and Talebi, H.A., 2014, February. A new interior permanent-magnet radial-flux eddy-current coupler. In Power Electronics, Drive Systems and Technologies Conference (PEDSTC), 2014 5th (pp. 500-505). IEEE. 172–6

[12] Boroujeni S T and Naghneh H B 2017 Analytical modelling and prototyping a slotless surface-inset PM machine *IET Electr. Power Appl.* **11** 312–22

[13] Razavi H K and Lampérth M U 2006 Eddy-current coupling with slotted conductor disk *IEEE Trans. Magn.* **42** 405–10

[14] Mohammadi S, Mirsalim M, Vaez-Zadeh S and Talebi H A 2014 Design analysis of a new axial-flux interior permanent-magnet coupler *PEDSTC 2014 - 5th Annu. Int. Power Electron. Drive Syst. Technol. Conf.* 562–7

[15] Dai X, Liang Q, Cao J, Long Y, Mo J and Wang S 2016 Analytical Modeling of Axial-Flux Permanent Magnet Eddy Current Couplings with a Slotted Conductor Topology *IEEE Trans. Magn.* **52** 1–15

[16] Li Z, Yan L, Qu B and Fu K 2020 Analytical prediction and optimization of torque characteristic for flux-concentration cage-type eddy-current couplings with slotted conductor rotor topology *Int. J. Appl. Electromagn. Mech.* **62** 295–313

[17] Canova A and Vusini B 2005 Analytical modeling of rotating eddy-current couplers *IEEE Trans. Magn.* **41** 24–35

[18] Li Y, Lin H, Tao Q, Lu X, Yang H, Fang S and Wang H 2019 Analytical Analysis of

an Adjustable-Speed Permanent Magnet Eddy-Current Coupling with a Non-Rotary Mechanical Flux Adjuster *IEEE Trans. Magn.* **55**

[19] Li Y, Lin H, Yang H, Fang S, Wang H and Wang K 2017 Analysis of a novel axial flux permanent magnet eddy-current coupling with a movable stator ring *2017 20th Int. Conf. Electr. Mach. Syst. ICEMS 2017*

[20] Idaho National Laboratory History of Electric Cars available at https://avt.inl.gov/sites/default/files/pdf/fsev/HistoryOfElectricCars.pdf

[21] Guarnieri, Massimo. 'Looking back to electric cars.' 2012 Third IEEE History of Electro-technology Conference (HISTELCON). IEEE 2012. Looking Back to Electric Cars

[22] Sulzberger C "An early road warrior: electric vehicles in the early years of the automobile. . I P and E M 2. . (2004): 66-71. 2004 An early road warrior *IEEE Power Energy Mag.* **2** 66–71

[23] Kebriaei M, Niasar A H and Asaei B 2016 Hybrid electric vehicles: An overview *2015 Int. Conf. Connect. Veh. Expo, ICCVE 2015 - Proc.* 299–305

[24] Ni L 2013 E Nergy S Torage T Echnologies : *"Energy storage Manag. a small Ser. plug-in hybrid Electr. Veh. Thesis Dr. Philos. Univ. Nebraska, 2010* 2–3

[25] Berry I, Khusid M, Manolis K and Arthur M 2009 MIT Electric Vehicle Team What's the Deal with Hybrid and Electric Cars ? http://web.mit.edu/evt/EVT2009_IAPClass_Day1.pdf

[26] Sen P K, Kumar Bohidar S, Kumar L, Kumar Dewangan B and Singh C 2014 Study on Classification of Differential System in Automobile *Int. J. Res. Appl. Sci. Eng. Technol.* **2** 191–4

[27] Gair S, Cruden A, McDonald J and Hredzak B 2004 Electronic differential with sliding mode controller for a direct wheel drive electric vehicle *Proc. IEEE Int. Conf. Mechatronics 2004, ICM'04* 98–103

[28] Zhao Y E, Zhang J W and Guan X Q 2009 Modeling and simulation of electronic differential system for an electric vehicle with two-motor-wheel drive *IEEE Intell. Veh. Symp. Proc.* 1209–14

[29] Crelerot, O., Bernot, F. and Kauffmann, J.M., 1993, September. Study of an electrical differential motor for electrical car. In Electrical Machines and Drives, 1993. Sixth International Conference on (pp. 416-420). IET.

[30] Sinha S, Deb N K, Mondal N and Biswas S K 2008 The differential induction machine: Theory and performance *Sadhana - Acad. Proc. Eng. Sci.* **33** 663–70

[31] Outbackcrossing.com.au. (2017). The Spin on 4WD Differentials. [online] Available www.outbackcrossing.com.au/FourWheelDrive/The_Spin_on_4WD_Differentials.shtml [Accessed 24 July. 2020].

[32] Chevy Hardcore, (2018). Choosing A Limited Slip Differential. [online] Available at: https://www.chevyhardcore.com/news/throwback-thursday-limited-slip/ [Accessed 24 July. 2020].

[33] Open vs. Limited Slip Differentials. [online] Speedwaymotors.com. Available at: http://www.speedwaymotors.com/the-toolbox/open-vs-limited-slip-differentials/28854 [Accessed 24 July. 2020].

[34] All wheel Driven, How does Viscous Coupling work? Available at https://www.awdwiki.com/en/viscous+coupling [Accessed 28 Nov. 2020].

[35] How a CAR works, Viscous coupling available at

https://www.howacarworks.com/illustrations/viscous-coupling [Accessed 26 Nov. 2020]

[36] Nasri A and Gasbaoui B 2012 Artificial Intelligence Application's for 4WD Electric Vehicle Control System *Intell. Control Autom.* **03** 243–50

[37] BARLOW, T.J., Latham, S., McCrae, I.S. and Boulter, P.G., 2009. A reference book of driving cycles for use in the measurement of road vehicle emissions. TRL Published Project Report. P.2,6,25 [eBook] available at: https://assets.publishing.service.gov.uk/government/uploads/system/uploads/attachment_data/file/4247/ppr-354.pdf

[38] Nicolas, R. (2013). The different driving cycles. [online] Car Engineer. Available at: http://www.car-engineer.com/the-different-driving-cycles/ [Accessed 2 Aug. 2020].

[39] Test cycles. Available at: globalfueleconomy.org https://www.globalfueleconomy.org/transport/gfei/autotool/approaches/information/test_cycles.asp#European [Accessed 2 Aug. 2020].

[40] MathWorks, Vehicle with Four-Wheel Drive, available at https://uk.mathworks.com/help/physmod/sdl/ug/vehicle-with-four-wheel-drive.html [Accessed 26 Nov. 2020]

[41] Dorrell D G 2005 Calculation and effects of end-ring impedance in cage induction motors *IEEE Trans. Magn.* **41** 1176–83

[42] Williamson S and Mueller M A 1993 Calculation of the impedance of rotor cage end rings *IEE Proc. B Electr. Power Appl.* **140** 51–60

[43] Lombard P and Zidat F 2016 Determining end ring resistance and inductance of squirrel cage for induction motor with 2D and 3D computations *Proc. - 2016 22nd*

Int. Conf. Electr. Mach. ICEM 2016 266–71